A Delft University of Technology Master's thesis

Towards quantifying changes in the modelled spatio-temporal variability in the ocean heat forcing to the Greenland tidewater glaciers

ABHAY PRAKASH

Towards quantifying changes in the modelled spatio-temporal variability in the ocean heat forcing to the Greenland tidewater glaciers

A study based on global climate model simulations of pre-industrial, historical and RCP 8.5 scenarios

ABHAY PRAKASH

Towards quantifying changes in the modelled spatio-temporal variability in the ocean heat forcing to the Greenland tidewater glaciers
A study based on global climate model simulations of pre-industrial, historical and RCP 8.5 scenarios.

Supervisors:
Dr.Miren Vizcaino, Faculty of Civil Engineering and Geosciences,
Department of Geosciences and Remote Sensing: Ice and Climate: TU Delft

Dr.Sarah Bradley, Faculty of Civil Engineering and Geosciences,
Department of Geosciences and Remote Sensing: Ice and Climate: TU Delft

Dr.Caroline A. Katsman, Faculty of Civil Engineering and Geosciences,
Department of Environmental Fluid Mechancis: Physical Oceanography: TU Delft

Prof.Dr.-Ing.habil.Roland Klees, Faculty of Civil Engineering and Geosciences, Department of Geosciences and Remote Sensing: Physical and Satellite Geodesy: TU Delft

Master's Thesis 2017:NN

Cover: Image acquired from www.lifeonthinice.com © JENNY E. ROSS.

Abstract

The Greenland Ice Sheet has a total volume of 2900000 km^3. In recent decades, the ice-sheet has been losing mass rapidly and has nearly doubled its contribution to sea-level rise. One main contributing factor has been the recent widespread acceleration of the tidewater glaciers that terminate in deep and narrow glacial fjords. However, our understanding of the subsurface water properties causing this acceleration has been extremely limited owing to the lack of observations around these locations. We hypothesize that while the ice-sheet is not coupled to the ocean in the current General Circulation Models (GCMs), they can still be used to improve our understanding of the subsurface warming around these regions.

In this study, we first evaluate two GCMs (HADGEM2-ES and GISS-E2-R) around three tidewater glacier locations, by interpolating the high resolution CTD data to the GCM grid. Our results substantiate that GISS-E2-R performs better than the HADGEM2-ES model along the Western Margin. However, along the Eastern Margin, we find that the HADGEM2-ES model is more consistent with the observations. The modelled spatio-temporal variability of water masses was investigated in a Pre-Industrial and Historical simulation, later used to quantify the evolution of subsurface warming under a future warming (RCP 8.5) scenario. Our results show that the Kangerlussuaq glacier (shelf) is more sensitive to greenhouse gas (GHG) forcings than Helheim and Jakobshavn. With respect to the Pre-Industrial climate, the mean warming of the Kangerlussuaq shelf under the RCP 8.5 scenario is 3.76° C, which is considerably greater than Helheim (2.38° C) and Jakobshavn (1.92° C). This is predominantly driven by the subsurface Return Waters of the Arctic Atlantic which are seen to warm the most under a future warming (RCP 8.5) scenario.

For each of the three simulation, we decompose the Ocean Heat Content (OHC) time-series into intrinsic oscillatory modes so as to discern and quantify the high-frequency variability from the multi-year/decadal variability and trends in the OHC. Where the contribution from the high-frequency modes to the total energy contained in the OHC signal is considerable in a Pre-Industrial scenario; the Historical and RCP 8.5 derived OHC are seen to contain a very dominant low-frequency response to GHG forcings, which contains (almost) all of the energy contained in the signal. For the RCP 8.5 scenario, we infer that at Kangerlussuaq, such a response is considerably greater than other locations. Furthermore, a consistent long-term increasing trend is seen in the upper ocean heat content for Kangerlussuaq, throughout the 21st century (1.01×10^8 J/m^2/month), unlike our inferences from other locations. This trend is found to be an order of magnitude higher than Helheim (2.36×10^7 J/m^2/month) and Jakobshavn (1.27×10^7 J/m^2/month). Our results also indicate that sea-ice free months at the Nares Strait (A.D. 2055 onwards) allows for a relatively greater mixing of the Lincoln Sea and Baffin Bay waters, which is consistent with the decline and stagnation of the rising OHC at Jakobshavn.

Keywords: Greenland ice sheet, tidewater glaciers, GCMs, climate projections, spatio-temporal variability, Kangerlussuaq, Helheim, Jakobshavn.

Acknowledgement

In this thesis, we take a new step towards improving our understanding of the subsurface ocean heat forcing around prominent tidewater glacier locations around Greenland. While previously undermined, the recent acceleration of these glaciers has highlighted the importance of ocean-ice interaction. I hope that reading this document provides the reader with new insight and more importantly, new ideas and means to further extend our work. The commencement of this research coincided with the launch of NASA's Oceans Melting Greenland campaign. I have been fortunate enough to have a conversation with their principal investigator Joshua K. Willis and to ask him about the mission and the interdisciplinary nature of the problem. Now, while I finish my work, the second year of the campaign is underway. For a researcher working in this field, I believe that these are the most challenging and yet the most interesting of times. Understanding the Arctic climate processes is an extremely challenging pursuit, one which demands synergy between modelling and observations; and large and small scale dynamically and thermodynamically driven phenomena. This makes me particularly eager to learn about the findings from the mission, and more importantly, to see how these observations can be used in parallel with the analytical muscle of modelling to help broaden our understanding.

This research is the culmination of a year's work carried out at the Department of Geosciences and Remote Sensing of the Delft University of Technology. This one year has made me realise that understanding the physical behaviour of a planet is exactly as complicated as it sounds, which makes a research pursuit in the field of climate physics, perhaps the most pressing and challenging issue faced by our generation. If one were to think about where to begin their academic journey to broaden their horizons and to take on problems of such magnitude, I feel extremely humbled and privileged to say that I have been a part of one of the most prestigious technical universities of our planet and the wonderful GRS family that I have been calling my home for these past two years. What that meant for me as a student was that I got to learn from professors who are at the absolute forefront of their research field. I would, therefore, take this moment to thank the GRS staff and the faculty members for providing me with the necessary insight, resources and well wishes without which I would not have been able to complete this project.

If I follow up on my argument that a pursuit in the field of climate science is interdisciplinary, then for my research, I was fortunate enough to have in my graduation committee, four of the finest professors and researchers from the fields of climate modelling, physical oceanography and physical and satellite geodesy. I would first of all like to specifically acknowledge the contribution of my daily supervisor Dr. Miren Vizcaino, and thank her, for her invaluable guidance throughout the course of my project. She allowed me to express myself, while at the same time, taught me how a research is and should be carried out. I truly believe that only a very few people are skilled/gifted at this art, and for this reason, she has my deepest gratitude. I also cannot thank her enough for moulding and improving my scientific approach, finding time to answer my questions and giving me weekly feedback on

List of Acronyms

AW   Atlantic Waters

PW   Polar Waters

NAO   Northern Atlantic Oscillation

SPNA   Sub-Polar North Atlantic

AMO   Atlantic Multidecadal Oscillation

GCM   General Circulation Model

OHC   Ocean Heat Content

SMB   Surface Mass Balance

STW   Subtropical Waters

NAC   Northern Atlantic Current

WSC   West Spitsbergen Current

EGC   East Greenland Current

RAW   Return Atlantic Water

NAD   North Atlantic Drift

IC   Irminger Current

NIIC   Northern Icelandic Irminger Current

DW   Deep Water

ISOW   Irminger Sea Overflow Waters

DSOW   Denmark Strait Overflow Waters

CFS   Cape Farewell Section

WGC   West Greenland Current

IMW   Irminger Mode Water

NAMW   Northwest Atlantic Mode Water

T-S   Temperature-Salinity

SIC   Sea-Ice Concentration

CEEMDAN   Complete Ensemble Empirical Mode Decomposition with..
..   Adaptive Noise

IMF   Intrinsic Mode Function

MLD   Mixed Layer Depth

Contents

List of Figures

List of Tables

1
Introduction

The purpose of this chapter is to introduce the reader to the geography of Greenland and the Greenland Ice-Sheet (GrIS) [our study area] along with illustrating the inducement behind the research. This is followed by an overview of the research that has been done in the respective domains of Atmospheric Science, Physical Oceanography and Cryospheric Science which helped us to formulate the parameters for our research. Lastly, we conclude the section by outlining our research objectives.

1.1   Introduction to the Study Area

Greenland is an autonomous country which lies between the Arctic and the Atlantic Ocean. It stretches from latitude 59° to 83° North and longitude 11° to 74° West and is the world's largest non-continental island. Bordering Greenland are the Atlantic Ocean and the Greenland Sea to the South-East and East respectively, the Baffin Bay lies to the West and the North is guarded by the Arctic Ocean. Also to the West and South-West across the Baffin Bay lies the first nearest neighbour in the name of Canada and to the East, across the North-Atlantic Ocean, Iceland.Figure 1.1 depicts the Geographical location of Greenland.

Figure 1.1: The geographic location of Greenland on the globe. Source: Wikipedia [1]

The Greenland Ice-Sheet is a vast ice body that occupies 80% of the total surface area of Greenland, which in numbers, equals roughly 1,710,000 square kilometers. The

ice-sheet spans for 2400 kilometres in the North-South direction and it's width, near the Northern Margin, hits its peak at 1100 kilometres at a latitude of 77° North.The thickness ranges from over 2 kilometres to over 3 kilometres at the thickest region. There are also several small ice-caps and isolated glaciers around the margin that cover around 76,000 to 100,000 square kilometres. Figure 1.2 depicts the outline map of the Greenland Ice Sheet along with the Ice-Sheet thickness.
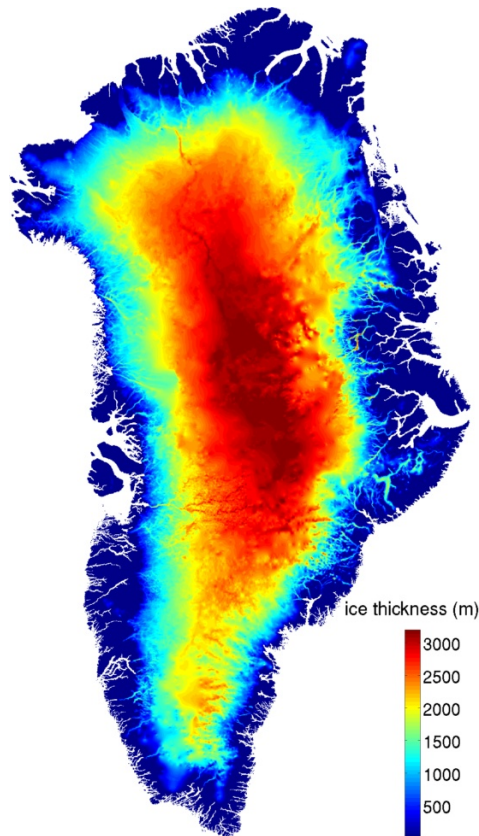
Figure 1.2: The Greenland Ice Sheet along with the ice sheet thickness (shown in meters above the mean sea-level). Source: BedMachine Greenland (Mass Conservation Dataset) [2]

The Koppen Climate Classification system divides Greenland into having two climate types namely the Ice-Cap climate observed over the Ice-Sheets and the Tundra climate seen elsewhere. Furthermore, the lowest mean annual temperatures of around -31°C are recorded at the North-Central part of the North dome whereas, at the crest of the South Dome, temperatures are around -20°C.

1.2 Motivation and Relevance

Surface Temperature records that have existed since the 1880s have shown that our planet is warming, and in 2016, the observed warming was more pronounced than the preceding years making it the third year in a row to set a new record for globally averaged surface temperatures (Potter, 2016 [3]). The Cryosphere of our planet responds strongly to the ongoing global warming leading to the Arctic Amplification

of Global Warming. An important region within the cryosphere is the Greenland Ice Sheet which has been losing mass due to increased melting and runoff which has been well documented through GRACE measurements showing a mass loss of around -230±12 Gt/yr for the period 2003-2009 and an acceleration of this mass loss of -10±6 Gt/yr^2 (Luthcke et al., 2013 [4]). This accelerated melting over the GrIS owing to a warming planet further floods the Northern Atlantic with freshwater thereby altering its density potentially leading to a weakening of the Meridional Overturning Circulation (MOC) (Hua et al.,2011 [5]) which can further have greater repercussions towards the regional and global climate states.

Furthermore, it has been documented that the Greenland Ice Sheet's contribution to sea-level rise has doubled over the last decade due to increased melting and, in part, due to the widespread acceleration of outlet glaciers around Greenland (Straneo et al., 2013 [6]). Nick et al., 2013 [7] has predicted that the contribution of these marine terminating glaciers of Greenland towards Sea Level Rise would be around 19 to 30 millimeters by the end of year 2200. One of the proposed mechanisms explaining this acceleration are the changes in the amount of heat that is supplied to the GrIS from warm subsurface Atlantic waters that carry heat from the tropics towards the higher latitudes. Holland et. al. 2008 [8] and Joughin et. al. 2012 [9] have indicated that warmer subsurface waters reaching the fronts of the outlet glaciers can result in increased submarine melting which modifies the force balance at the glacier edge. The resulted glacier accelerating results in increased ice discharge to the ocean and a net contribution to sea level rise.

Thus, at this juncture, understanding the climate of the GrIS and its arctic surroundings is becoming imperative to address the issues related to global sea-level rise and the future climate state of the planet.

1.3 A brief record of submarine melting of Greenland's tidewater glacier

The aforementioned (subsection 1.2) notion of oceans playing a large role in melting the tidewater glaciers around Greenland and ice-sheet destabilization dates back to the early 1970s but has only recently gained momentum in the last decade owing to its implication to the global sea level rise. Several research works have been carried out within the domain of Ocean-Ice interactions around the Greenland Fjords in the last few years. In this section, we classify these research based on their consideration of glacier dynamics and the relevant spatial scales.

Glacier's response to variability in the ocean heat forcing:

Andersen et al., 2011 [10], by using sand grains as a proxy for iceberg discharge, depicted a record of calving activity dating back to 1890. The record demonstrated large variability in calving rates but the present high was reproduced only in 1930s. Comparing this with climate indices indicated that high calving activity coincided

with a strong influence of Atlantic Waters (AW) and a lower influence of Polar Waters (PW) on the shelf of Greenland along with warmer summers and a negative Northern Atlantic Oscillation (NAO) phase. Furthermore, they provided evidence that Helheim Glacier responds to short-term fluctuations of large scale oceanic and atmospheric conditions on timescales of 3-10 years.

Nick et al., 2013 [7] used a glacier flow model to simulate the behaviour of four major marine-terminating outlet glaciers to document the corresponding sea level rise in changing climate scenarios. The atmospheric and oceanic forcing was applied from a mid-range future warming scenario which predicts a warming of 2.8°C by 2100. They projected a contribution of 19-30 mm from these four glaciers by 2200. For a more extreme future warming scenario (4.5°C by 2100) the projected losses increase by more than 50% producing a cumulative sea level rise of 29-49 mm by 2200.

Fjord-Scale warming and glacier retreat:

Rignot et al. 2010 [11] documented the rates of summer submarine melting through measurements of temperature, salinity and ocean currents near the calving fronts of several glaciers in Central Western Greenland coupled with ice-front bathymetry. Through water mass and heat-budget calculations, they documented a rate of 0.7±0.2 to 3.9±0.8 m/d. which were two orders of magnitude larger than surface melt rates, but comparable to rates of iceberg discharge. They concluded that ocean waters melt a considerable, but highly variable, fraction of the calving fronts of glaciers before they disintegrate into icebergs, and concluded that submarine melting must have a profound influence on grounding-line stability and ice-flow dynamics.

Noticeably, Holland et al. 2008 [8] presented hydrographic results explaining the transition of the Jakobshavn Isbræ (JI) from slow thickening to rapid thinning in 1997, concurrent with a doubling of the glacier velocity. A sudden increase was observed in the subsurface ocean temperatures in 1997 along the entire west coast of Greenland. This increase was attributed to the arrival of the warmer waters of the Irminger Sea origin on the continental shelf along Western Greenland and JI.

Studies along similar lines were carried out by Johannessen et al., 2011 [29] around the Sermilik Fjord where the Helheim Glacier terminates. The region close to the mouth of the glacier is usually inaccessible because of the heavy ice-traffic resulting from the drifting icebergs and seasonal ice in the inner parts of the fjord. Three summer expeditions were therefore carried out from 2008-2010 in the Sermilik Fjord where the observations showed that the waters in the fjord were exposed to a relatively warmer and saline subsurface Atlantic Waters which were shown to stem out from the Irminger Current. These waters, below 300 meter depth, had temperatures more than 4°C and a salinity of 34.8 psu. An annual time series of all oceanographic stations, off the Eastern Greenland coast, since 1970, was used to construct a proxy for the fjord temperatures at 400 meters depth with the assumption that the temporal variability of the temperatures in the Irminger Current would be representative of the variability of the Atlantic Waters present in the fjord.A lagged cross-correlation

showed that the ice-front movement lagged the proxy temperatures by one year showing a maximum correlation of r ~ -0.49 and that at least 24% of the ice-front movement could be explained by the proxy variation of the warm AWs.

Fjord-Shelf Exchange:

Straneo et al., 2009 [12] carried out a similar study as Johannessen et al.,2011 [29] in the Sermilik Fjord. The study was based on the observations collected in the months of July and September, 2009. Two moorings were deployed in the middle of the fjord for the period in between the survey. Results from the campaign showed that there were large volumes of warmer AW present both inside the fjord and on the East Greenland shelf near Sermilik during both the months. Studying the changes in the water properties from the two periods and combining it with the ocean current measurements from the moorings allowed the author to conclude that the warmer Atlantic Waters were being rapidly replenished through exchange with the East Greenland shelf. The authors further suggested that the northeasterly wind events are the drivers of this exchange. These winds tend to push the warm Atlantic Waters close to the fjord mouth and create strongly sheared flows inside the fjord. This circulation is typical of narrow fjords and is a more effective heat transport phenomenon than an estuarine circulation (Refer Theory: Estuarine Circulation, subsection 2.1.4) [Klinck et al.,1981 [13]; Stingebrandt, 1990 [14]].

Basin-Scale Atlantic Water variability:

While there is a distinct lack of historical data from the Sermilik fjord, the contrast along the Southern and South-Western Greenland continental shelves is well documented through observations (repeated hydrographic sections) in the past decades (Sutherland and Pickart, 2008 [15]; Holland et al. 2008 [8]; Hanna et al. 2009 [16]). Observations have shown that waters around these continental shelves were much colder prior to the mid-1990s which now contain signatures of warm water from the tropics in large volumes owing to an anomalous intrusion of relatively warm and saline AWs into the subpolar region (Hatun et al.,2005 [17]). This follows from the observed warming of the Irminger Current and the North Atlantic Subpolar Gyre's interior (Myers et al. 2008 [18]; Yashayaev et al. 2007 [19]) and the slowdown of the gyre observed over the last decade (Häkkinen and Rhines, 2004 [20]).

This warming of the Sub-Polar North Atlantic (SPNA) is expressed as an increase in the upper ocean (500-1000 meters) heat content (Figure 1.3 **c**). This intrusion is driven by the shifting wind patterns over the North Atlantic (Häkkinen and Rhines, 2004 [20], Hakkinen et al.,2011 [21]) which in turn correspond well with the wintertime atmospheric block over Greenland and also Western Europe (Hakkinen et al.,2011 [21]).
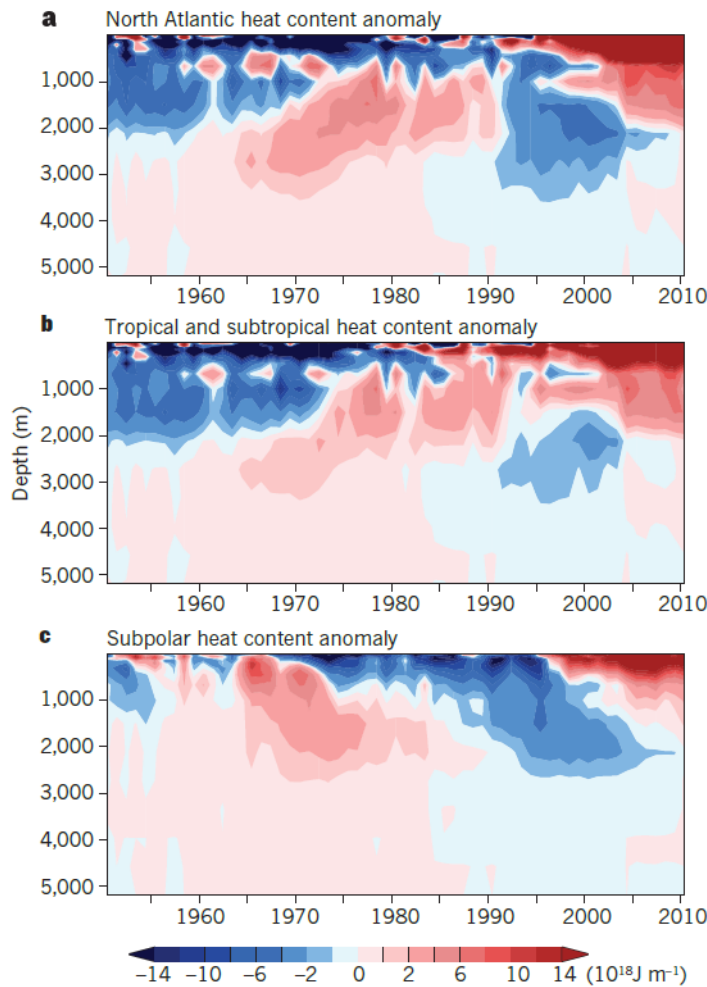
Figure 1.3: a) Heat Content Anomaly for the entire North Atlantic. **b)** Heat content anomaly for the subtropical and tropical regions. **c)** Heat Content anomaly for the subpolar regions. The period ranges from 1950-2010. The time mean from 1950-2010 is used to define the anomaly over each depth. Over the course of this period, the data coverage from depths of 700 meters and below is sparse adding significant amount of uncertainties. Source: Williams et al., 2013 [22].

A dominant atmospheric variability mode over the North Atlantic is the North Atlantic Oscillation (NAO), wherein, a negative NAO phase leads to a cooling of the Subtropical North Atlantic and simultaneously a warming of Subpolar North Atlantic with increased flow of warmer subtropical waters towards Greenland's margins (Lozier et al.,2008 [23]). From the early 1950s till 2000s, such a behaviour has been used to explain the simultaneous and opposing changes in the subpolar and subtropical gyre's heat content anomalies of the upper ocean (500-1000 meters) (Figure 1.3 **b** and **c**), attributing the cause of the SPNA warming and the AW variability close to the Greenland margin to changes in the NAO cycles (Visbeck et al.,2003 [24], Holland et al.,2008 [8]). However, since the late 1990s, both the Subpolar and Subtropical regions have been gaining heat simultaneously (Figure 1.3 **a**, **b** and **c**) and therefore such an assumption no longer holds true on its own.

The warming of the Subpolar gyre on multidecadal timescales in the North Atlantic is more strongly correlated to the Atlantic Multidecadal Oscillation (AMO) Index (Polyakov, I.V. et al. 2005 [25]; Reverdin, G., 2010 [26]). The absolute AMO signal is further governed by the global sea surface temperature rise (Trenberth et al.,2006 [27]) which could explain its strong correlation with the warming of the SPNA, however, this correlation exists even after the warming trend of the global sea-surface temperature is removed (Figure 2.7 **c**) (Hakkinen et al.,2011 [21]).

The increased inflow of the warm waters from the tropics into the subpolar region is likely causing the warming of the SPNA. We understand that the subtropical ocean is gaining in heat (Levitus,S. et al.,2012 [28]) as a result of a warming atmosphere (Figure 1.3 **b**). When the NAO shifted from a persistent positive phase to a quasi-neutral phase in the early 1990s, some of the heat from the subtropical gyre got advected to the subpolar region. Therefore, it was concluded that a warming trend over the North Atlantic Ocean (Levitus,S. et al.,2012 [28]), a warm AMO phase and the persistent winds driving the cross gyre exchange between the SPNA and the Subtropical North Atlantic is the cause of the warming of the Subpolar gyre.

Interpretation:

It can be inferred from these studies that the ocean-ice interaction, whilst previously overlooked, plays a key role in the GrIS mass budget. However, our knowledge about the properties of the ocean waters reaching Greenland's tidewater glaciers and triggering their acceleration has been extremely limited because of lack of in-situ observations around these locations. On shorter timescales, the observations from these fjords have a sufficient temporal resolution, however, they span a few summer profiles at best. Therefore, the task of linking the sparse subset of observations to the variability in the climate system and the physical processes which manifest themselves on decadal to multi-decadal timescales becomes a challenging task. Furthermore, on longer time-scales, most of the traditional hydrographic sections around Greenland and the Northern Atlantic are usually captured once a year which means that they alias seasonal variability. Another important coupling is the response of Ocean towards changes in the atmosphere around the North Atlantic. The synthesis from the above studies makes it self-explanatory that more observations are needed to monitor the inflow of warm subtropical waters towards the poles, on the continental Greenland shelves and inside the glacial fjords at the ice-ocean interface. At the same time, it is also important to bridge the gaps using modelled results to strengthen our understanding of the ocean forcing and its variability around these tidewater glaciers. This leads us to the formulation of our primary research objective, from which, three research questions are proposed:

Can GCMs be used to bridge the data gaps and put the hydrographic observations into perspective? Can they be used for making reliable projections of subsurface ocean heat forcing?

1.4   Research Questions

The overview of the research carried out on this subject guided the formulation of the objective of this thesis. As explained above, most of the work in literature corresponds to observations taken during summer expeditions and short cruises spanning for a period of 3-5 years. To put these results into perspective, a much larger timescale needs to be considered to attribute recent changes to anthropogenic forcing. For reliable projections of future evolution of GrIS it is necessary to comprehensively address the spatial and temporal distribution of the warmer subsurface Atlantic waters. In this study, the spatio-temporal variability and trends in the Ocean Heat Forcing is investigated using results from two different General Circulation Models (GCMs), namely the HADGEM2-ES and GISS-E2-R, in the vicinity of three selected major outlet glaciers in South West and South East Greenland in pre-industrial, historical and future climate scenarios. We further target several specific questions as mentioned below:

1) *How reliable are the Global Circulation Models in simulating the Ocean Heat Forcing to the GrIS?*

The modelled Ocean Heat Forcing is dependent on how the model simulates the ocean circulation around Greenland. To evaluate this, we examine the vertical and zonal variations in sea-water potential temperature (T) and salinity (S) for our study locations around Greenland. The observational record so chosen spans from 1950-2005, with sparse data coverage during the winter months of December-February. The modelled hydrographic sections of T and S, are therefore, extracted from the Historical Experiment (1950-2005) for the months of March-November. We use a regridding approach which takes as input the high-resolution CTD observations of Temperature-Salinity. The model grid information along longitude and depth is used to define an interrogation window that adapts to the inconsistent spacing between the modelled depth levels. Inverse distance weighting is applied within the window to interpolate the observed values onto the modelled grid. This is used to inspect if the model is able to capture the advection of heat and salt from the warm and saline AWs onto the Greenland Shelf, and close to where the prominent tidewater glaciers terminate.

2) *What is the spatial variability of the different water masses along our study regions and how does it evolve under anthropogenic GHG forcings?*

We compare the water mass signature anomalies in Historical (A.D. 1985-2005) and RCP 8.5 (A.D. 2075-2095) experiment with respect to the Pre-Industrial simulations to establish the response of the dominant currents to GHG forcing. Through our results, we address the change in the spatial distribution of the warmer subsurface Atlantic Waters, which are present on the Greenland continental shelf close to our study locations. Emphasis is given on addressing how and why these responses vary across our study locations.

3) ***What is the temporal variability of the Ocean Heat Content (OHC) around our study locations and how does it evolve under anthropogenic forcing?***

To determine the natural variability in the modelled monthly OHC time-series, we use a pre-industrial scenario over a 90 year period. Using the historical and RCP 8.5 simulation (90 year period), we quantify the anthropogenic-sourced long-term trend in the modelled OHC. We use CEEMDAN (Complete Ensemble Empirical Mode Decomposition with Adaptive Noise) to decompose the OHC time-series into Intrinsic Mode Functions (IMFs), to discern and quantify the high-frequency (intra-annual) variability of the OHC from the multi-year variability and trend. Marginalised Hilbert Spectrum of the modes is used to quantify changes in the signal energy arising from GHG forcings with respect to the Pre-Industrial climate.

1.5 Outline

In Chapter 2, we first provide a brief overview of the principle mechanism of submarine melting of tidewater glaciers. We then explain the mechanisms within the fjord that drive the glacier sensitivity towards submarine melting and the fjord-shelf exchange. This is followed by a brief overview of the ocean circulation and currents around Greenland.

In Chapter 3, we introduce our study locations and elucidate the motivation behind our selection. After that, the setup of the two GCMs used in our study is explained along with the different climate scenarios. We then explain the high-resolution CTD data profile and the formulation of our downsampling technique. This is followed by the methodology pertaining to how changes in the spatial and temporal variability in the Ocean Heat Forcing were computed.

In Chapter 4, we present our results which is broadly categorised in three parts. In the first part, we present results from the evaluation of the HADGEM2-ES and GISS-E2-R models. Changes in the spatial and temporal variability in the Ocean Heat Forcing is presented in the second and third part of the chapter respectively.

In Chapter 5, we revisit and answer each of the research objectives proposed in the introduction chapter and provide our recommendations for further research in line with our study.

2

Theory

2.1 Introduction to Submarine Melting of Tidewater Glaciers around Greenland

2.1.1 Submarine Melting: Principle Mechanism

Several glaciers along the coast of Greenland terminate in tidewater in deep sea or with a floating ice-shelf which extends for 100-200 meters below the sea level, in long and narrow fjords that connect them to the continental shelf (Figure 2.1). These glaciers, referred to as tidewater glaciers or floating ice-tongue glaciers respectively, interact with the ocean waters at the calving front.
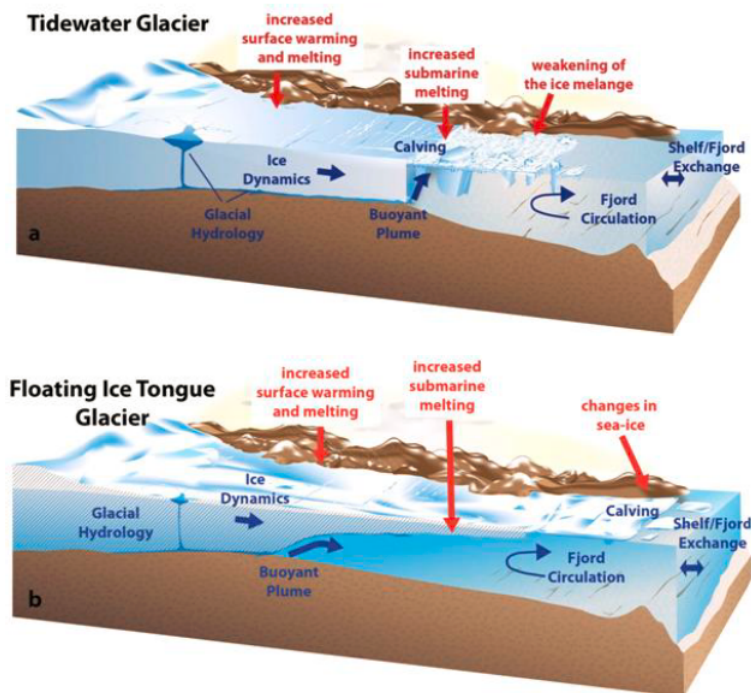
Figure 2.1: a) Tidewater Glacier and a **b)** Floating Ice-Tongue Glacier. The illustrations have been obtained from Straneo et al., 2013 [6]

Looking along the periphery of an ice sheet, the waters close to the surface of the ocean, referred to as Polar Waters (PWs), tend to be both fresh and cold (Figure 2.2). In their natural state, they can typically be close to the surface freezing point

($\sim$ -1.8°C). These waters tend to show only a moderate impact on triggering any subsurface melt of the floating ice-shelf.
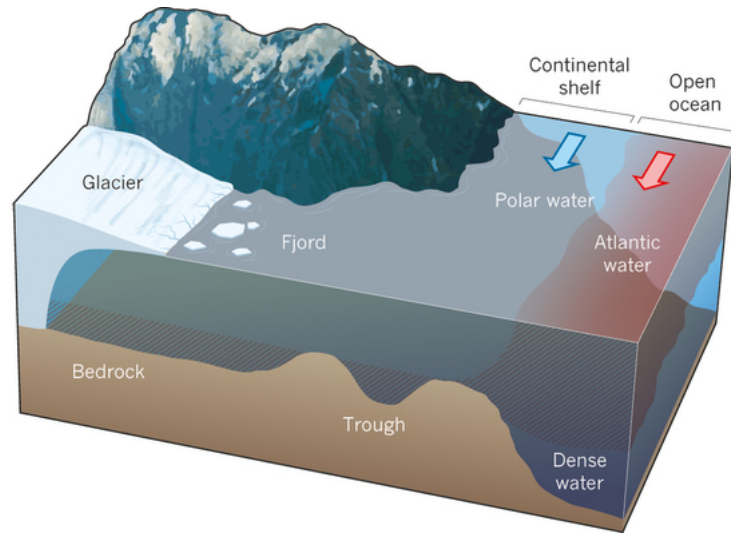
Figure 2.2: Two major water mass types found inside the Greenland fjords. The subtropical warm and saline AWs (depicted in red) that circulate around the SPNA, cross the continental shelf and reach the glacial fjords of Greenland at depth, where they meet the fresh PWs (blue) that originate from the Arctic flowing close to the coastline. The exchange between the fjord and the shelf (glacier-ocean) entails a varied range of spatial and temporal scales [Source: Straneo et al., 2013 [6]].

The waters sitting below the PWs are much more warm and saline compared to the PWs and their origin can be traced back to the subpolar and subtropical regions. Owing to the greater salinity, these water masses are denser than Polar Waters despite being warmer causing them to sink below the surface when they arrive closer to the polar regions (Figure 2.2). These waters are referred to as the Atlantic Waters (AWs). These warm and saline AWs trigger dynamic changes at the marine terminating margins of the GrIS where they come in contact with the floating ice-shelf, causing rapid melting, which is referred to as submarine melting, with melt rates in the order of a tens of meters/year (Figure 2.3).

2.1.2 Glacier's response to Submarine Melting

There has been a fourfold increase in the observed mass loss from the GrIS. The observed rate from 1992-2001 was reported to be 51 ± 65 Gt/yr which for the 2002-2011 period was 211 ± 37 Gt/yr (Shepherd et al., 2012 [32], Hanna et al., 2013 [33]) . For the combined period from 1992-2011, this has led to an observed global mean sea level rise of 7.5 ± 1.8 mm attributing Greenland to account for a quarter of the global slr (Shepherd et al., 2012 [32], Hanna et al., 2013 [33]).

Two processes, both of which contribute substantially, are responsible for mass loss from the GrIS (Van Den Broeke et al.,2009 [34], Krabill, 2004 [35]). Around Western

and South-Eastern Greenland, the thinning and rapid retreating of multiple tidewater glaciers resulted in an increase in the discharge of ice (Figure 2.7) (Sole et al.,2008 [36]). Furthermore, an increased surface melting resulted in a negative surface mass balance (SMB) (Figure 2.7) (Van Den Broeke et al.,2009 [34], Hanna et al., 2011 [37]). Most of the glaciers in the south attained their peaks in terms of velocity in the year 2005 but have since slowed down(Moon et al.,2012 [38]). However, the discharge still appears to be greater when compared to the mid 1990s(Moon et al.,2012 [38]) with significant spatial differences within the same region. Observations from atmospheric and oceanic components have shown considerable warming which is synchronous with the widespread changes that have been observed in the Greenland SMB and the rapid discharge of ice at the marine terminating glacier margins, indicating a direct response of the GrIS to external forcings. For the decrease in Greenland SMB, these external forcings involve increasing air temperatures above the GrIS along with spatially varying precipitation patterns (Hanna et al.,2013 [33], Hall et al.,2013 [39]), whereas, the increased discharge of ice is dictated mainly by the inflow of warm ocean waters into the fjords and the role-play of various fjord-scale dynamic/thermodynamic processes.

2.1.3 Ice-Ocean Interface Dynamics

The exchange of heat across the ice-ocean interface is a turbulent phenomenon depending on molecular scale processes. This signifies that not all the heat from the fjords are drawn into melting the glaciers. Thus, an increased submarine melt rate is not directly dependent on a warming of the waters in these narrow fjords.

Subglacial Discharge and the role of Buoyant Plumes:
The presence of a stable boundary layer insulates the ice partially from the AWs. For a rapid melting of the glaciers to occur at this interface, intense turbulent flows are usually required to disrupt the formation of such a stable boundary layer. The surface melting of the ice causes the fresh glacial meltwater to percolate to the base of the glacier which then flows from beneath the glacier (subglacial discharge) into the ocean (Figure 2.1). Owing to a difference in density between the fresh meltwater and the ocean water, it rises up buoyantly, where the turbulent mixing of the plume with the warm ocean waters at depth leads to the plume gaining in temperature as it rises up (Figure 2.3). Furthermore, along the face of the glacier, submarine melting causes a similar release of buoyant freshwater plumes. It is the property of the plume that largely governs the heat and salinity exchange, which are, in turn, governed by the temperature, salinity and buoyant velocity of the plume along with glaciological parameters related to the geometry of the ice front and/or roughness of the surface. Furthermore, the enhanced summertime surface melt of the ice enhances the subglacial discharge, catalysing the turbulent mixing, and therefore increasing the observed submarine melting. Therefore, even with insignificant seasonal variations in the AW temperatures in the fjords, the submarine melting may increase substantially during the summer months.
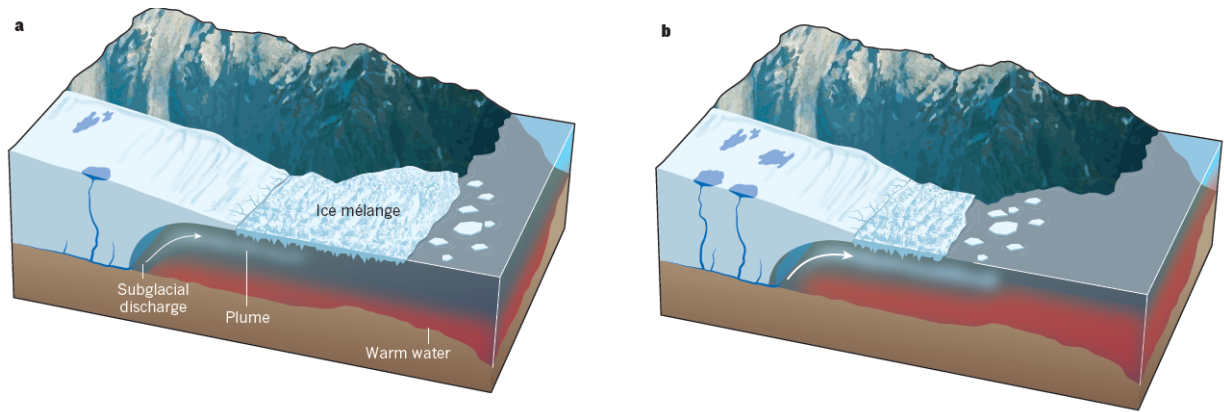
Figure 2.3: a) Conditions prior to retreat with relatively cold PWs, thick cover of ice melange at the marine terminating margin and a controlled subglacial discharge. **b)** Retreat conditions comprise of warm subsurface AWs combined with an increase in the surface melt resulting in an increased submarine melting. This is also visible from the weakening of the ice melange.

2.1.4 Fjord Scale Mechanisms influencing Glacier Sensitivity towards Submarine Melting

Ice Melange:

Most of the fjords in Greenland are completely filled with a melange of icebergs and sea ice (Figure 2.3). These extensively filled ice melange regions extend hundreds of meters deep in the water. For the warm ocean waters to reach the terminus of the glacier, it has to compensate much of its heat to melt the melange. Thus, the presence of a thick and dense melange covers directly affects the submarine melt rates while also showing a strong seasonal cycle. During the winter months,as the sea ice concentration increases, the constituent icebergs are bound together as rigid amalgamated masses. As the terminus of the glacier advances, this mass is thrusted down the fjord. In the summer months, as the sea ice concentration reduces, the bond between the amalgamated mass weakens causing the melange constituents to float separately. The wintertime amalgamation is known to greatly reduce calving. Remobilization of the melange with the onset of summer allows it to exit the fjord. Such a seasonality has been observed at Jakobshavn where the glacier terminus has been seen to advance during the winter season and retreating again in the summer. This results in an annual variation of speed close to the terminus of the glacier by around 20-30 percent (Joughin et al.,2008 [41], Amundson et al.,2010 [42]). One can, therefore, argue that the presence of warmer water in the fjords will directly influence the annual variation. By shortening the duration when the melange remains frozen makes the glacier more susceptible to calving leading to retreat. One such example was observed when a period of marginal sea ice concentration in the Disko Bay was found to be concordant with the breakup of the floating ice tongue at Jakobshavn (Figure 2.4) (Joughin et al.,2008 [41]).

Figure 2.4: Lying in between 2 rock out-thrusts, a region covered with ice melange which lies in front of the Jakobshavn Isbræ is shown.This 14 km long area covered with melange was occupied by a several-hundred meters thick ice tongue prior to early 2000s. Source:Joughin et al.,2012 [9]

Terminus Geometry of the Glacier:
The terminus geometry defines how exposed the front of a glacier is to the warm ocean waters, thereby controlling the influence of melt. A gradual retreat of the glaciers by a few 100 meters is plausible owing to an increased melting rate (1 m/year), however, observational records of retreat have shown events related to enhanced calving and rapid retreat instead of gradual melt (Howat et al.,2005, Luckman et al.,2006). Increased melt (enhanced melt rates) acts as a catalyst in producing enhanced calving by melting the ice from beneath. High melting rates of around 1 m/day observed around Jakobshavn in the early 2000s led to a rapid thinning causing the floating ice tongue to collapse which was around 15 kms long (Holland et al.,2008 [8], Motyka et al.,2011 [43]). If, on the other hand, the glacier has a grounded terminus instead of a floating overhang, the exposed glacier surface area (to warm waters) significantly reduces and melt rates of similar magnitudes are moderate compared to the 10-40 m/day mean rates achieved as a result of calving.

Estuarine Circulation:
Estuarine Circulation can be realised as a buoyancy driven circulation which are very typical of Greenland's glacial fjords. As the buoyant plume (from subglacial runoff) rises upward, it entrains ambient water and makes its way out of the fjord effectuating the inflow of ocean waters (Figure 2.5). If estuarine circulation is the dominant mode of heat-transportation in the fjords, an increased subglacial runoff would lead to more submarine melting. Such a hypothesis, that the renewal of AWs in the glacial fjords of Greenland is controlled by estuarine circulation, has not been supported through observations. Understanding the dynamics of the relationship between the buoyant plumes, the fjordic circulations and the subsequent melt rates implies coverage of the varied spatial scales (from a few mm to a few hundred km)

which is challenging, even with the high-res models. Furthermore, the unresolved processes that are parameterized in the model are not constrained well by observations (Jenkins, 2011, Sciascia, 2013) making it difficult to understand how submarine melting is impacted by the shelf driven variability.
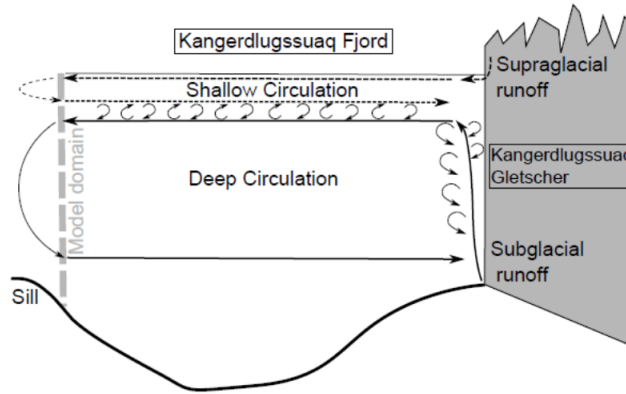
Figure 2.5: A schematic of the Estuarine Circulation around Kangerlussuaq Glacier in Eastern Greenland. Source: Sole et al.,2008 [36]

2.2 Dynamics of Fjord-Shelf Exchange

Hydrographic Variability around the Greenland Continental Shelves:
The observed increase in the discharge of ice since the 1990s is linked to the glacier retreat at the SPNA margins and the extension of the SPNA into the Baffin Bay (Figure 2.6).
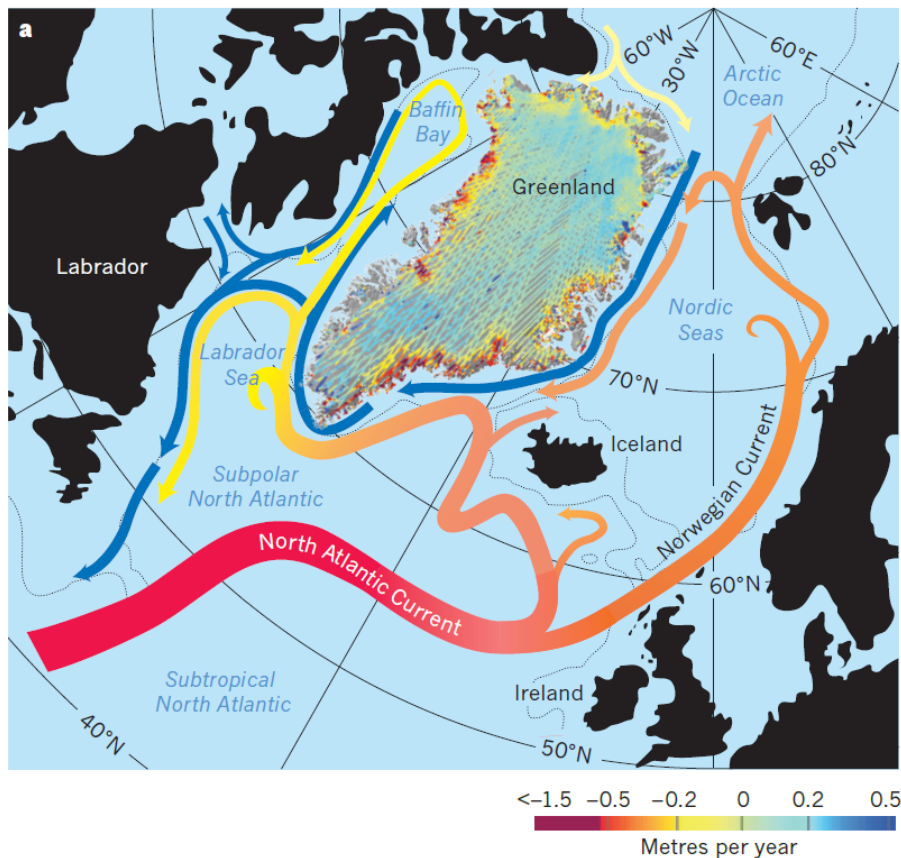
Figure 2.6: The major currents and basins around Greenland are shown. The rapid ice-discharge is concentrated around the SPNA margins. The red-yellow current lines represets the water pathways of the AWs and the blue current lines represent the freshwater pathways of the Arctic origin waters. The rates of dynamic thinning are shown in the colorbar. Source: Pritchard et al. 2009 [46]

The subtropical warm waters circulate in a cyclonic gyre around the SPNA, flowing around the Greenland and North American continental slopes. These Subtropical Waters (STWs) encircle the cold and dense waters at the interior of this gyre (Yashayaev et al.,2007 [19], Vage et al., 2011 [47]). On the Greenland shelf (200-300 m deep), the cold and fresh waters of the Arctic origin act as buffers to the warm STWs (Sutherland et. al., 2008 [15]). The SPNA began to warm rapidly in the 1990s (Bersch et al.,2007 [48], Yashayaev et al.,2007 [19], Williams et al.,2013 [22]), an observation concordant with the retreat of the glaciers (Figure 3b-d). This change is corroborated through the warming of upper 1000 meters off Western Greenland waters which includes the shelf (Figure 2.7 **b**) extending to the Baffin Bay (Zweng et al.,2006 [52]).
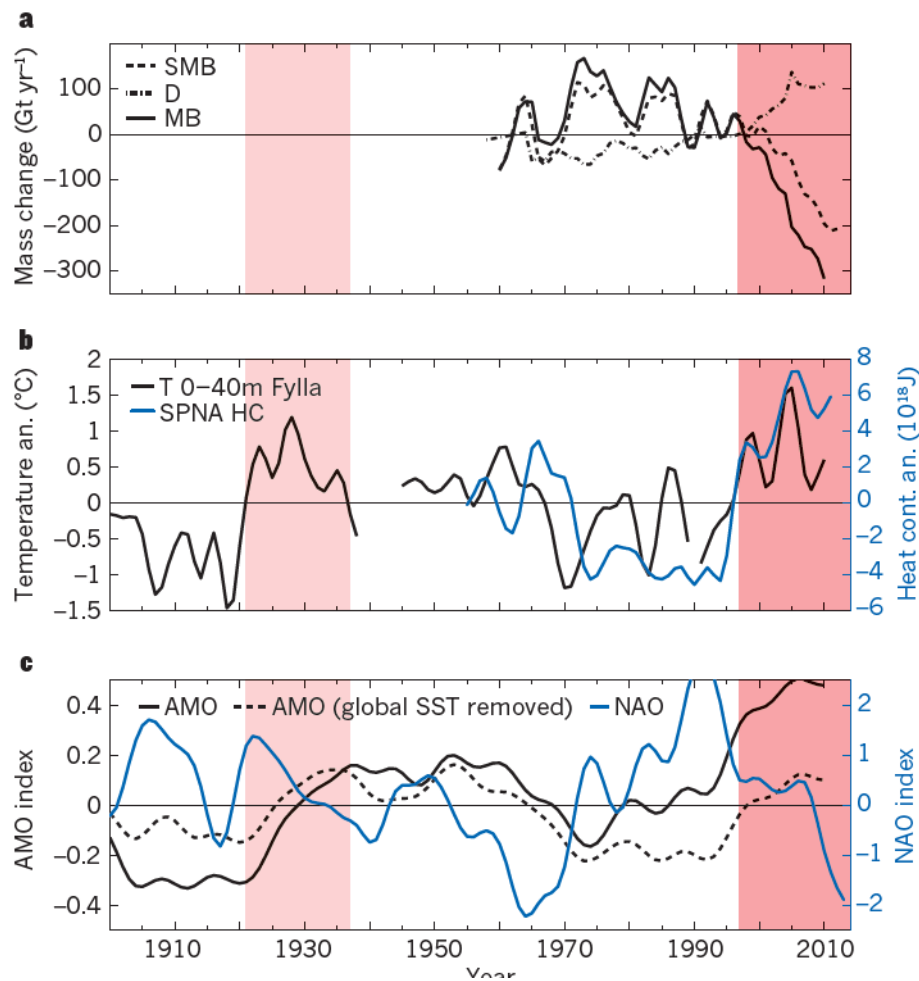
Figure 2.7: a) Surface Mass Balance (SMB), Ice Discharge (D) and Mass Balance (MB) anomalies [based on Bamber et al., 2012 and Van Den Broeke et al.,2009] in gigatonnes per year. **b)** Upper 700 meter Heat Content anomaly of the SPNA (blue) (Hakkinen et al.,2013 [49]) and Fylla Bank, Western Greeland: 0-40 meter Mean temperature anomaly (black) (Andresen et al.,2012 [10]). **c)** NAO winter index (blue) (Hurrell 1995 [50]), AMO index anomaly with the global SST trend (solid black) and without the global SST trend (dotted black) (Enfield et al.,2001 [51] and Trenberth et al.,2006 [27]. Shaded in deep red are the recent years (1990s) which marked the beginning of rapid glacier acceleration concordant with the warm period. Light red shading marks a similar period of warming (1930s). The time series have been filtered using a 5-year low-pass filter and extended to 2010. The mean wrt the period has been removed. Source: Straneo et al., 2013 [6].

Towards Southeastern Greenland, data from the annually repeated hydrographic sections reveals that the Atlantic layer is thickening substantially around the same period (1990s) which again is concordant with a similar warming seen for the waters on the shelf (Vage et al.,2011 [47]). The warming of the shelf is corroborated with the propensity of AW intrusions, where these AWs propagate into the deep troughs of the shelves across Greenland, a phenomenon which have become more frequent in recent years (Sutherland et al.,2008 [15]).

Records of Fjord-Shelf exchange:
Understanding the response of the fjords towards the warming of the shelf is abstruse owing to the lack of observational records prior to the warming of the SPNA. However, two summer profiles from Kangerlussuaq fjord (South-Eastern Greenland), one prior to the mid 1990s (1993) and one post the SPNA warming in 2004 show that the waters inside the fjord have become warmer (Christoffersen et al.,2011 [53]). Compared to the substantial weekly and inter-annual variability in the fjordic climate, these results are not representative of the long term changes.
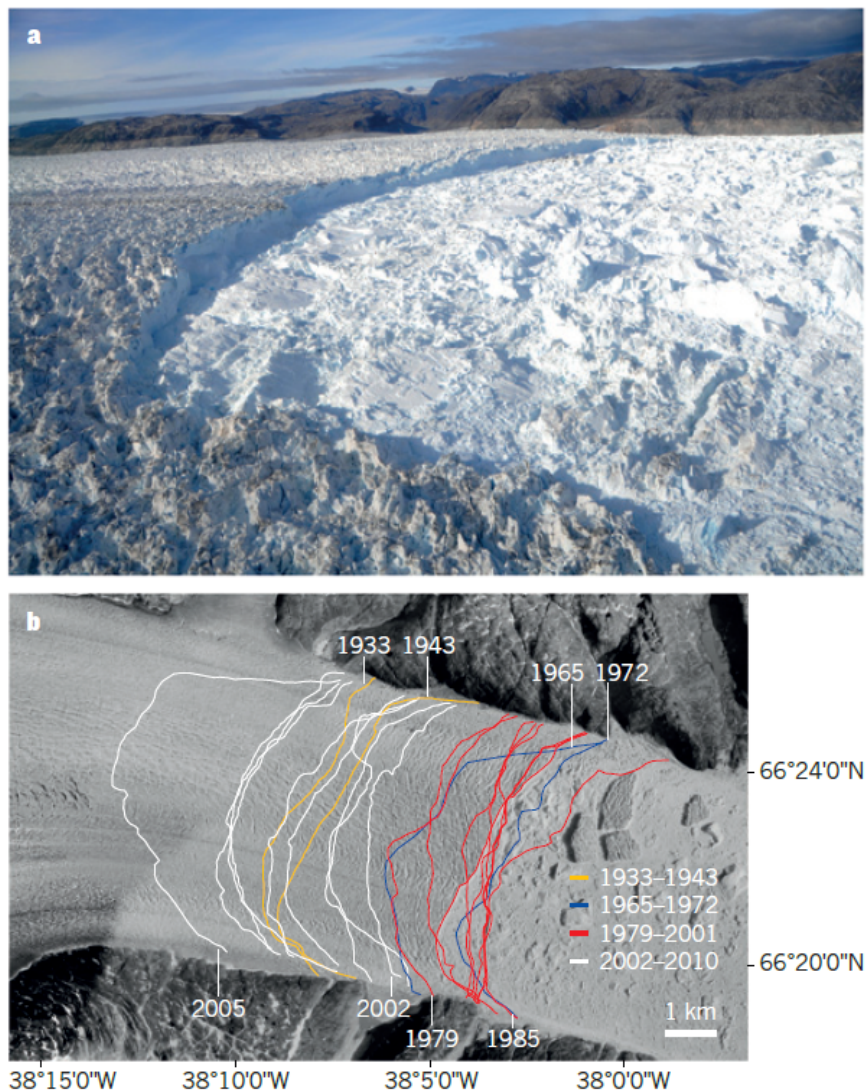
Figure 2.8: a) The terminus of the Helheim Glacier in the Sermilik Fjord, Southeast Greenland. A thick melange of ice buffers the front of the glacier which is grounded in 600 meters of water. The lower mountain reaches depict the extent of the glacier before the retreat in early 2000s.Source: Straneo et al., 2013 [6]. **b)** The retreat of the Helheim Glacier between 2002 and 2005 was more than 4 kms which is comparable to a similar retreat observed during the 1930s. Source:Andresen et al.,2011 [10]

Data collected from several fjords recently have indicated the presence of a thick subsurface AW layer, which is warm (0-4 °C) and saline, beneath the cold and fresh PW layer (Holland et al.,2008 [8], Christoffersen et al.,2011 [53], Rignote et al.,2010 [11], Straneo et al.,2010 [54], Johnson et al.,2011 [55]). Around the glacial fjords bordering the Arctic Ocean in Northern Greenland lie the coldest waters whereas the warmest is present around the glacial fjords that border the Baffin Bay and the SPNA. This is congruous with the variability of the mean AW properties on the nearby continental shelf and slope which makes them representative of the distance of the AWs from its subtropical origin (Straneo et al.,2012 [56]). As the fjords usually have a deep sill (greater than 200 meters), the typical fjord-shelf exchange around Greenland is unimpeded which makes the fjord and the shelf AW properties similar (Sutherland et al.,2013 [57], Johnson et al.,2011 [55], Straneo et al.,2012 [56]). This is further observed in the along-fjord variations which are comparatively smaller indicating that the AWs are present in close proximity to the glacier terminus. This study, however, is hindered by the presence of a thick melange of ice in the vicinity of the glacier, because of which, most of the surveys terminate 10-15 kms from the terminus (Figure 2.8).

The fjords, therefore, contained signatures of both AWs and PWs before the warming of the SPNA began in the mid 1990s. However, owing to the relatively colder shelf conditions prior to the mid 1990s, it has been argued that the AW layer was both thinner and colder. Several processes such as the estuarine circulation and tidal mixing help in rapidly flushing (renewing) the waters from the fjord. The sparse (limited) set of direct velocity observations have suggested high frequency variability dictated by fast currents (Sutherland et al.,2012 [58], Mortensen et al.,2013 [59]). Measurements from moorings and repeat surveys suggest a sub-seasonal periodicity (Straneo et al., 2010 [54], Mortensen et al.,2013 [59], Mortensen et al. 2011 [60]),indicating rapid renewal (within months) even for the larger fjords, in response to the warming of the shelf.

2.3 Ocean Circulation around Greenland

2.3.1 Modes of Northern Atlantic Current:

From South-West (of Greenland), the warm, saline and shallow Northern Atlantic Current (NAC), an extension of the Gulf Stream, enters the Subpolar North Atlantic area. Flowing northward along the western coastline of United Kingdom, it flows through the Faroe-Shetland Channel (Figure 2.9).
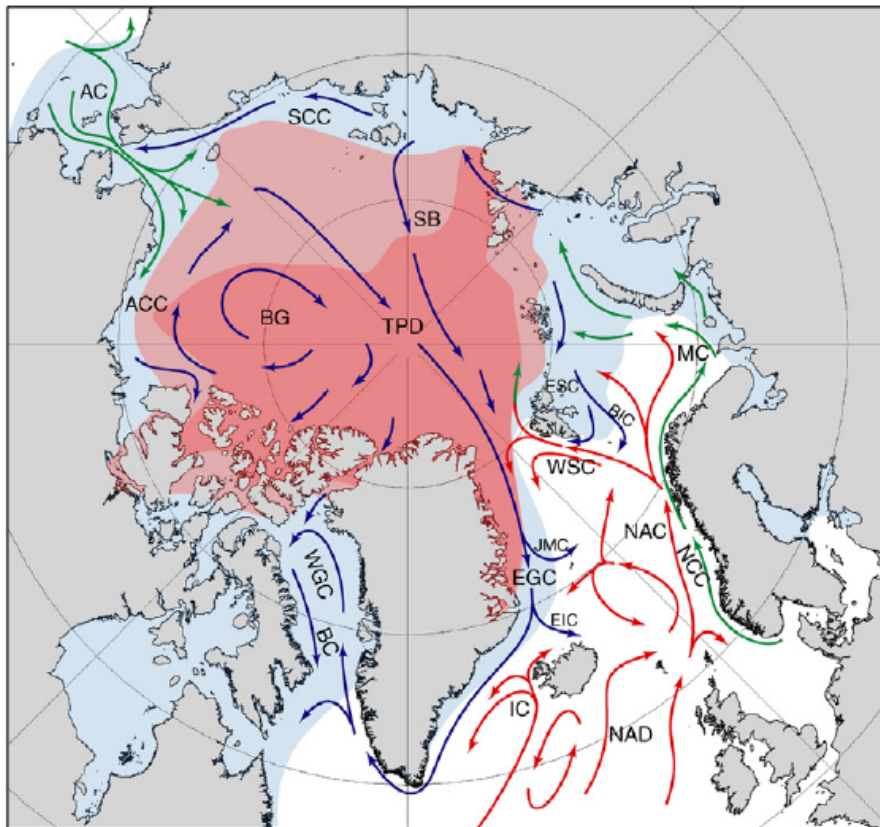
Figure 2.9: Schematic of the circulation in the Sub-Arctic and Arctic upper ocean. The abbreviations are as follows: AC: Anadyr Current; ACC: Alaskan Coastal Current; BC: Baffin Current; BIC: Bear Island Current; BG: Beaufort Gyre; EGC: East Greenland Current; EIC: East Iceland Current; ESC: East Spitsbergen Current; IC: Irminger Current; JMC: Jan Mayen Current; MC: Murman Current; NAD: North Atlantic Drift; NAC: Norwegian Atlantic Current; NCC: Norwegian Coastal Current; SB: Siberian Branch (of the Transpolar Drift); SCC: Siberian Coastal Current; TPD: Transpolar Drift; WGC: West Greenland Current; and WSC: West Spitsbergen Current. The red arrows represent the warm and saline currents of the Atlantic origin whereas the cold and fresh arctic currents are depicted using the blue arrows. The green arrows represent the transformed currents having comparatively lower salinity. The maximum and minimum ice extent is shown using blue and red shading whereas the minimum sea ice extent during 2007 is represented using a dark red shading. Source: Rudels et al.,2012a [78]

It continues its northward journey along the Western Norwegian continental slope, where at 70°N, it bifurcates into two subcomponents. One of these components heads eastward along the Northern Norwegian continental slope into the well-ventilated Barents Sea (as part of the Barents Sea Inflow). The other component follows the slope northwards to Svalbard, where it submerges under the cold and less saline surface waters of the Arctic, and continues along the northern pathway as a subsurface current (referred to as the West Spitsbergen Current (WSC)) into the Arctic Ocean (Figure 2.9). The WSC, an extension of the Norwegian Atlantic Current, is

responsible for the northward transport of warm and saline AW masses east of the Fram Strait. Furthermore, a part of the NAC is deflected over to the West (Figure 2.9), instead of following the northward route to the Arctic Ocean. Here, the NAC gets entrained with the East Greenland Current (EGC) and sinks below the Polar Waters. This underlying NAC from 150-800 meters begins its southward journey towards the subtropics and is referred to as the Return Atlantic Waters (RAW).

The NAC is also present around the southern coast of the Icelandic Shelf as the North Atlantic Drift (NAD) (Figure 2.10), where it bifurcates into two branches. One of the branch moves towards the east, where it flows through the Iceland-Faroe ridge, to the Faroe Islands. Profiling of the eastward branch of the Irminger Current was done using buoys (dropped at 100 meters) and CTD (Krauss, 1995 [61]). These buoys, upon their release off of the eastern end of the ridge, drifted into the Norwegian Sea.
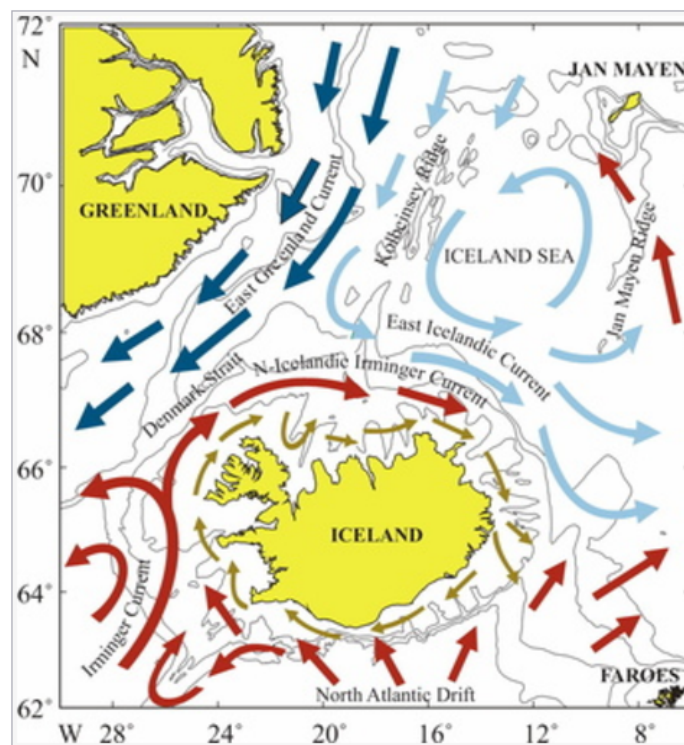
Figure 2.10: Schematic of the Irminger Current branches and Ocean Circulation around Iceland. Source: The Marine Research Institute [79]

The Irminger Current (IC) is the other branch of the NAD which heads westwards. From there, a part of this current migrates southwards following the Reykjanes Ridge (Figure 2.11) (A ridge extending from South-Western Iceland), ultimately crossing it and following a northward path along the western slope of the ridge.
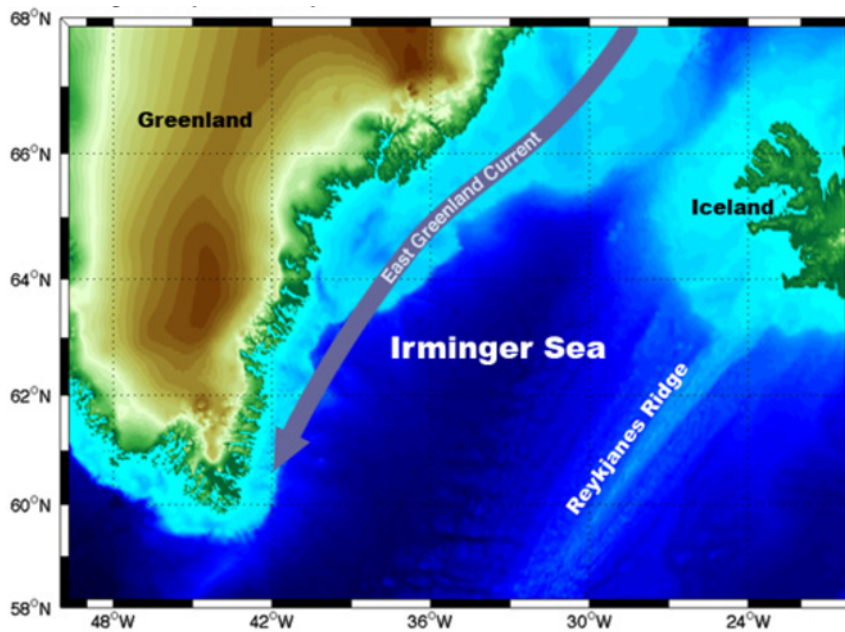
Figure 2.11: The location of the Reykjanes Ridge (an underwater mountain range extending from South-Western Iceland) in the Irminger Sea. Source: Woods Hole Oceanographic Institution [80].

The other part of this current continues on the westward path, closely tied to the Icelandic coast (Figure 2.10). As it crosses Reykjanes, it heads northwards, following the Icelandic coastline and merges with the offshore component (Figure 2.10). Ultimately, signatures of IC water masses are found on the Eastern Greenland continental slope as this current crosses the Irminger Sea and exits southward following the slope (Figure 2.10, Figure 2.9). Krauss, 1995 [61] also documented through a similar profiling of the westward component of the current that upon the release of the buoys west of 28° W, they were carried towards the Greenland slope and from there, got advected via the EGC. A substantially small fraction of the current flows through the Denmark Strait, predominantly tied over to the shelf. This current then turns eastward along the Northern Icelandic coastline (Figure 2.10) where it is referred to as the Northern Icelandic Irminger Current (NIIC).

2.3.2 East Greenland Current:

The EGC is a southward flowing current originating from the Fram Strait (between Greenland and Svalbard archipelago) and extending up to the Cape Farewell Section (Southern Greenland) (Figure 2.9). It flows via the Greenland and the Norwegian seas, and as it approaches the Jan Mayen Fracture Zone at 70°N (Figure 2.12), the upper part of this current is deflected eastwards. This is believed to occur due to an interaction of the barotropic component of the current with the bathymetry (Hopkins, 1991 [62]). This extension is suppressed during instances of strong easterly wind events. The EGC is geostrophically constrained to the continental margins of Greenland owing to the conservation of potential vorticity (Hopkins 1991). The cold and dense water masses (Deep Waters of the Arctic Origin) that are found

below 1600 meters are not able to cross the shallower ridge and propagate towards the Iceland Sea. These water masses continue circulating around the gyre in the Greenland Sea (Rudels et al 1999), further interacting with the waters present in the Greenland Sea as it makes its way towards the centre.
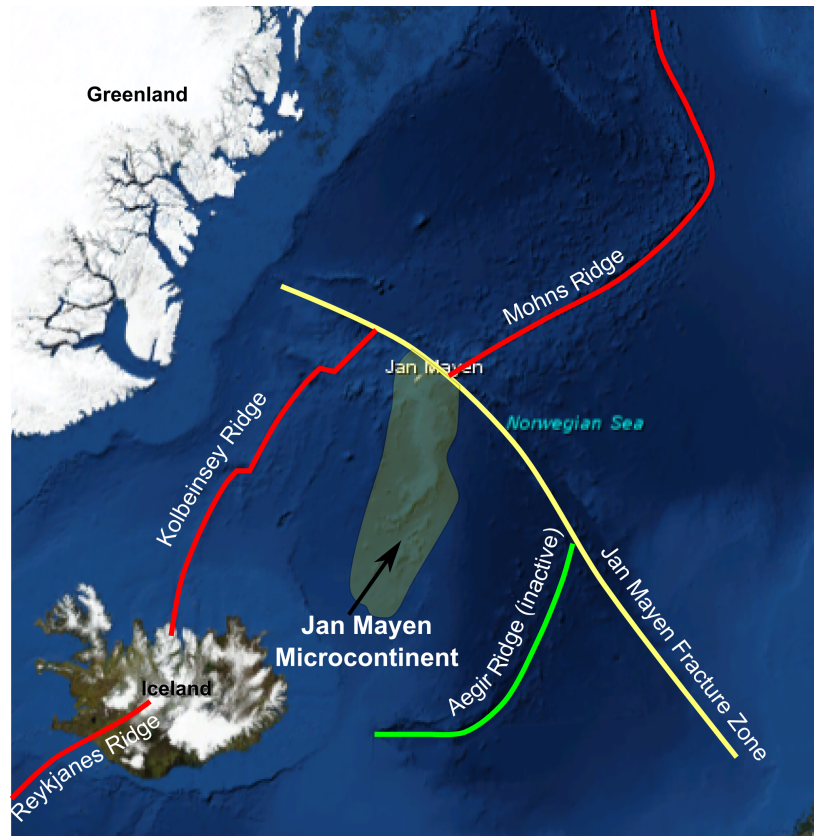
Figure 2.12: Location of the Jan Mayen Fracture Zone along with the plate boundaries. Red lines indicate active spreading centres whereas the yellow lines indicate the inactive ones. Image was acquired as a screenshot from the NASA WorldWind software. Source: Jan Mayen Microcontinent, Wikipedia [81].

Water mass classification of the EGC shows the presence of three broad categories (Aagaard and Coachman, 1968a [63]). The upper $\sim$ 150 meters comprise of Polar Waters (PWs) originating from the Arctic Ocean, which are cold (-1.8 °C - 0 °C) and fresh. The layer is marked by a strong halocline owing to a strong salinity gradient which varies from 30 psu at the surface to around 34 psu at 150 meters. Below the PWs are the Return Atlantic Waters (RAWs) extending from 150 meters to a depth of around 800 meters. They are characterized by temperatures that remain above 0°C and salinity that ranges from 34 psu (at 150 meters) to 34.88/35 psu at depths, usually reaching a maximum at around 400 meters, after which, the salinity does not show significant variability. The last water mass category is the Deep Water (DWs) which are present below a depth of 800 meters. These DWs are both cold and saline and circulate cyclonically in the Greenland Sea (Aagard and Coachman, 1968b [64]). Their temperatures are usually below 0°C and the salinity varies from 34.87-34.95 psu.

The EGC being the only prominent southern current pathway is also responsible for the export of ice from the Arctic Ocean. Owing to the high velocities of the EGC surface current, it is able to carry sea ice and cold PWs southwards through the Fram Strait. More than 90 percent of the sea ice export through this pathway is accredited to the EGC (Woodgate et al. 1999, Rudels et al. 1999). Furthermore, as the EGC is fed by the warm and saline RAWs, it results in the suppressing the formation of ice in the current as the entrainment of saline waters in a region of strong cooling results in the destabilization of the column of water (Aagaard et al., 1985 [65]).

2.3.3 Deep Water Formation:

The Irminger Sea Overflow Waters (ISOW) and the Denmark Strait Overflow Waters (DSOW) are highly dense water masses which originate from the very well-ventilated Arctic Seas. Their density is substantially higher compared to the Northern Atlantic waters found at similar depths. The DSOW is colder than the ISOW and it outflows along the shelfbreak, through the 640 meters deep Denmark Strait, where they meet the warm and saline waters of the subtropics recirculating in the Irminger Sea (Figure 2.13).
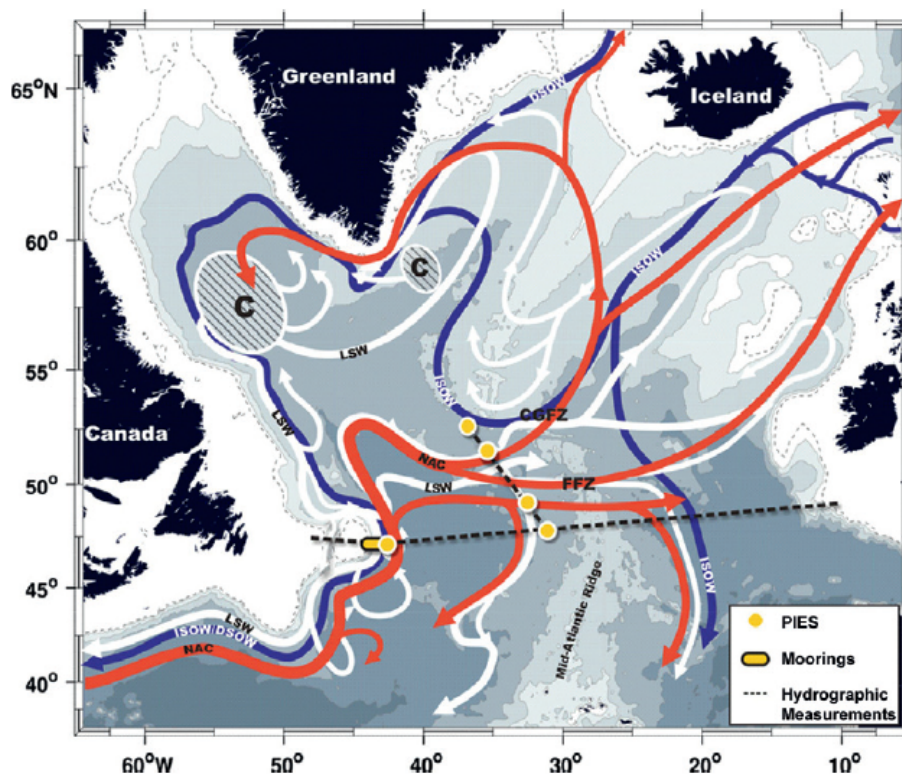
Figure 2.13: The entrance of Northern Atlantic Current from the South-West of Greenland (red) and the pathways of Dense Water Flows around Greenland are shown, where the DSOW and ISOW are depicted in blue and the Labrador Sea Water (LSW) is depcited in white. Source: Rhine et al. 2011 [82]

The ISOW outflows predominantly through the Faroe-Bank Channel (Figure 2.14) while a small fraction exits across the Iceland-Faroe Ridge (Hansen and Osterhus, 2000 [66] and Hansen and Osterhus, 2007 [67]). The combined overflows from DSOW and ISOW is estimated to be ~ 6 Sv (Ross, 1984 [68]; Girton et al., 2001 [69]; and Macrander et al., 2005 [70]; Jochumsen et al., 2012 [71]) (1 Sverdrup = 1 million cubic meters/second). The DSOW is the dominant overflow with roughly 3 Sv of transport across the Denmark Strait. The Faroe Bank Channel, the predominant overflow channel of the ISOW allows a transport of 2.2 Sv (Hansen and Osterhus, 2007 [67]) whereas the Iceland-Faroe Ridge contributes to a relatively smaller 1 Sv transport (Hansen and Osterhus, 2000 [66]).

Figure 2.14: The location of the Faroe Bank Channel in the Greenland-Scotland Ridge. One of the few gaps present in the Ridge is the Faroe Bank Channel. The Ridge also acts as an impediment towards the transport of deep water and stretches from East Greenland-Iceland-Faroe Islands and across up to Scotland. Source: E. Paul Oberlander, Woods Hole Oceanographic Institution [83].

Upon overflowing their respective sills, these get surrounded by rarer water masses allowing them to sink to the bottom. Entrainment of ambient water during the descent doubles the transport (Dickson and Brown, 1994 [72] and Mauritzen et al.,2005 [73]). These current pathways are driven by the bathymetry. The ISOW flows predominantly through the Charlie-Gibbs Fracture Zone (Saunders, 1994 [74]) along its westward journey and a relatively smaller proportion flows through the gaps in the Reykjanes Ridge (Bower et al.,2002 [75]) [Provide Figure]. There occurs periods when the Gibbs Fracture Zone is occupied by the presence of a strong NAC which blocks the dominant westward pathway of the ISOW (Schott et al.,1999 [76]). During such a period, the whole column of water predominantly flows east-wards, however, there is a part of the ISOW which remains in the East Atlantic and

turns southwards following the mid-Atlantic Ridge (Fleischmann et al.,2001 [77]). South of the Denmark Strait and between the Reykjanes Ridge and South-Eastern Greenland lies the Irminger Sea (Figure 2.11), an important region of the Northern Atlantic. There is a formation of a sharp front as the DSOW mixes with the warm STWs. This front has a narrow and strong auxiliary current (known as the East Greenland/Irminger Current) which provides the pathway for freshwater and the Arctic-origin water (of intermediate density) transport to the North Atlantic. Also, over here in the Irminger Sea, the ISOW and the DSOW join and continue their journey southwards as the Deep Western Boundary Currents (DWBC) (Figure 10.8). These two currents are separable on the basis of their tracer properties in the North Atlantic but are usually denoted as the Lower North Atlantic Deep Water (LNADW) characterized by high salinity and oxygen levels.

2.3.4   West Greenland Current:

The East Greenland Current rounds off at the Cape Farewell Section (CFS) and extends northward following the western Greenland coastline. At around 66 °N, it bifurcates towards the west where it gets entrained with the southward flowing Baffin Current (BC) (Figure 2.9) close to the Eastern Canadian coastline. This current is responsible for the transport of water masses from the Arctic Ocean as it leaves the area from the Canadian Arctic Archipelago outflow region. Following the southern pathway along the Eastern Canadian coastline, it merges with the Labrador Current, which ultimately meets the NAC (Figure 2.13) at around 45 °N.

Near the CFS, the waters remain relatively still. As a contrast, the Labrador Current water lying towards the south, is dragged from east to north-east by the NAC (Figure 2.13). As a result, it gradually mixes with the IC in the Irminger Sea and returns back to the region lying south of CFS. It can be inferred that the system of currents near the CFS resembles a great cyclonic gyre having comparitively smaller velocities.

Two major current components are found to be predominant along the banks of Western Greenland. The West Greenland Current (WGC) (extending from the EGC) component is found to be closest to the coast and is responsible for the northward transport of PWs along the Western Greenland coastline. This current receives a substantial amount of freshwater as a result of run-off from the numerous fjordic systems, resulting in the dilution/freshening as it moves northward. The second component is found further to the west lying below the PWs. The origins of this current component can be traced to the Irminger Sea and the water mass signatures relate well with the NAC. The warm and saline water mass signatures are traceable all along Western Greenland beginning from CFS.

Recent studies (Pickart et al., 2001 [84]) have shown that there is a substantial difference in the current components between the Eastern and Western Greenland continental margins. Towards the east, the currents are found to be confined to the shelf break. Contrastingly, the currents to the west extend further offshore over the deep basin (Figure 2.15).
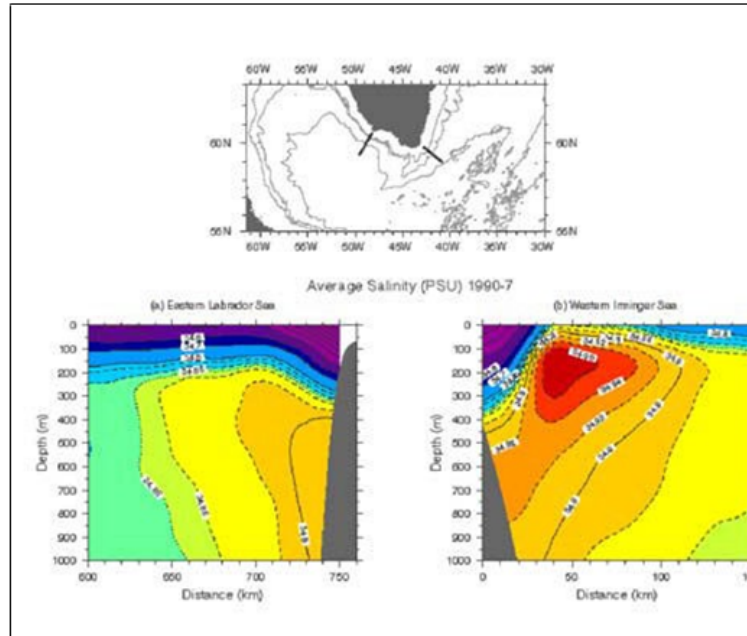
Figure 2.15: The mean upper layer salinity near Cape Desolation Section, Eastern Labrador Sea (Left) and Cape Farewell Section, Western Irminger Sea (Right) for the period 1990-1997 are shown. Source: Pickart et al.,2001 [84].

The steep continental slope towards the western margin leads to the baroclinic instability of the Irminger Current. This results in the generation of a localized high eddy variability source. These fluctuations arising in the IC component has been analyzed through the analysis of spaceborn data (Topex-Poseidon altimeters) along with in-situ data from subsurface drifters and surface floats (Prater, 2000 [85], Fratantoni, 1999 [86], Lavander,2000 [87], Cuny et al.,2001 [88]).

With regards to the properties of flow tracers along Western Greenland, four broad categories of water masses have been characterized in the upper 1000 meters (Buch, 1990/2000 [89]). The Polar Waters (PWs), Irminger Waters (IWs), Irminger Mode Waters (IMWs) and Northwest Atlantic Mode Waters (NAMWs). The PWs are usually cold (below 1 °C) and fresh (below 34.4 psu), however, during the summer months, the temperatures have seen to go up to 3-5°C. The IWs are warm (around 4.5°C) and saline (above 34.95 psu) waters originating from the IC. The IWs are only occasionally traced off of Western Greenland and are found predominantly in the southernmost part (of Western Greenland). The IMWs are the IWs that get mixed with the water masses from the surroundings as it continues northward towards Southwest Greenland. Their tracer properties are comparable to that of the IWs, however, they are relatively cold (4°C) and fresh (34.85-34.95 psu) as compared to

the IWs. The NAMWs are colder (2°C) and fresher (34.5-34.85 psu) compared to the IWs and IMWs, however, temperatures have been observed to go over 5°C during the late autumn months. Both the IMWs and NAMWs are found year round off of the Western Greenland margin.

3

Methodology

3.1 Study Region

Towards analysing the decadal variability in the ocean heat forcing around Greenland, we select 3 prominent locations where the tidewater glaciers terminate in deep (200-750 meters) sea. Two of our study locations are located on the Eastern Margin and one towards the West. In this section, we introduce our study locations and elucidate the motivation behind our selection.

Helheim Glacier:

Helheim Glacier (66.38 °N, 38.8 °W) lies towards South-East Greenland and is one of the largest outlet glaciers of the GrIS [Glacier Research [90]]. Located at the head of the Sermilik fjord and a further 100 km away from the open ocean, the terminus of the Helheim Glacier is submerged in 750 meters of water (Figure 3.1).
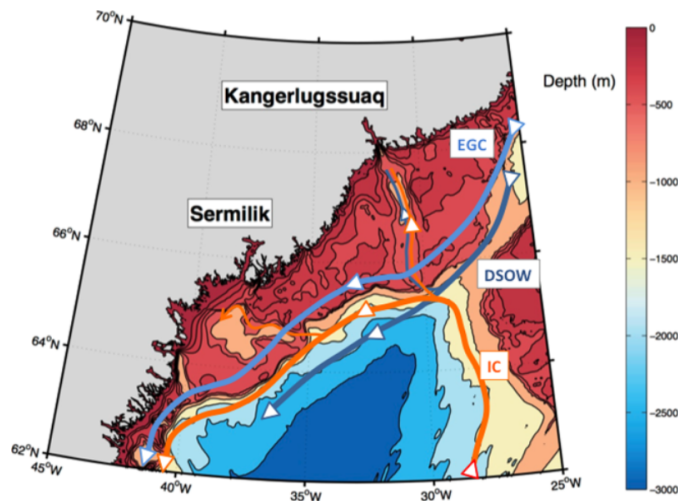
Figure 3.1: Location of the Helheim Glacier in the Sermilik Fjord and the Kangerlussuaq Glacier in the Kangerlussuaq Fjord, Eastern Greenland. The bathymetry is obtained from ETOPO1. Depth contours are represented with 100 meter spacing up to 500 m and thereafter with 500 meter spacing. The arrows are indicative of the current pathways of East Greenland Current (EGC), Irminger Current (IC) and the Denmark Strait Overflow Waters (DSOW). Source: Mark E. Inall et al., 2013 [95]

From 2002 to 2006, the glacier went through a series of rapid changes which included a retreat of the terminus of the glacier by almost 8 km (Figure 2.8). During this period, there was an observed thinning of around 200 meters and also a near-doubling of flow velocity. Studies (Sutherland and Straneo, 2012 [58]), have shown that the AW heat transport from the shelf to the terminus is around 0.029 TW. This makes Helheim Glacier an important location for studying submarine melting.

Kangerlussuaq Glacier:

The Kangerlussuaq Glacier is the largest outlet glacier on the east coast of Greenland (Figure 3.1) (Kangerlussuaq Glacier, UNEP [91]). Between 2000 and 2005, the glacier doubled its flow rate, increasing from 16 m/day in 2000 to 33 m/day in 2005 [Rignot and Kanagaratnam, 2006 [92]]. However, these rates were seen to reduce to 22 m/day in 2010 [Bevan et al., 2012 [93]]. On the contrary, the flow rates at Helheim shows less variability and is found to be somewhat lower in magnitude [Seale et al., 2011 [94]]. A recent study (Mark E. Inall et al.,2013 [95]) quantified the delivery of heat by the AW to the Kangerlussuaq Fjord during September 2010. The results showed the ocean heat flux was 0.26 TW, an order of magnitude greater than the observed value in the Sermilik Fjord where the Helheim Glacier terminates. This is equivalent to melt rates of 10 m/day (30-60% of the flow velocity). This makes the observed submarine melting at Kangerlussuaq Glacier highly significant. Furthermore, a great volume of ice was melted by the warm Polar Surface Waters that were present inside the fjord. The author highlighted that the two well documented retreat events of 2004 (May) and 2010 (November) were preceded by the presence of anomalously warm surface waters within the fjord.

During this period of rapid retreat, observations from mid 1990 - 2005 [Seale et al.,2011 [94]], have shown that the glaciers located further north of the Denmark Strait (above 69°N) have not been accelerating rapidly as the South-Eastern ones. This has been attributed to the absence of AWs from the shelf at such latitudes. Therefore, we do not analyze any locations lying North of the Denmark Strait.

Jakobshavn Glacier:

The Jakobshavn Glacier (69.16 °N, 49.83 °W) is one of Greenland's fastest accelerating glaciers (Figure 3.2), with annually averaged observed terminus speeds of 46 m/day (Joughin et al.,2014 [96]), as observed during summertime measurement campaigns in 2012 and 2013, with greater summertime speeds. While drawing comparisons with the previous summer records, the speedup was found to be 30-50 % larger. The authors documented that the mean annual velocity was three times greater than the observed values in mid 1990s whereas the summertime peak was greater by more than a factor of four.
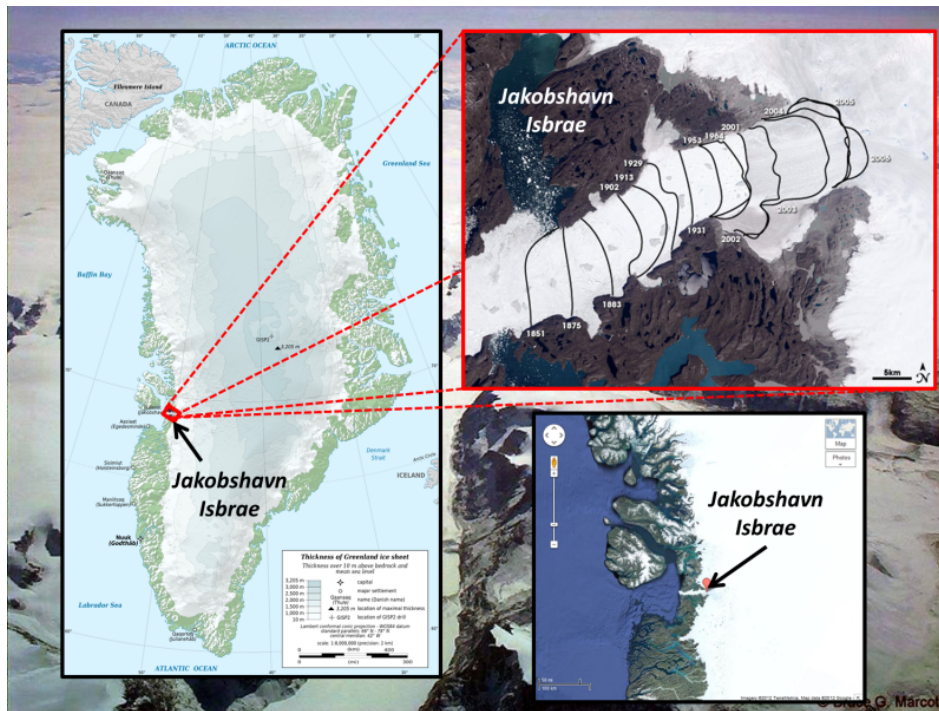
Figure 3.2: Landsat image of Jakobshavn Isbræ courtesy of NASA Earth Observatory. The glaciers calving front position corresponding to the relevant years since 1851 has been shown using black lines. Source: NASA Earth Observatory [97]

There has been a significant variation between 1992 and 2003 (Figure 3.2) in the measured speed of flow of the Jakobshavn Glacier which ranges from $\sim$ 5700 m/yr - 12600 m/yr (Joughin et al., 2004 [98]). This near-doubling of the glacier flow has been shown to cause an increase in the rate of rise in sea level by $\sim$ 0.06 mm/yr, which accounts for $\sim$4% of the rate of rise in sea level in the 20th century (Krishna Ramanujan, NASA, 2004 [99]). From 1850-1964 (Figure 3.2), the glacier retreated by $\sim$ 30 km, followed by a stationary period of 35 years (Pelto et al., 1989 [100]). A rapid acceleration coupled with a dynamic thinning began after 1997 where the glacier reached a terminus velocity of 34 m/day (Figure 3.2). The rates of thinning were observed to be around 15 m/year as it retreated by 5 kms in 6 years (Joughin et al., 2004 [98]; Joughin et al.,2008 [41]).

An increase in the temperature of the AWs (originating from the Irminger Sea) that flow into the West Greenland Current has led to the increase in temperatures around Western Greenland at an observed rate of $\sim$0.2°C/decade [Zweng and Munchow, 2006 [52]]. In 1998, a rapid increase in the AW temperatures across Western Greenland was found to be coincident with the acceleration of Jakobshavn Isbræ [Holland et al., 2008 [8]], and therefore, for a better prediction of the future evolution of the Jakobshavn glacier and the GrIS, a scrupulous understanding of the AW properties around Western Greenland (and close to the glacier in particular) is necessary.

3.2   Setup of General Circulation Models:

This section is divided into three sub-parts. The first part of this section provides a brief introduction to the two General Circulation Models (GCMs), which serve as a tool for our study. The output from the two models will be utilised to answer the proposed research questions (Refer: Subsection 1.4). To that extent, we use output from three different climate simulations, each differing from other in terms of the prescribed climate forcing. The classification of the three different simulations (Pre-Industrial, Historical and RCP 8.5) is done in the second part of this section. Lastly, we provide the grid details specific to each of our study locations, and the time period corresponding to each of the three different simulations, for both the models.

3.2.1   Introduction to General Circulation Models:

HADGEM2-ES Model:

The HADGEM2-ES model is a fully coupled Atmosphere-Ocean General Circulation Model (AOGCM). With 38 levels in the vertical, the atmospheric component has a horizontal resolution of 1.875° (longitude) x 1.25° (latitude), and extends up to 39 km in the vertical (height). The oceanic component has a resolution of 1°x1° (which increases at the equator to 1/3°). There are a total of 40 levels in the vertical reaching depths of 5200 meters. The interval/spacing with respect to height/depth between the levels are not consistent. A general grid structure of the HADGEM2-ES model has been shown below:

Axis	**Grid Points**	**Start**	**End**
Latitude	216	90°S	90°N
Longitude	360	0°E	1°W
Depth	40	5 m	5327.5 m

Table 3.1: HADGEM2-ES model grid structure

GISS-E2-R:

The GISS-E2-R model is the ModelE2 atmospheric general circulation model (AGCM) coupled with the Russel Ocean General Circulation Model (OGCM). The E2-AGCM has a resolution of 2.5° x 2° in longitude and latitude respectively, with 40 layers in the vertical. The E2-AGCM has three different physics-versions, based on how they treat the composition of the atmosphere and the indirect effect of aerosols. They have been categorised on the CMIP5 archive as 'p1', 'p2' and 'p3', referring to the physics version 1,2 and 3 respectively. For our study, we use the first physics version (p1) of the E2-AGCM, which is classified as the 'NINT' version, with a non-interactive atmospheric composition. Within every AGCM grid, four OGCM grids are nested in the Russell OGCM. It has a resolution of 1.25° x 1° in longitude and latitude respectively, with 32 layers in the vertical, which extends to a depth of 4990

meters. Mass conservation in the Russell OGCM allows the excess water added as runoff and precipitation to be conserved before it is cycled to the atmosphere as a result of physical processes such as sublimation or evaporation. This ensures the conservation of salt as well in the model.

Axis	Grid Points	Start	End
Latitude	180	89.5°S	89.5°N
Longitude	288	0.625°E	0.625°W
Depth	32	6 m	4887 m

Table 3.2: GISS-E2-R model grid structure

3.2.2   Classification of climate simulations

The General Circulation Models (GCMs) require time to approach their own climatology after starting from prescribed initial and boundary Conditions. This is referred to as the spin-up period of the model; during which the model tries to attain stabilisation. After spin up, the models can be forced in different ways. Each climate simulation, therefore, pertains to a specified forcing criteria. This part of the section briefly explains the classification of the three different climate simulations used in our study.

HADGEM2-ES Model:

To understand the natural variability within the climate system, we make use of the control run from the HADGEM2-ES model, which follows from the CMIP5 guidelines (Refer to the URL for the CMIP5 guidelines at [101]) for Initial and Boundary conditions for the baseline simulations. To that extent, the run initiates at A.D. 1860, after the components are spun up to 1860 climate state (pre-industrial climate state), with a prescribed non-evolving CO_2 forcing as the boundary conditions. In other words, the CO_2 concentration levels are held constant at pre-industrial values of 286.3 ppm. As there are no prescribed changes in the external forcings that influence the climate, they provide the tool for evaluating the internal noise within the climate system.

At this time, the climate system is assumed to reach its equilibrium position. However, several components of this system equilibrate on much longer timescales resulting in an imbalance in the energy budget, and an associated climate drift. Among them are the physical parameters involving oceans, and more specifically, the deep ocean circulation, a phenomenon operating on millennia level timescales.

The spin-up state of the HADGEM2-ES model is so chosen that the climate drifts remain negligible (Collins et al.,2011 [102]) over the standard course of a simulation (∼300 years). It is, however, a general practice, to account for the climate drift, as models do not fully equilibrate during the spin up period. In the case of physical oceanic properties such as the sea water potential temperature (ThetaO), the drift is

usually manifested as a warming/cooling of the ocean resulting from the net radiative top of atmosphere (TOA) energy imbalance. To that extent, a linear regression over the Pre-Industrial period is calculated and subtracted from the Pre-Industrial, Historical and RCP 8.5 simulations.

The pre-industrial run is followed by a historical simulation, which again follows from the CMIP5 protocol (CMIP5 guidelines [101]). In the HADGEM2-ES model, this is defined for a period from 1860-2005, initialised after the PI-Control spin-up. The external climate forcings for this period are obtained from the historical record of both anthropogenic (GHGs, aerosols) and natural forcings (solar and volcanic). The CO_2 concentrations that are used in the Historical simulation were obtained from the global mean data, NOAA (NOAA global mean CO_2 data [103]); measurements from the observatory at Mauna Loa (Keeling et al.,2009 [104]) and also the Law Dome ice core.

The RCP 8.5 (Representative Concentration Pathway 8.5) is one of the 4 future climate simulations, which extends from the 2005 model state. Therefore, it utilises the state of the model at the end of the Historical Simulation as its initial condition. The RCP 8.5 scenario is representative of high GHG concentrations and is characterized, over the course of the simulation, through increasing GHG emissions, with radiative forcing reaching ∼8.5 W/m² towards the end of the 21st century.

From the initial state, the recommended concentrations for the 21st century is calculated using the harmonized data provided by the IIASA (the IAMC responsible for RCP 8.5). This includes pathways of emissions that begin from 2000 for several GHGs, along with well-mixed GHG emissions from 2005-2100. The time series is extended beyond 2100, in such a manner that the CO_2 concentrations under the RCP 8.5 scenario become stable (∼2000 ppm by A.D. 2250). Both the Historical and the RCP 8.5 simulation require the boundary conditions (external climate forcing factors) to vary with time.

GISS-E2-R Model:

The temperature and salinity distribution derived from Levitus climatology [Levitus and Boyer, 1994; Levitus et al., 1994] is used for initialising the ocean from rest. The composition of the atmosphere and the solar irradiance are kept constant at pre-industrial levels, (i.e., at the values synonymous to A.D. 1850) and the model is pushed towards an equilibrium state.

Measurements from Ice-Cores (Schmidt et al 2011) are used to prescribe the GHG concentrations. Before commencing the pre-industrial (control) run, the model is allowed to run for ∼500 years, which is roughly a few decades more than what is required to bring the upper ocean in an equilibrium with the atmosphere. However, the deep ocean does not attain a complete balance in this duration, as it usually needs ∼(a few) 1000 years. The net TOA imbalance is small (Forster et al 2013), however, a gradual climate drift persists through the course of the run, which needs

to be accounted for, as in the case of the HADGEM2-ES model.

The control run extends for a period of 531 years. The first 81 years from this period are used to initialise the Historical simulation. The last 451 years includes the period extending from A.D. 1850 - A.D. 2300, which are used to draw comparisons with the perturbed historical and RCP 8.5 simulations.

3.2.3   Grid detail of study regions

In this section, we provide the grid details corresponding to each of our study locations for both the models in Table 3.5 and 3.6. The time-period corresponding to each of the three simulations for the HADGEM2-ES and the GISS-E2-R model is provided in Tables 3.3 and 3.4.

HADGEM2-ES	
Simulation Name	**Period**
PI-Control	90 years
Historical	A.D. 1909 - A.D. 2005
RCP 8.5	A.D. 2005 - A.D. 2095

Table 3.3: HADGEM2-ES Model: Time Period for each of the three simulations

GISS-E2-R	
Simulation Name	**Period**
PI-Control	90 years
Historical	A.D. 1909 - A.D. 2005
RCP 8.5	A.D. 2005 - A.D. 2095

Table 3.4: GISS-E2-R Model: Time Period for each of the three simulations

Helheim Glacier: HADGEM2-ES	
Variable Name	Values
Section Span	38°W-27°W, 65°N
Shelf Span	38°W-35°W, 65°N
Offshore Span	35°W-27°W, 65°N
Kangerlussuaq Glacier: HADGEM2-ES	
Variable Name	Values
Section Span	31°W-18°W, 68°N
Shelf Span	31°W-27°W, 68°N
Offshore Span	27°W-18°W, 68°N
Jakobshavn Glacier: HADGEM2-ES	
Variable Name	Values
Section Span	54°W-64°W, 69°N
Shelf Span	54°W-58°W, 69°N
Offshore Span	58°W-64°W, 69°N

Table 3.5: The grid details corresponding to the HADGEM2-ES model have been presented for each of the study locations. These locations can also be viewed in the Study Area Map (3.3).

Helheim Glacier: GISS-E2-R	
Variable Name	Values
Section Span	38°W-27°W, 65.5°N
Shelf Span	38°W-35°W, 65.5°N
Offshore Span	35°W-27°W, 65.5°N
Kangerlussuaq Glacier: GISS-E2-R	
Variable Name	Values
Section Span	32°W-18°W, 67.5°N
Shelf Span	32°W-27°W, 67.5°N
Offshore Span	27°W-18°W, 67.5°N
Jakobshavn Glacier: GISS-E2-R	
Variable Name	Values
Section Span	52°W-64°W, 68.5°N
Shelf Span	52°W-58°W, 68.5°N
Offshore Span	58°W-64°W, 68.5°N

Table 3.6: The grid details corresponding to the GISS-E2-R model have been presented for each of the study locations. The longitudes have been rounded off to the nearest integer for convenience. These locations can also be viewed in the Study Area Map (Figure 3.3).
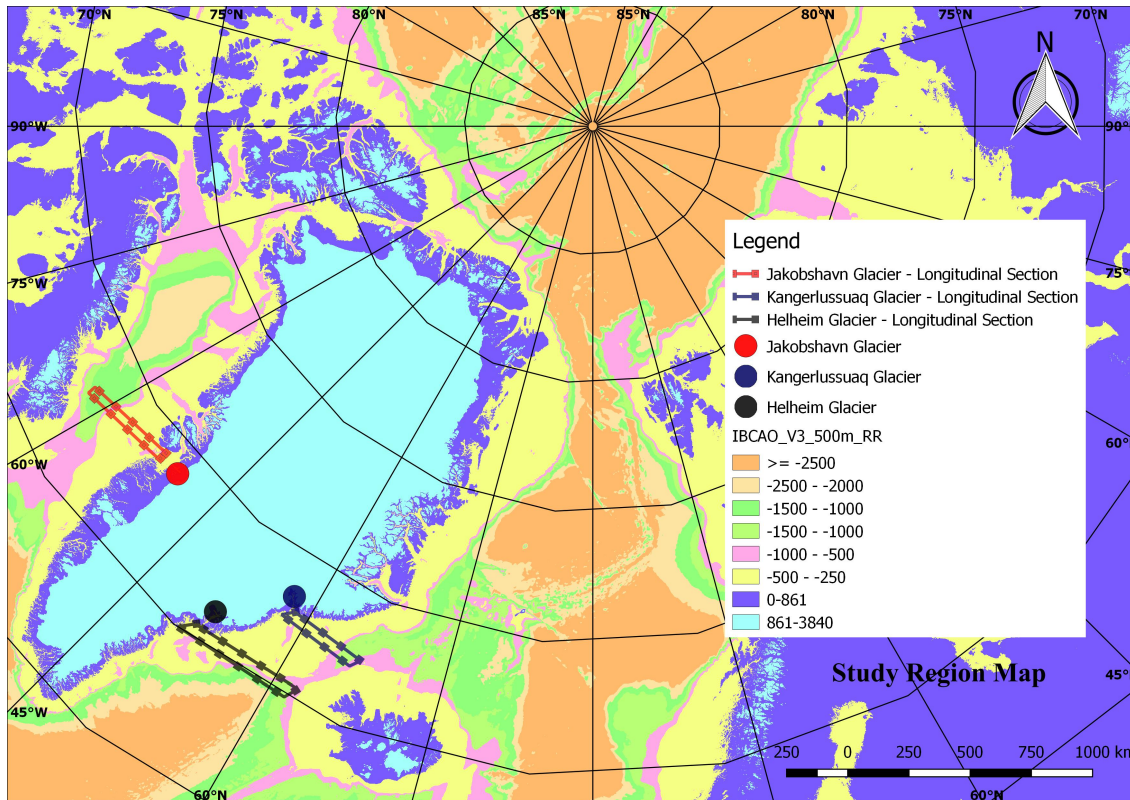
Figure 3.3: Study Region Map: The three prominent tidewater glacier locations used in our study have been highlighted using coloured circles. The longitudinal section that forms the basis of our analysis framework has been represented using rectangular boxes. The bathymetry data has been obtained from IBCAO Version 3 (IBCAO_V3_500m_RR), which has an improved 500 meter radiometric resolution. The colorbar has been provided to highlight the bathymetry.

3.3 Model Evaluation

In order to answer our research questions proposed in subsection 1.4, we use the modelled temperature and salinity fields as flow tracers (a fluid property that can be used to track its flow), from both the HADGEM2-ES and GISS-E2-R model. These modelled parameters are first evaluated against observational datasets.

In order to draw direct comparisons, high Resolution CTD datasets, obtained from hydrographic sections around our study locations are regridded to the respective modelled grids. These datasets correspond to a period from 1950-2005. The winter-time Arctic sea-ice cover makes data acquisition a challenging task, and therefore, these observations span from April-November. The premise of our model evaluation takes into consideration these parameters. To that extent, we use the output from the last 56 years of the Historical Simulation (1950-2005). Modelled means of the tracers do not take into account the months of January, February, March and December.

In this section, we first explain **A)** the data profile, followed by **B)** the working principle of a CTD profiler and how it obtains the variables of interest. This is followed by **C)** the formulation of our regridding technique.

A) CTD Data Profile:

We provide information about the data source, and the sampling characteristics of the data corresponding to each of our study locations.

The high resolution CTD datasets are obtained from National Oceanic and Atmospheric Administration's (NOAA) World Ocean Database 2013 (WOD13). The data is acquired during hydrographic cruises and corresponds to several days-weeks of a particular month. As stated before, owing to logistical constraints, the dataset is only acquired from April-November. To keep the observational data consistent with our GCMs, we compute the monthly mean from the cruise data corresponding to that particular month. These are then used to construct the annual means from which we later compute the 56 year climatological fields of Temperature and Salinity (T-S) from 1950-2005. Furthermore, the section span is consistent with the modelled sections (Refer Tables 3.5 and 3.6). Table 3.7 provides details corresponding to each of our study locations.

Location	Cast Count	Grid Details	Resolution (Y*Z)
Helheim	415	38-27°W, 65°N	410*3706
Kangerlussuaq	479	31-18°W, 68°N	474*1593
Jakobshavn	138	52-64°W, 69°N	137*1257

Table 3.7: CTD Data Profile corresponding to each of our study location. Y and Z denotes the Longitude and Depth respectively.

B) Setup of a CTD Profiler:

A CTD (Conductivity, Temperature and Depth) is an oceanographic instrument used to measure the conductivity, temperature and pressure profile of the column of water. A vertical profile is created as the CTD is lowered into the water column. Both top-down and bottom-up profiles can be created using the instrument. The pressure measurements are used to calculate the depth. The instrument measures changes in the conductivity and temperature of the column of water with respect to the depth (pressure), which is later used to obtain the salinity of the column. The measurement of the variable fields and the subsequent calculation of other parameters of interest has been described below:

Variable Fields:

i) Temperature: The potential temperature (θ) of a fluid parcel is the temperature that it would have if it were displaced adiabatically to a standard reference pressure

(usually 1000 mbar). Mathematically, if a parcel having tracer properties of S_0, T_0 and P_0, was moved adiabatically to a reference pressure P_R, then the potential temperature of the parcel is expressed as:

$$\theta(S_0, T_0, P_0, P_R) = T_0 + \int_{P_0}^{P_R} \Gamma(S_0, \vartheta(S_0, T_0, P_0, P), P)dP) \tag{3.1}$$

Where; Γ is referred to as the adiabatic lapse rate, which is the temperature change corresponding to per unit pressure change, when a parcel gets displaced adiabatically. Mathematically, this can be expressed as:

$$\Gamma = (\frac{\partial T}{\partial P})_{\text{adiabatic}} \tag{3.2}$$

$$\Gamma = -\frac{T}{\rho^2 C_p}(\frac{\partial \rho}{\partial T})_{P,S} = \frac{\alpha_T T}{\rho C_p} \tag{3.3}$$

Where; α_T denotes the thermal expansion coefficient, expressed as:

$$\alpha_T = -\frac{1}{\rho}(\frac{\partial \rho}{\partial T})_{P,S} \tag{3.4}$$

Where; T refers to the absolute temperature (measured in °K), and,
C_p is the reference specific heat capacity of sea-water taken as 3990 J/Kg/K.

In a CTD profiler, a thermistor is used to measure/sense the temperature. The device relies on measuring the change in resistance offered by a piece of metal wire, when a current is passed through it. As the relationship between the resistance and the temperature is non-linear, conversion coefficients are used to describe the logarithmic relationship. These coefficients are referred to as the Steinhart-Hart coefficients (Refer to the Steinhart-Hart equation 3.5).

$$\frac{1}{T} = a + b\ln\frac{fo}{f} + c\ln^2\frac{fo}{f} + d\ln^3\frac{fo}{f} - 273.15 \tag{3.5}$$

where;
T is the temperature in Kelvin;
a,**b**,**c** and **d** are referred to as the Steinhart-Hart coefficients, which vary, based on the thermistor model and the desired range of temperature.
f is the observed sensor frequency. The term **fo/f** is the Resistance (**R**) offered at Temperature **T**.

ii) Pressure: A CTD uses a pressure gauge for measuring pressure. The working principle behind a pressure gauge relies on measuring the applied external pressure which causes a small fluid tube to compress (or expand). As the atmospheric pressure varies, a sensor relying on the gauge pressure will be subjected to a built-in error. Therefore, absolute pressure (relative to vacuum) is used instead of differential pressure. The pressure in the ocean is correlated to the depth, which implies that the depth (at a pressure reading) can be determined by the pressure that is exerted on the gauge. Generally, pressure is measured in decibar(dbar), and 1dbar

roughly translates to a depth of 1 m. The calculation of depth from pressure is done using the hydrostatic approximation assuming that there is no fluid motion (Equation 3.6)

$$P(dbars) = \int_0^z \rho(z)g dz \tag{3.6}$$

Where;
ρ is the density of the ocean (1027 kg/m^3)
g is the acceleration due to gravity (9.8 m/s^2).
Using these typical values, we obtain a proportionality constant of 1.0065 dbar/m. This roughly translates to a 2-3% error if the pressure values (dbar) are used as depths (m).

The integral of the vertical equation of motion, from the top of the atmosphere (∞) to a given depth level (-z), for an ocean in static equilibrium, can be used to obtain the pressure at the given depth (-z), as observed by the CTD (Equation 3.7).

$$P(-z) = \int_\infty^{-z} \rho(z)g dz \tag{3.7}$$

The pressure signal at the bottom (Equation 3.8) is a contribution of several different components. These include:

- The contribution of the atmospheric pressure (P_{atm}), which is the vertical integral from TOA (z=∞) to the surface of the sea (z=η).
- The sea surface height variability (mean sea level (m.s.l.) deviation) characterized by waves whose time varying elevation is described by η. This pressure arising from the surface wave is obtained by a vertical integral from the surface of the sea (z=η) to the m.s.l. (z=0).
- The next component is the mean hydrostatic pressure, which is the vertical integral from the m.s.l. (z=0) to the given depth (z=-z).
- The final component depends on the deviation in mean density (given by ρ_{avg}). The term ρ'(z) describes how the changes in internal density influences the pressure as observed by the bottom pressure sensor.

$$P(-z) = P_{\text{atm}} + \rho_0 g \eta + \rho_{\text{avg}} g h + \int_0^{-z} \rho'(z)g dz \tag{3.8}$$

iii) Conductivity: Theoretically, salinity is defined as the amount of solute (inorganic ions which are less than 0.5 μm) dissolved per kg of seawater. Formally expressed as parts per thousand (ppt), Practical Salinity Unit (PSU) is now used as the standard unit. As both these units are roughly the same, PSU can be considered as a decent approximation for ppt and vice versa. CTD measures the conductivity of sea-water to determine the amount of dissolved inorganic ions. An electric current is made to pass between two plates. The minerals and salts present in the sea water will act as a conductor of electricity when the sampled water is made to pass between these plates. The resistance offered by the water sample is used to determine the ion concentration of the water. Practical Salinity Unit (PSU) is obtained by using the sample temperature (t) and conductivity ratio (C) (Equation 3.9). The conductivity ratio is the ratio of measured to known conductivity.

The known conductivity refers to the conductivity of a particular concentration of dissolved minerals and salts. Typically, this method has a precision of ∼0.001 PSU.

$$S = a_0 + a_1 C^{\frac{1}{2}} + a_2 C + a_3 C^{\frac{3}{2}} + a_4 C^2 + a_5 C^{\frac{5}{2}} + \frac{t-15}{1+k(t-15)} \cdots$$
$$\cdots + b_0 + b_1 C^{\frac{1}{2}} + b_2 C + b_3 C^{\frac{3}{2}} + b_4 C^2 + b_5 C^{\frac{5}{2}} \tag{3.9}$$

Where,
a,**b** and **k** are fitting constants.

Through the course of our study period (1950-2005), different CTD profilers were deployed by various research institutions during their respective cruise. The accuracy and stability of a typical modern day CTD device is provided in the table below (Table 3.8).

Parameter	Initial Accuracy	Typical Stability
Conductivity	± 0.0005 S/m	0.0003 S/m/month
Temperature	± 0.005°C	0.0002°C/month
Pressure	± 2dbar	2dbar/year

Table 3.8: Detailed Specifications of the SBE 19plus V2 profiler.

C) Regridding of High Resolution CTD Data:

The temperature and salinity data extracted from the CTD profilers are then regridded to the model grid (Refer Table 3.1 and 3.2) so as to allow us to draw comparisons with the modelled Temperature and Salinity (T-S) fields.

For regridding our high resolution CTD datasets of Temperature (θ_{obs}), Salinity (S_{obs}) , we make use of an interrogation window (λ). The window is used to sort, group and then interpolate the the observed variable (T-S) fields corresponding to observed longitude (Y_{obs}) and depth (Z_{obs}), to the modelled longitude (Y_{mod}) and depth (Z_{mod}) grid points. For regridding at the desired grid point (Y_{mod} and Z_{mod}) within the window, we use the inverse distance weighting approach. The mathematical formulation of the technique used has been described below:

Window Size:
The size of the window in the direction of Longitude, is determined based on the model resolution across longitude. Therefore, for HADGEM2-ES, the size of the window is 1° (Refer Table 3.1) and for the GISS-E2-R model, the size of the window is 1.25° , (Refer Table 3.2). The longitude component of the window can be expressed as λ_{Y}, where:

$$\lambda_{\mathrm{Y}} = Y \pm \frac{\delta_{\mathrm{Y}}}{2} \tag{3.10}$$

And,

$$\delta_{\mathrm{Y}} = Y_{\mathrm{j+1}} - Y_{\mathrm{j}} \tag{3.11}$$

Where;

$\delta_{\mathrm{Y}}=$ Difference between two successive modelled longitude grid points ($Y_{\mathrm{j+1}}$, Y_{j}).

Along the vertical, the distance between two consecutive modelled depth level is used to determine the window size. As the depth intervals are unequal, different window sizes need to be implemented. The depth component of the window can be expressed as λ_{Z}, where:

$$\lambda_{\mathrm{Z}} = Z_{\mathrm{mod}} \pm \frac{\delta_{\mathrm{Z}}}{2} \tag{3.12}$$

And,

$$\delta_{\mathrm{Z}} = Z_{\mathrm{j+1}} - Z_{\mathrm{j}} \tag{3.13}$$

Where;

δ_{Z} is the vertical distance between two successive modelled depth levels ($Z_{\mathrm{j+1}}$, Z_{j})

Formulation:

Let n be the number of observations that fall within our window. Then, the regridded Temperature ($\hat{\theta}_{\mathrm{d}}$) and Salinity fields ($\hat{S}_{\mathrm{d}}$) corresponding to each modelled depth (Z_{mod}) and longitude (Y_{mod}), is given as:

$$\hat{\theta}_{\mathrm{d}} = \frac{1}{\sum_{i=1}^{n} \frac{1}{d_{\mathrm{R_i}}}} \left(\frac{\theta_{\mathrm{obs_1}(Y_{\mathrm{obs}}, Z_{\mathrm{obs}})}}{d_{\mathrm{R_i}}} + ... + \frac{\theta_{\mathrm{obs_n}(Y_{\mathrm{obs}}, Z_{\mathrm{obs}})}}{d_{\mathrm{R_n}}} \right) \tag{3.14}$$

$$\hat{S}_{\mathrm{d}} = \frac{1}{\sum_{i=1}^{n} \frac{1}{d_{\mathrm{R_i}}}} \left(\frac{S_{\mathrm{obs_1}(Y_{\mathrm{obs}}, Z_{\mathrm{obs}})}}{d_{\mathrm{R_i}}} + ... + \frac{S_{\mathrm{obs_n}(Y_{\mathrm{obs}}, Z_{\mathrm{obs}})}}{d_{\mathrm{R_n}}} \right) \tag{3.15}$$

Where;

θ_{obs} and S_{obs} denote the observed temperature and salinity values within the interrogation window (λ)

d_{R} is the distance between the observation point (θ_{obs},S_{obs}) and the interpolation location ($\hat{\theta}_{\mathrm{d}}$,$\hat{S}_{\mathrm{d}}$). If the observational longitude (Y_{obs}) is the same as modelled longitude (Y_{mod}), the distance d_{R} is simply expressed as the vertical distance (z) between the observation point and the interpolation location. Otherwise, d_{R} can be expressed as:

$$d_{\mathrm{R}} = \sqrt{z^2 + y^2} \tag{3.16}$$

Where;

z and y correspond to the vertical and longitudinal distances between the observation and the interpolation location.

We assume a spherical earth, and therefore, at a particular latitude expressed as ϕ, the length of one degree of longitude is expressed as:

$$\frac{\pi}{180} R_{\mathrm{m}} cos\phi \tag{3.17}$$

Where;

R_{m} is the meridional radius of the earth, taken as 6367.449 kms.

Appendix: Sea-Ice Concentration
Sea-Ice Concentration (SIC) is expressed as the relative amount (percentage) of area occupied by sea-ice within every modelled grid point. On a scale from 0-100 (%), a value of 0 implies a completely sea-ice free grid point and vice-versa. The HADGEM2-ES and GISS-E2-R derived SIC along the Jakobshavn section is used to address the discrepancy between the modelled and observed surface water characteristics. For the Historical Simulation (A.D. 1950-2005), we obtain the annual SIC climatologies from the monthly sampled sea-ice concentration field, which is then used to construct the 56 year climatologies.

3.4 Spatial Variability in the Ocean Heat Forcing

To understand the spatial variability in the Ocean Heat Forcing, we first assess the spatial distribution of ocean currents along our study regions using the Pre-Industrial simulation ($\sim$20 year period). Anomalies in Historical (A.D. 1985-2005) and RCP 8.5 (A.D. 2075-2095) simulation, with respect to the Pre-Industrial simulation, are used to establish the response of the dominant currents towards GHG forcing. Emphasis is given on addressing how and why these responses vary across our study locations.

Part **A** of this section explains the methodology used to construct hydrographic sections of Temperature and Salinity (T-S) from the GCMs.

For a future warming scenario, the salinity anomalies (RCP 8.5 - Pre-Industrial) show a considerable freshening of the surface waters. This is partly driven by the substantial decline in modelled (winter) sea-ice concentration (SIC), which leads to an enhanced (winter) precipitation in the Arctic. For this reason, we make use of the modelled SIC and Precipitation fields for each of the three simulations using methods illustrated in Part **B**.

A) Temperature and Salinity Field:

For each of the three simulations corresponding to both the GCMs (Refer 3.3 and 3.4), a 20 year-period is used. For the Historical and RCP 8.5 simulation, this corresponds to the last 20 years. Annual climatologies are first obtained for each of the three simulations, from the monthly sampled sea-water potential temperature and salinity fields. Then, the 20 year climatologies are computed from the annual climatological fields.

B) Sea-Ice Concentration and Precipitation Cycle:

Sea-Ice Concentration:
We use the modelled SIC field to construct the mean annual SIC cycle for the RCP 8.5 scenario (A.D. 2075-2095) for each of our study regions.

Precipitation:
1 kg of precipitation over 1 m^2 area has 1 mm thickness. Therefore, we first convert the monthly modelled Precipitation , expressed in kg/m^2/s, to mm/month

$$P(mm/month) = P(kg/m^2/s) \times 30 \times 24 \times 60 \times 60 \tag{3.18}$$

This is then used to calculate the mean annual precipitation cycle for the RCP 8.5 simulation, for a period from A.D. 2075 to A.D. 2095, corresponding to each of our study regions.

3.5 Temporal Variability in the Ocean Heat Forcing:

To understand the multi-year/decadal variability in the Ocean Heat Forcing across our study regions, we construct a time series of the Ocean Heat Content Density (expressed in J/m^2), for each of the three climate simulations. The methodology pertaining to the Ocean Heat Content Density calculations from the sea-water potential temperature profile has been explained in part **A)** of this section. Part **B)** explains the spectral analysis methods used to distinguish the long-term (low-frequency) anthropogenic sourced signal from the high-frequency background variability, and to extract the periodicity.

A) Ocean Heat Content Time Series:

The amount of heat stored in the ocean is expressed in Joules, through the Ocean Heat Content (OHC). For our study, the monthly modelled three-dimensional field of sea-water potential temperature is used to create a time series of the areal Ocean Heat Content density (J/m^2) for each of the three simulations. To that extent, the temperature field that corresponds to our study locations are first averaged over the longitudinal/latitudinal sections (Refer Equation 3.19). The resulting (averaged)

temperature profile for our section , is used to obtain the time series of the areal Ocean Heat Content density (Refer Equation 3.20).

$$\bar{\theta}_z = \sum_x \theta_{(x,z)} \ ; \ \bar{\theta}_z = \sum_y \theta_{(y,z)} \tag{3.19}$$

Where ;

For a longitudinal section, $\theta_{x,z}$ is the sea-water potential temperature corresponding to every modelled longitude (x) and depth (z) grid point.

For a latitudinal section, $\theta_{y,z}$ is the sea-water potential temperature corresponding to every modelled longitude (y) and depth (z) grid point.

$\bar{\theta}_z$ is the sea-water potential temperature profile over depth (z), averaged over the entire section.

$$\Phi = \rho C_p \int_{z_1}^{z_2} \bar{\theta}_z dz \tag{3.20}$$

Where ;

ρ is the reference density of sea-water, taken as 1029 kg/m^3

C_p is the reference specific heat capacity of sea-water, taken as 3990 J/Kg/K

Φ is the areal Ocean Heat Content density (J/m^2) between upper (z_1) and lower (z_2) ocean depth levels.

The OHC time-series corresponding to each of our simulation has an associated climate drift (as discussed under subsection 3.2.2) as the models do not fully equilibrate during the spin-up period. The drift arises from the net radiative top of atmosphere (TOA) energy imbalance and usually results in a warming/cooling of the ocean. We follow a general practice, wherein, we compute the linear regression over the Pre-Industrial time-series and subtract it from each of the three simulations.

B) Spectral Analysis of the modelled OHC signal:

Within the domain of our modelled section, the response of the ocean is manifested over different timescales. Over shorter time scales (several weeks-months), the response is driven by active turbulence. These turbulent processes are mostly driven by ocean waves, winds and/or increase in surface density as a result of brine rejection (during sea-ice formation), cooling and surface evaporation, leading to (deep) convection. This causes homogenisation of the ocean up to a certain depth level, known as the mixed layer depth. While the GHGs influence the short-term response, their influence is largely manifested as a very dominant, low frequency, long-term response.

As the Pre-Industrial simulation does not include any evolving forcing, there is considerable high-frequency contributions towards the total energy contained in the OHC signal. The long-term response can be thought of as a low-frequency natural variability in the oceans climate. For the Historical and RCP 8.5 simulations, over shorter time scales, the GHG forcing influences the high-frequency response. Furthermore, an anthropogenic sourced, dominant, low-frequency response is induced. In order to distinguish between climate processes that act over varied timescales in each of our simulation, we use the Complete Ensemble Empirical Mode Decomposition with Adaptive Noise (CEEMDAN) algorithm. The Ensemble Empirical Mode Decomposition (EEMD) forms the basis for CEEMDAN, which in turn, follows from the Ensemble Mode Decomposition (EMD) (Huang et al., 1998 [105]).

The EMD approach is used for the analysis of non-stationary and non-linear properties of a time-series. It is based on the assumption that the time-series (dataset) comprises of intrinsic modes of oscillations. These are identified by the algorithm as the Intrinsic Mode Functions (IMFs), based on the characteristic structural and temporal locality exhibited by the series. It uses information from the extrema of the waves for the input time-series. This is used for the successive extraction of the oscillatory constituents, beginning with high-frequency components, and advancing towards the low frequency components. This allows for a natural separation of the long-term (low-frequency) trend from the non-linear high-frequency oscillation patterns. These Intrinsic Mode Functions, corresponding to each of our simulation, are construed as the basis vectors that characterise the modelled Ocean Heat Content. The CEEMDAN approach operates as a dyadic filter bank (Flandrin et al.,2004 [106]; Wu and Huang,2004 [107]). Each mode can be regarded as a bandpass filter (Flandrin et al.,2004 [106]); where the mean period corresponding to the subsequent mode is (nearly) exactly doubled with respect to the previous mode. There is no certainty that the modelled Ocean Heat Content contain harmonic components, and therefore, Fourier/Wavelet analysis would provide the same context, however, they would be (physically) less meaningful (Chang et al., 1997 [108]). Thus, we argue that CEEMDAN is a more-suited method for our analysis.

Empirical Mode Decomposition:

In an EMD, each IMF so computed, needs to meet two conditions. Firstly, the local mean of the envelope obtained from the extrema of the waves must be 0. Secondly, throughout the analysis of the signal, the zero crossings and the extreme signal should have the same integer value. Let the input of the Ocean Heat Content time-series be represented by OHC(t). Following steps are used for the decomposition of this signal using the EMD:

- The maxima and minima of the waves are obtained for the OHC(t). A cubic spline interpolation is used to separately connect these points to create the upper (δ^+) and lower (δ^-) envelopes.

- The local mean of the new formed envelope (δ) is computed through:

$$\bar{\delta}(t) = (\delta^+ + \delta^-)/2 \tag{3.21}$$

- If $\bar{\delta}(t) \sim 0$, then the zero local mean IMF ($\bar{I}1(t)$) is computed by subtracting the local mean of the envelope ($\bar{\delta}(t)$) from the input signal OHC(t).

$$\bar{I}1(t) = OHC(t) - \bar{\delta}(t) \tag{3.22}$$

- If the aforementioned criteria is not met, the preceding steps are repeated until $\bar{\delta}(t) \sim 0$.
- The first IMF obtained ($\bar{I}1(t)$) for the input time series OHC(t) from this procedure corresponds to the smallest temporal scale of OHC(t).
- Subtraction of the first mode from the input time series OHC(t), yields the residue, denoted by $\gamma 1(t)$.

$$\gamma 1(t) = OHC(t) - \bar{I}1(t) \tag{3.23}$$

- The components of the input time series OHC(t) that correspond to larger temporal scales are contained in the residue $\gamma 1(t)$, which now corresponds to the new input time series.
- To obtain the subsequent components, the residue is resifted. This sifting procedure is carried on, generating the IMFs and the following residues, until no further IMFs can be extracted. The resulting final residue $\gamma n(t)$, therefore, is a constant, monotonic function (Refer Flandrin et al,2004 [106]).

$$\gamma 2(t) = \gamma 1(t) - \bar{I}2(t) \quad ; \gamma 3(t) = \gamma 2(t) - \bar{I}3(t) \quad ; \gamma n(t) = \gamma_{n-1}(t) - \bar{I}_n(t) \tag{3.24}$$

- The input time series OHC(t), post the EMD, is expressed as

$$OHC(t) = \sum_{i=1}^{n} Ii(t) + \gamma n(t) \tag{3.25}$$

Where;
n corresponds to the total number of generated IMFs.

It becomes clear that the EMD does not use any a-priori basis function. The piecewise fit ensures that the process is adaptive and temporally local. However, there is a problem with regards to mode-mixing. The Ensemble Empirical Mode Decomposition (EEMD) is used to resolve the problem.

Ensemble Empirical Mode Decomposition:

The IMFs in the Ensemble Empirical Mode Decompostion (EEMD) are obtained as the ensemble mean of the IMFs obtained from EMD over an ensemble of trials OHC^i, where (i=1,2,3,...,K). The process can be expressed as follows:
- Different white noise realisations (ε^i) are generated having a fixed amplitude β.

- The different realisations of the generated white noise is added to the input signal OHC, to generate an ensemble of trials OHC^i, where, i=1,2,3,...,K.

$$OHC^i = OHC + \beta \varepsilon^i \qquad (3.26)$$

  Where;
  ε^i(i=1,2,3,..,K) is a Gaussian white noise having zero-mean and unit variance. β defines the predefined and fixed amplitude of the white noise.
- The EMD is used for the decomposition of each of the individual trials OHC^i, where i=1,2,3,..,K, resulting in the generation of j=1,2,3...,J number of modes (I_j^i), corresponding to each individual trial (i).
- The jth mode of OHC, denoted by $\bar{I}_j$, is given as:

$$\bar{I}_j = \frac{1}{K} \sum_{i=1}^{K} I_j^i \qquad (3.27)$$

The EEMD approach tackles the mode mixing problem that occurs in EMD, however, if the ensemble is not big, it does not alleviate all of the noise from the IMFs.

Complete Ensemble Empirical Mode Decomposition With Adaptive Noise:

As each individual trial undergoes an independent decomposition in an EEMD, a set of different residues are generated, with each set corresponding to a different realisation.

$$\gamma_j^i = \gamma_{j\text{-}1}^i - I_j^i \quad (\gamma_0^1 = OHCi) \qquad (3.28)$$

The Complete Ensemble Empirical Mode Decomposition With Adaptive Noise (CEEMDAN) approach takes the first EEMD mode (denoted as $\tilde{I}_1$) to generate the first residue (γ_1).

$$\gamma_1 = OHC - \tilde{I}_1 \qquad (3.29)$$

An ensemble of trial is generated, using the single first residue and different realisations of a white noise, over which, the first EMD mode is calculated. The $\tilde{I}_2$ is obtained through averaging.

The **CEEMDAN** algorithm adopted for our study is explained below in detail:

- Different white noise realisations (ε^i) are generated having an amplitude β_0. An ensemble of trials of the input signal are generated by adding the white noise to the input signal (OHC).

$$OHC^i = OHC + \beta_0 \varepsilon^i \qquad (3.30)$$

  Where;
  i=1,2,3,..,K

- The first EMD mode is calculated for K different realisations of the input signal. The first EEMD mode ($\widetilde{I}_1$, Equation 3.31) is obtained as follows:

$$\widetilde{I}_1 = \frac{1}{K} \sum_{i=1}^{K} I_1^i = \bar{I}_1 \tag{3.31}$$

and the corresponding residue (γ_1) is obtained using Equation 3.29)

- The residue γ_1 is used to generate a new set of realisations γ^i, where i=1,2,3..,K.

$$\gamma^i = \gamma_1 + \beta_1 \varepsilon^i \tag{3.32}$$

- The first EMD mode is calculated for each of the K different realisations of γ^i

$$\gamma_1^i = \gamma_1 + \beta_1 \alpha_1 \varepsilon^i \tag{3.33}$$

Where; α_j is the operator, which yields the j$^{\text{th}}$ EMD mode (or the 1$^{\text{st}}$ EMD mode in this case)

- The second mode is obtained as

$$\widetilde{I}_2 = \frac{1}{K} \sum_{i=1}^{K} \alpha_1 \gamma_1 + \beta_1 \alpha_1 \varepsilon^i \tag{3.34}$$

- and the corresponding residue is obtained as

$$\gamma_2 = \gamma_1 - \widetilde{I}_2 \tag{3.35}$$

- Similarly, the j$^{\text{th}}$ residue (j=3,4,5,..,J different modes) can be obtained as:

$$\gamma_j = \gamma_{j\text{-}1} - \widetilde{I}_j \tag{3.36}$$

- Following the estimation of the second mode (Refer 3.34), the subsequent modes can be obtained using a similar approach. Therefore, the first EMD mode of $\gamma_j + \beta_j \alpha_j \varepsilon^i$, where i=1,2,3,...,K, is obtained and the j+1$^{\text{th}}$ CEEMDAN mode is identified as:

$$\widetilde{I}_{j+1} = \frac{1}{K} \sum_{i=1}^{K} \alpha_1 \gamma_j + \beta_j \alpha_j \varepsilon^i \tag{3.37}$$

and the subsequent residue can be obtained from equation 3.36

- These steps are repeated until further residue decomposition is not possible, and equation 3.38 holds true for the final residue (Γ), where, J represents the total number of modes.

$$\Gamma = OHC - \sum_{k=1}^{J} \widetilde{I}_j \tag{3.38}$$

- The OHC signal after CEEMDAN decomposition is expressed as

$$OHC = \sum_{k=1}^{J} \widetilde{I}_j + \Gamma \tag{3.39}$$

Energy Spectral Density of the OHC

The IMFs obtained from the CEEMDAN analysis are real valued signals and are distributed normally. The energy spectral density obtained has a χ^2 distribution [Wu and Huang, 2004 [107]]. For the ith mode, represented by Ii(t), the analytical signal is expressed as:

$$C_{\text{i}}(t) = Ii(t) + iT[Ii(t)], \tag{3.40}$$

$$C_{\text{i}}(t) = A_{\text{i}}(t)e^{i\theta_{\text{i}}(\text{t})} \tag{3.41}$$

Where for the ith mode $I_{\text{i}}(t)$;

T[·] denotes the Hilbert Transform Operator
$A_{\text{i}}(t)$ is the instantaneous amplitude
$\theta_{\text{i}}(t)$ is the instantaneous phase

The Hilbert Transform H(t) of a time-series X(t) is given by:

$$H(t) = \frac{1}{\pi}\textbf{p.v.} \int \frac{X(t')}{t - t'} dt' \tag{3.42}$$

Here,

p.v. denotes the Cauchy Principal Value
X(t) and its Hilbert Transform H(t) form the complex conjugate C(t). The analytical signal can then be expressed as:

$$C(t) = X(t) + iH(t) \tag{3.43}$$

The resulting complex signal can be used to easily extract the instantaneous frequency and energy. For the ith mode, the instantaneous frequency $\omega_{\text{i}}(t)$ is given as:

$$\omega_{\text{i}}(t) = \frac{d\theta_{\text{i}}(t)}{dt} \tag{3.44}$$

Thus, with equations (3.41) and (3.44), we calculate the complex signal corresponding to every mode and then the instantaneous frequency.

Marginalised Hilbert Spectrum

After the Hilbert Transform is performed on each mode, the Ocean Heat Content time series can be expressed as:

$$H(\omega, t) = \sum_{i=1}^{K} A_{\text{i}}(t)e^{i\int \omega_{\text{i}}(\text{t})\text{dt}} \tag{3.45}$$

Where;

The frequency-time distribution of the amplitude, H(ω,t), is referred to as the Hilbert Spectrum. H(ω,t) represents the joint distribution of the signal amplitude and frequency content as a function of time.

The Marginalised Hilbert Spectrum is used to describe the cumulated amplitude over the duration/length of each of our simulation in a probabilistic sense. From the Hilbert Spectrum, the Marginalised Hilbert Spectrum H(ω) can be obtained as:

$$H(\omega) = \int_t H(\omega, t)dt \tag{3.46}$$

Where;
H(ω) gives the total contribution corresponding to every frequency value (ω). The energy can be simply expressed as:

$$E(\omega) = |H(\omega)|^2 \tag{3.47}$$

4

Results

4.1 Model Evaluation

The first part of this chapter pertains to the evaluation of the two GCMs used in our study (Research Question 1: Subsection **1.4**). We ascertain if the models in question are capable of representing the characteristic water masses of the respective currents around Greenland, by examining the modelled Temperature and Salinity profiles with respect to the regridded CTD observations of the same (Methodology, Subsection **3.3**).

4.1.1 Eastern Margin

Helheim Glacier:

HADGEM2-ES Model:
Evaluating the modelled Temperature and Salinity fields, from the HADGEM2-ES model, we see that a warm core of AW is present offshore (Figure 4.1 (b)). The T-S characterisation of these modelled AWs relate well with the observation (Figure 4.2). However, they are not modelled as surface currents, as seen in the observations, but are present at depths of ∼100 meters.

For the purpose of our study, it is important to mention that the advection of heat from the Irminger Current, towards the continental shelf, and close to the Sermilik Fjord, is well represented in the model (Figure 4.1 (b)). The Deep Water classification is well represented in the HADGEM2-ES model (Figure 4.1 (b)).

GISS-E2-R Model:
Tracer classification of the GISS-E2-R model output, for the same section, reveals a deficient match with the observations (Figure 4.1 (c)). There is no agreement between the modelled and observed spatial location of the Irminger Current (Figure 4.1 (a)). Furthermore, the water mass signatures of the IC do not relate well with the observations.

More importantly, the Irminger Current does not propagate on to the Greenland shelf and remains offshore (Figure 4.1(c)). Lastly, the deep waters are not present in the GISS-E2-R model (Figure 4.1(c)). At greater depths, the model only depicts the warmest water masses, which are most likely, it's representation of the Irminger Current.

a)

b)

c)
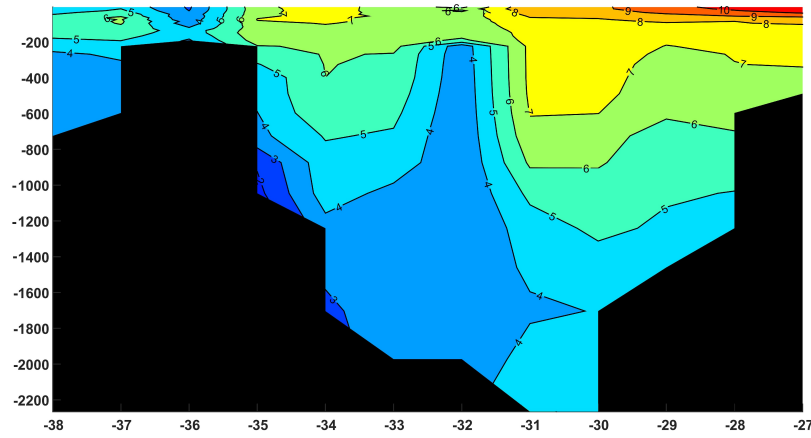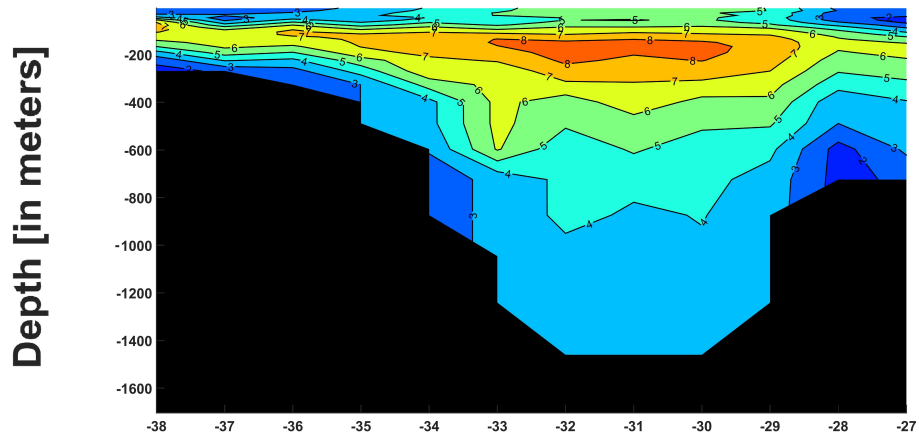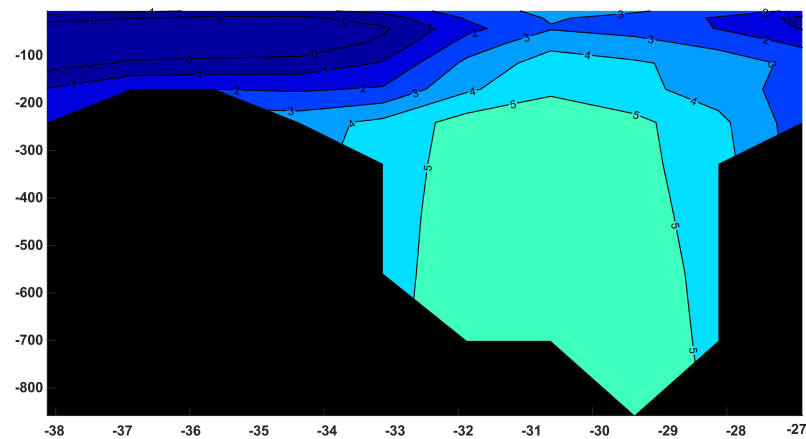
Figure 4.1: Potential temperature profile across the longitudinal section at Helheim Glacier as derived from a) CTD observations, b) HADGEM2-ES model, c) GISS-E2-R model.
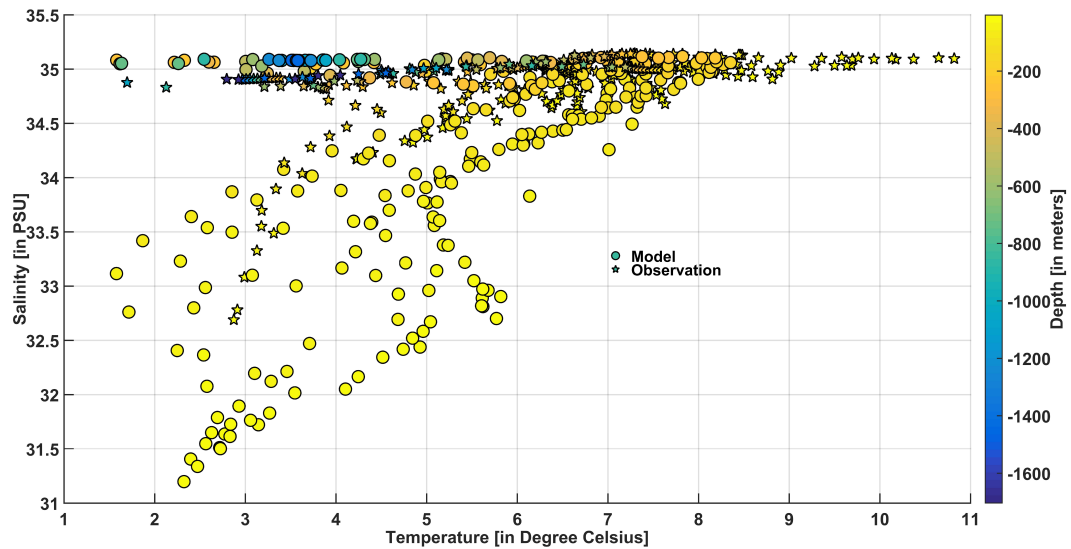
Figure 4.2: T-S characteristics of water masses found along the longitudinal section from Helheim Glacier for both the HADGEM2-ES model and the observation. The data points have been colour coded with the corresponding depths at which they are found

The DWs along this section (South of Denmark Strait) are formed by the overflowing waters of the Arctic, that cross the Denmark Strait, and continue their flow southwards. The absence of the DSOW in the GISS-E2-R model, therefore, could be the result of a relatively lower volume transport across the strait, as compared to the HADGEM2-ES model. The DW masses only appear in the GISS-E2-R model further southward (Not Shown Here). These are the DW masses of the ISOW, which in theory, join the DSOW in the Irminger Sea, and continue their journey southwards together, as the Deep Western Boundary Currents (DWBC).

Kangerlussuaq Glacier:

HADGEM2-ES model:

The model is able to capture the branch of Irminger Current which flows North-West, towards the Kangerlussuaq Fjord (Figure 4.3 (b)). The signatures of the subsurface waters present on the shelf are dependent on this branch of Irminger Current, and also the Return Atlantic Waters (RAWs), which flow southwards, as a subsurface current component of the EGC.

The observational records show that these AW masses are not present all along the shelf (Figure 4.3 (a)) as represented in the model, however, the characteristic tracer properties of the shelf AW agree fairly well (Figure 4.4). It can be inferred that the HADGEM2-ES model does well in its representation of the subsurface Atlantic currents on the shelf.

Towards the Icelandic shelf (21°W-18°W), close to the surface, we see the presence of Northern Icelandic Irminger Current (NIIC) (Figure 4.3 (b)). However, the modelled depth of this pathway of NIIC, extends deeper than the observed values. At greater depths, there is a gradual drop in the temperature values. Here, the modelled water mass signatures resemble the DWs, however, this DW layer representation is shallower and warmer (Figure 4.3 (b)) when compared to the observations (Figure 4.3 (a)).

South of Denmark Strait, the modelled Irminger Current component is relatively colder than the observational data. Therefore, the slight overestimation in the modelled temperature of the subsurface AWs on the Greenland shelf (Kangerlussuaq section), arises because the RAWs in the HADGEM2-ES model, are slightly warmer than their observed values (Refer: Appendix A.1.2; Figure A.2).

GISS-E2-R model:

The model does not properly model the subsurface AW signatures on the shelf (Figure 4.3 (c)). The contribution from the North-Western branch of the IC is in part, overcompensated by the RAWs . These RAWs are colder than the HADGEM2-ES model and the observational records (Refer: Appendix A.1.2; Figure A.2). Also, there is an overestimation of the Polar Water layer, as it extends up to depths of ∼200 meters (Figure 4.3 (c)). These inferences help to explain the relatively colder subsurface shelf waters.

The NIIC component is present in the GISS-E2-R model, however, not as a surface current (Figure 4.3 (c)). The model accurately represents the DWs, which are found below the NIIC.
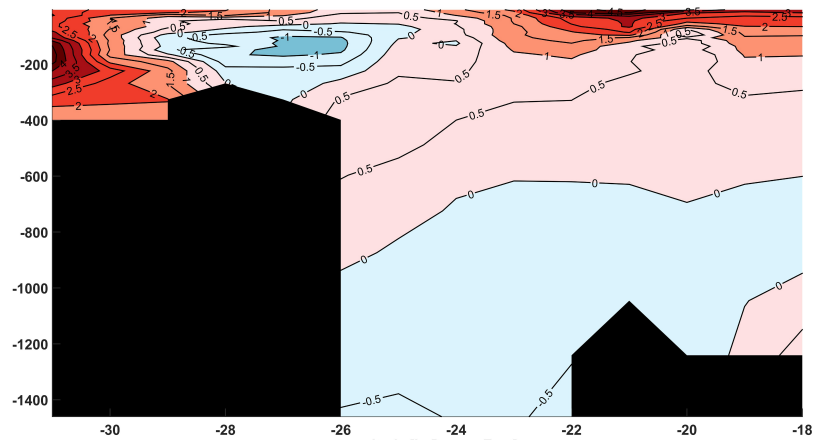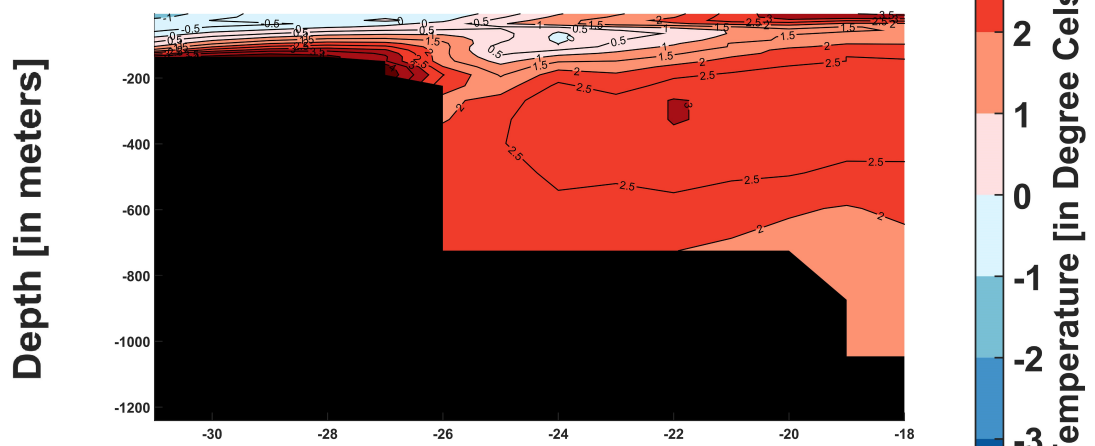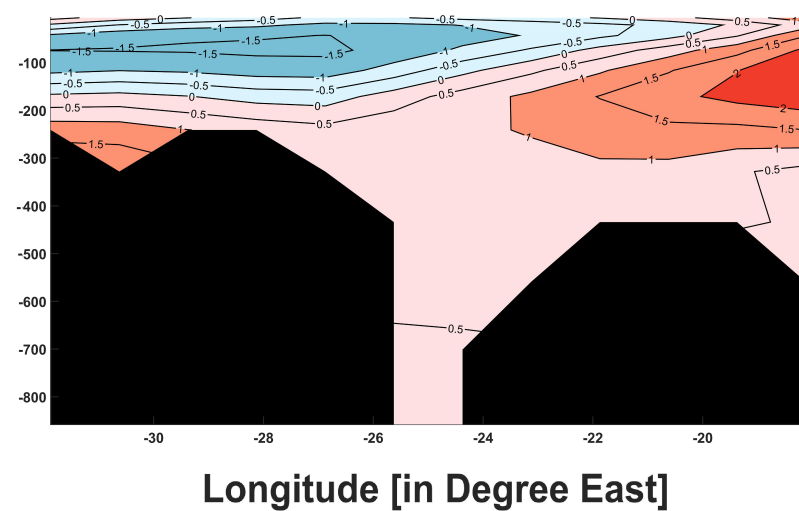
Figure 4.3: Potential temperature profile across the longitudinal section at Kanger-lussuaq Glacier as derived from a) CTD observations, b) HADGEM2-ES model, c) GISS-E2-R model.
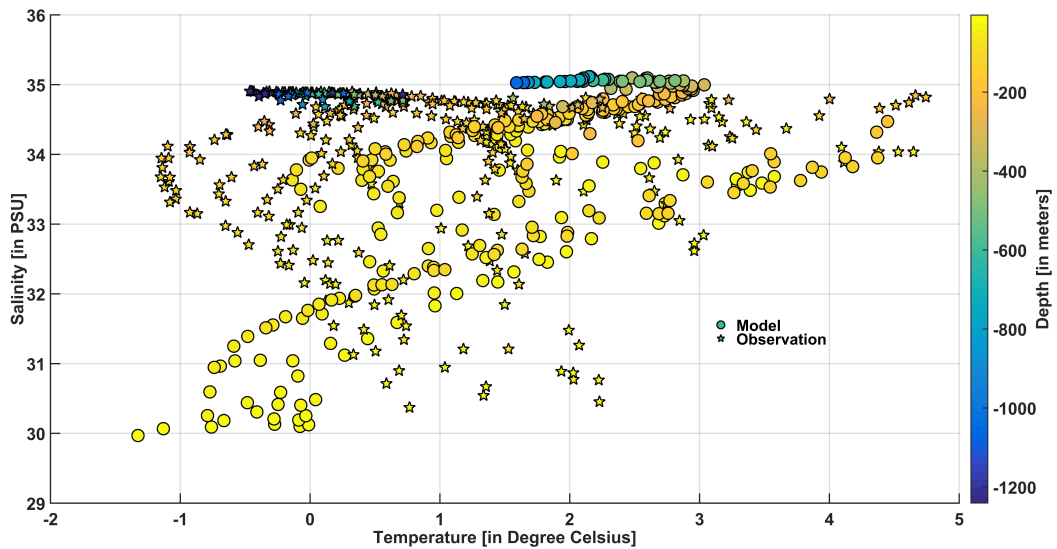
Figure 4.4: T-S characteristics of water masses found along the longitudinal section from Kangerlussuaq Glacier for both the HADGEM2-ES model and the observation. The data points have been colour coded with the corresponding depths at which they are found.

Summary: Eastern Margin

Our results clearly demonstrate that the GISS-E2-R model does not accurately model the subsurface AW properties on the Helheim and Kangerlussuaq longitudinal sections. At the Helheim Glacier section, the spatial representation of the Irminger Current component does not relate well the observations and the current is not seen to propagate on to the shelf. At Kangerlussuaq, the overestimation of the Polar Water layer on the shelf renders the subsurface AW representation incorrect. On the other hand, the HADGEM2-ES model relates fairly well with the observations. For our study purpose, an accurate modelled representation of subsurface oceanographic properties is of paramount interest. Based on this argument, and our evaluation of the two GCMs along the Eastern Margin, we opt to use the HADGEM2-ES model for further analysis.

4.1.2 Western Margin

Jakobshavn Isbræ:

HADGEM2-ES Model:
The model is able to capture the observed transition in tracer properties from the East (Figure 4.1(a) and (b), Figure 4.3 (a) and (b)) to the West of Greenland (Figure 4.5 (a) and (c)). However, the Polar Water layer is thicker ($\sim$200 meters), colder and fresher than the observed values (Figure 4.5 (a)) and the GISS-E2-R model (Figure 4.5 (b)).

Below the PWs, the model shows the presence of a relatively warm and saline AW layer (Figure 4.5 (c), Figure 4.6 (b) and (c)). These water masses have signatures that relate to the presence of Irminger Mode Waters (IMWs) and Northwest Atlantic Mode Waters (NAMWs). However, the heat from these Irminger Current sources are not advected towards the shelf. Therefore, unlike the observations (Figure 4.5 (a)), these IMWs and NAMWs do not reach the continental shelf (Figure 4.5 (c)).

The baroclinic instability towards the western margin is well modelled. To that extent, we see that the currents (PWs and AWs) are not just contained to the shelf break (as observed in Eastern Greenland) but extends over the deep basin as well (Figure 4.5 (c)).

Below the AWs, the temperatures begin to gradually decrease with depth (Figure 4.5 (c)). However, the salinity stratification remains the same (Figure 4.6 (c)). Furthermore, the temperatures are still not comparable to Deep Water temperatures (Figure 4.5 (c)). This thin layer of water mass, is therefore, more likely to be a variant of NAMWs. The transition of AWs to DWs is not completed within the framework of our modelled section.

GISS-E2-R model:
The model is also able to resolve the observed transition in tracer properties, along with modelling the baroclinic instability towards the west (Figure 4.5 (b), Figure 4.6 (a)). The extent of the PW layer relates very well with the observations (Figure 4.5 (a)). The modelled PW characteristics are found to be relatively less warmer. However, the values lie within the typical temperature range for PWs found along the western Greenland margins .

The modelled AWs that lie below the PWs, represent the NAMWs in terms of their water mass characteristics. However, just like the PWs, these AW masses (Figure 4.5 (b)) are also relatively less warm than the observed values (Figure 4.5 (a)). They do show a propensity to climb on to the Greenland shelf (Figure 4.5 (b)), unlike the HADGEM2-ES model (Figure 4.5 (c)).

The DW layer is well represented in the GISS-E2-R model (Figure 4.6 (a), Figure 4.5 (b)).

Subsection A.1.1 of the Appendix, characterises the modelled surface water anomaly as seen in the HADGEM2-ES model (Figure 4.5 (c) and 4.6 (b) and (c) based on our inferences from the modelled sea-ice concentration, (surface) temperature and salinity profiles.

Summary: Western Margin

Along the Jakobshavn longitudinal section, we found that the HADGEM2-ES model overestimates the PW layer thickness and the AWs sitting below are not able to climb on to the shelf, unlike the observed representation.

The GISS-E2-R models the Polar Waters and the subsurface AWs fairly well. More importantly, the subsurface NAMWs and the IMWs are found to be present on the shelf.

Owing to it's accurate representation of the AW inflow near Jakobshavn, we opt to use the GISS-E2-R model for our study. It is noteworthy to point out that we will be using different models for the eastern and western margin. However there is minimal inter-model discrepancy across the western margin compared to the east. Both the models are able to represent the dominant modes of the West Greenland Current (WGC). Therefore, results from GISS-E2-R model at Jakobshavn can be used in conjunction with the representation of the Eastern Margin by the HADGEM2-ES model, to draw conclusions regarding the spatial differences between the Eastern and Western Greenland margins.

a)
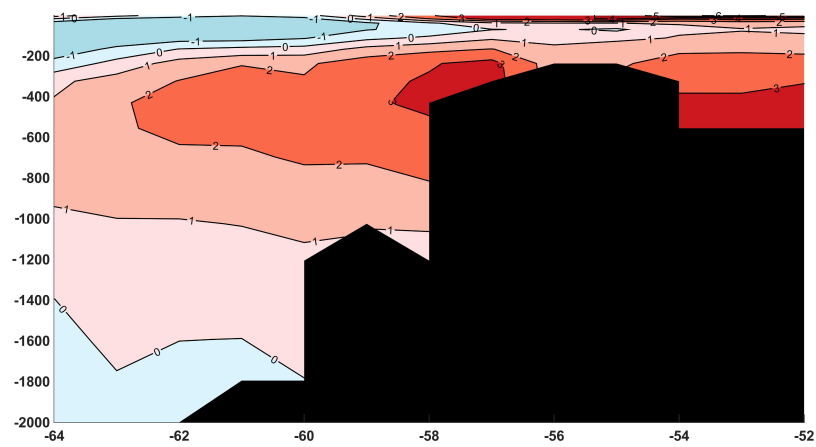
b)
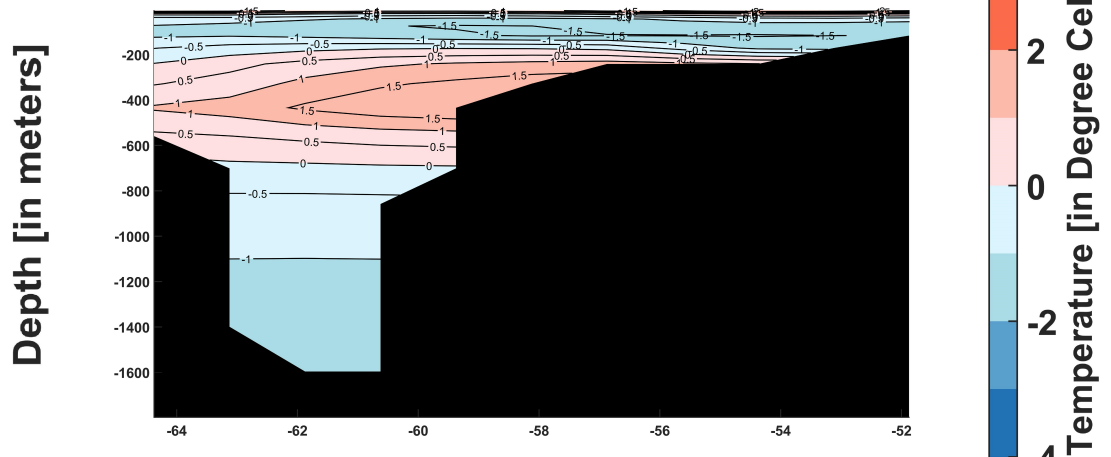
c)
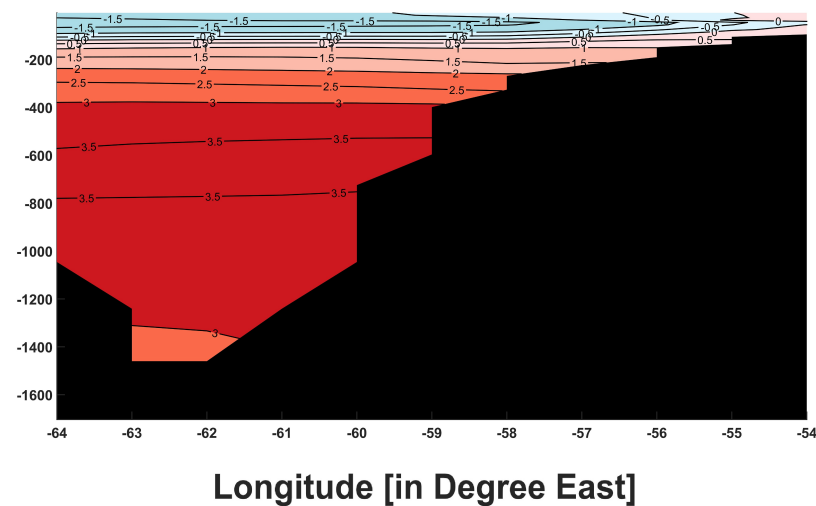
Figure 4.5: Potential temperature profile across the longitudinal section at Jakobshavn as derived from a) CTD observations, b) GISS-E2-R model, c) HADGEM2-ES model.
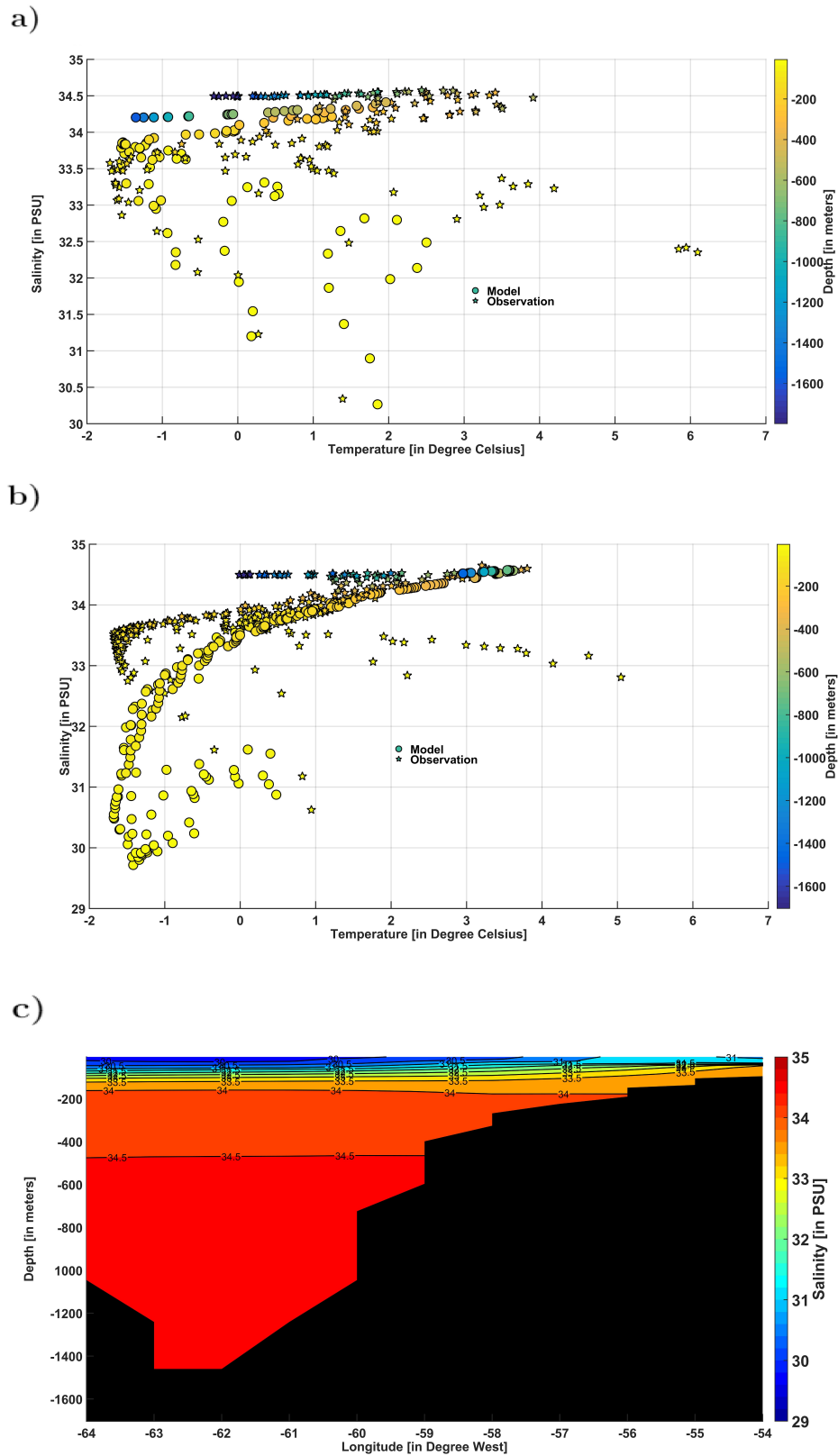
Figure 4.6: **a), b)** represents the GISS-E2-R and HADGEM2-ES derived T-S characteristics plotted against the observed values. **c)** Modelled salinity profile (HADGEM2-ES model) accross the longitudinal section at Jakobshavn.

4.2 Changes in spatial variability in the ocean heat forcing

In this part of the chapter, we examine the response of dominant ocean currents around Greenland to GHG forcing. To that extent, results for the Historical and RCP 8.5 simulations are presented relative to the Pre industrial climate. Emphasis is laid on addressing the modelled spatial variability in the distribution of warmer subsurface AWs, present on the Greenland continental shelf, around our study locations. (Research Question **2**: Subsection 1.4).

Helheim Glacier:

Anomaly [Historical simulation]:

The modelled anomaly for the Historical simulation (A.D. 1985-2005) with respect to the Pre-Industrial simulation (20 year period) shows that the Irminger Current reaching the shelf gains both in heat and salt (Figure 4.7 (c)). The subsurface AWs (Figure 4.7 (a)) are warmer by ∼1°C.

Anomaly [RCP 8.5 simulation]:

In a future warming scenario (A.D. 2075-2095), the anomaly with respect to the Pre-Industrial climate shows a considerable warming of both the surface and subsurface waters on the shelf (Figure 4.7 (b)). There is an increase in salinity (Figure 4.7 (c)), however, this is compensated in part by an enhanced freshening of the upper ∼150 meters. This is driven by a declining winter sea-ice concentration leading to enhanced winter precipitation (Refer: Appendix, Figure A.3 and Figure A.5 (a)).

Inference:

It can be argued that the net increase in subsurface salinity seen for the Historical simulation arises due to a gradual increase in the AW inflow from the subtropics, which bring in more inorganic solutes with them. These are then effectively communicated to the shelf, close to the Sermilik Fjord, via the westward branch of Irminger Current (Figure 4.7 (a): The Irminger Current can be seen as the subsurface current component between the 100-700 meter depth).

For the RCP 8.5 simulation (Figure 4.7 (b)), the gain in heat at the shelf, is considerably higher than the Historical simulation (Figure 4.7 (a)). The surface layer gaining in heat translates to a declining sea-ice concentration. This further leads to an enhanced (winter) precipitation, which is seen to compensate for the gain in salinity as seen in the Historical simulation up to depths of ∼150 meters (Refer: Appendix, Figure A.5 (a)).

The continental shelf, north of the Denmark Strait (DS), and close to Kangerlussuaq, is comparatively shallower than the Helheim Glacier (shelf) (Figure A.6: 67-68°N).

Owing to this spatial disparity, it can be argued that only a small fraction of the subsurface AW component of the EGC arrives at the Helheim Glacier (shelf) (Figure A.6 (a) and (b)). These water masses, along with the Denmark Strait Overflow Waters (DSOW), are much colder (Figure A.7) compared to the water masses found south of the Denmark Strait. As a result, they sink below the Irminger Current and usually correspond to the Deep Water masses found south of the Denmark Strait.

It also becomes clear from Figure 4.7, that the only water masses that gain in both heat and salt, for both the simulations, are these overflowing DW masses south of the Denmark Strait. More importantly, these DWs show a greater sensitivity towards a future warming scenario. Comparing the subsurface water mass signatures in Figure 4.7 (a) and 4.7 (b), it can be inferred that the modelled anomaly in temperature for the DWs is substantially greater than the IC waters.

Therefore, in terms of subsurface temperature magnitudes, the Irminger Current (IC) is the dominant heat transporting current towards the Helheim Glacier (shelf). However, the RAWs are seen to depict a greater sensitivity in response to the GHG forcings.
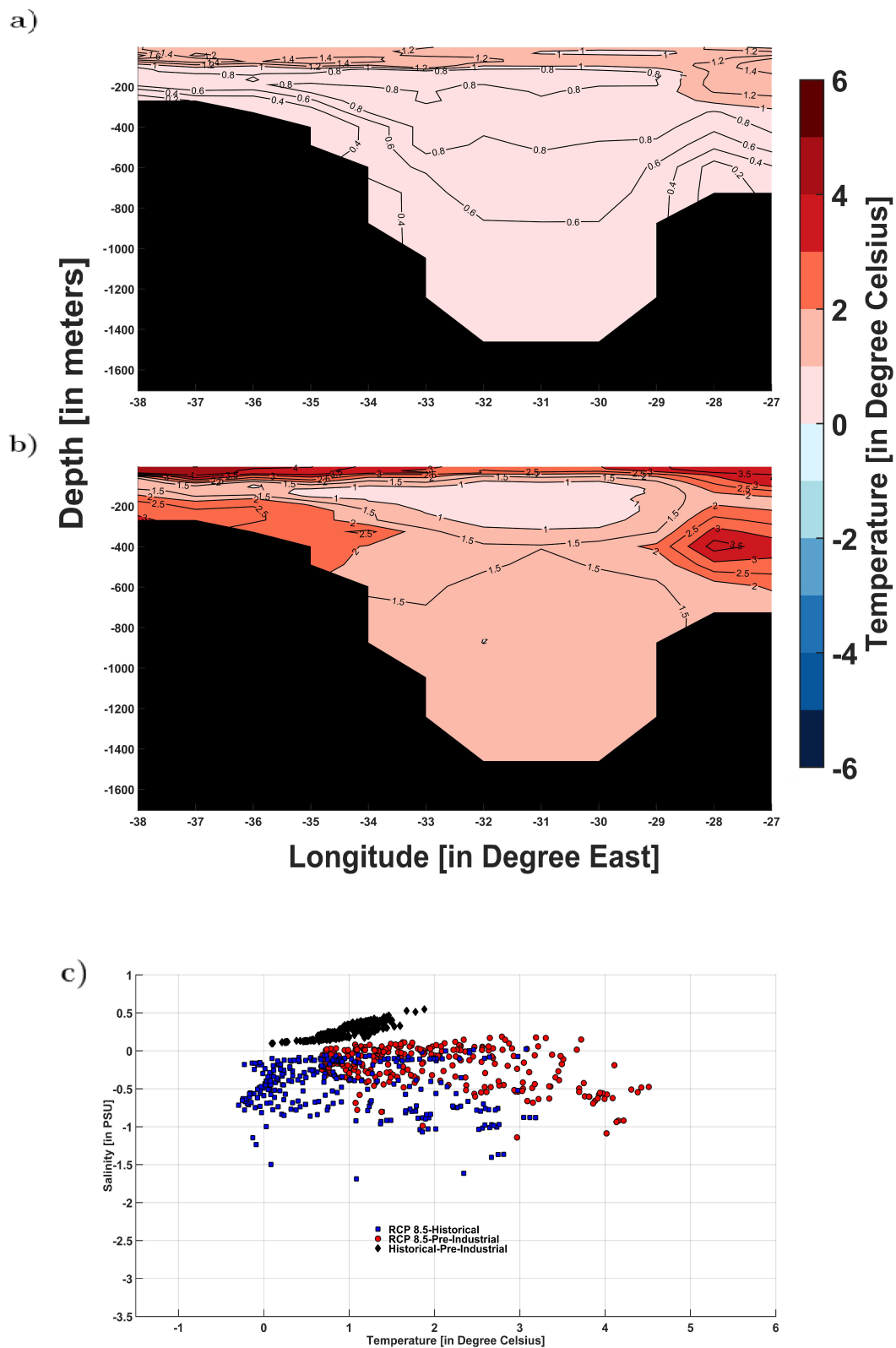
Figure 4.7: HADGEM2-ES derived modelled temperature anomaly across the Helheim Glacier section for **a)** Historical - Pre Industrial and **b)** RCP 8.5-Pre-Industrial. Figure 4.7 **c)** shows the anomaly in the modelled T-S characteristics for the different simulations.

Kangerlussuaq Glacier:

Anomaly [Historical simulation]:

The anomaly in the Historical simulation (A.D. 1985-2005), with respect to Pre-Industrial values, shows that the AWs on the shelf, close to the Kangerlussuaq fjord, gain in heat and salt (Figure 4.8 (a) and (c)). This gain is greater than the modelled subsurface temperature anomaly as seen for the Helheim Glacier (shelf) (Figure 4.7 (a) and 4.8 (a)).

Anomaly [RCP 8.5 simulation]:

For the RCP 8.5 simulation, we notice an anomaly in the subsurface warming (Figure 4.8 (b)) considerably greater than the Helheim Glacier (Figure 4.7 (b)). Furthermore, the gain in subsurface salinity (Figure 4.8 (c)) is substantially higher than the Helheim Glacier (shelf) (Figure 4.7 (c)).

Inference:

The continental shelf close to the Sermilik Fjord, is in close proximity to the (modelled) warm core of the Irminger Current (Figure 4.7 (a) and (b)). Only a fraction of the heat (and salt) from this current migrates further North-West towards Kangerlussuaq Glacier (shelf) (Figure A.6).

If the Irminger Current is the only dominating heat transporting Atlantic current along the Eastern Margin, the Helheim Glacier (shelf) would show a greater response to GHG forcing. However, our results do not validate this hypothesis, as we infer that the subsurface warming along the Kangerlussuaq shelf (Figure 4.8 (a) and (b)) shows a relatively greater sensitivity towards GHG forcings, as compared to the Helheim region (Figure 4.7 (a) and (b)).

The sensitivity of subsurface AWs close to Kangerlussuaq Glacier (shelf) can be explained by the role of Irminger Current in conjunction with the Return Atlantic Waters.

In a Pre-Industrial climate, these subsurface waters of the East Greenland Current (EGC) are much colder compared to the AWs of the IC found south of the Denmark Strait (Refer: Appendix, Figure A.7). This results in a compensating effect when a warm subsurface Irminger Current component mixes with the colder subsurface Return Atlantic Waters.

However, these RAWs are found to gain more heat in response to the anthropogenic forcing (Refer: Figure 4.8 (a) and Appendix, Figure A.8 (a)) than the IC. As a result, the RAW anomaly with respect to the Pre-Industrial climate is substantially higher than the IC anomaly (Figure 4.7 (a)).

This effect is greatly amplified in a future warming scenario (RCP 8.5 simulation) (Refer: Figure 4.8 (b) and Appendix, Figure A.8 (b)). This negates the previously discussed compensating effect of these RAWs, as seen in a Pre-Industrial climate. The anomaly (A.D. 2075-2095) with respect to Pre-Industrial values shows a substantial rise in both temperature and salinity values (Figure 4.8 (b), Figure 4.8 (c)).

Furthermore, for a future warming scenario, a gain in subsurface salinity (Figure 4.8 (c)), that is greater than Helheim Glacier (shelf) (Figure 4.7 (c)), suggests that the RAW inflow exceeds the IC inflow near Kangerlussuaq.
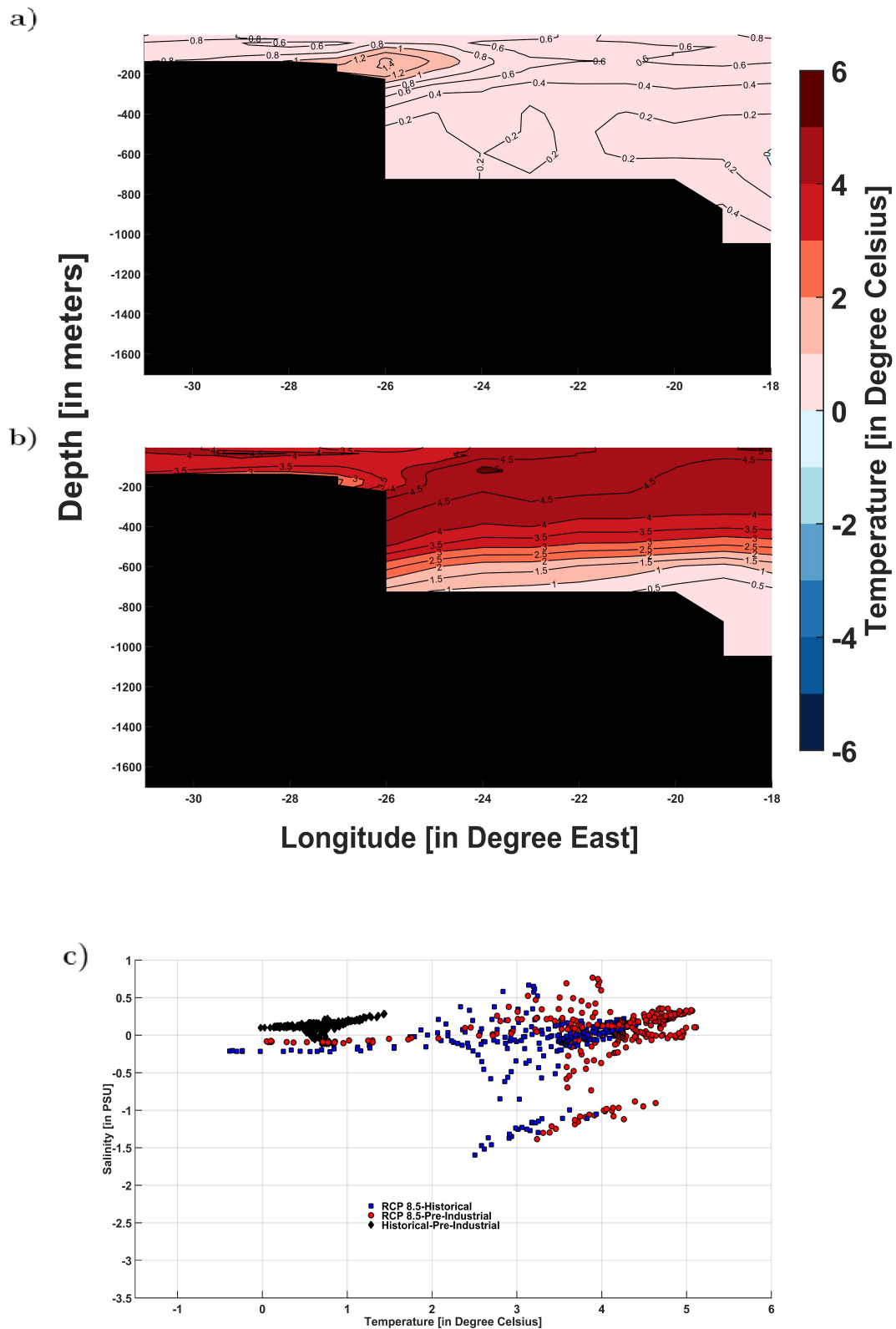
Figure 4.8: HADGEM2-ES derived modelled temperature anomaly across the Kangerlussuaq Glacier section for **a)** Historical - Pre Industrial and **b)** RCP 8.5-Pre-Industrial. Figure 4.8 **c)** shows the anomaly in the modelled T-S characteristics for the different simulations.

Jakobshavn Isbræ:

Anomaly [Historical simulation]:

The modelled Historical anomaly (A.D. 1985-2005) with respect to Pre-Industrial climate, near Jakobshavn Isbræ, shows an increase in both heat and salt (Figure 4.9 (a) and (c)), with a subsurface warming of ∼1°C (Figure 4.9 (a)).

Anomaly [RCP 8.5 simulation]:

In a future warming scenario (A.D. 2075-2095), the modelled anomaly shows a considerable increase in subsurface temperatures (Figure 4.9 (b)). These are comparable to the modelled subsurface temperature anomalies near the Helheim Glacier (shelf). However, the modelled salinity anomaly shows considerable freshening of both the surface and subsurface water masses on the shelf (Figure 4.9 (c), Figure A.5 (c)). This freshening is substantially higher than the Helheim and Kangerlussuaq region. In the GISS-E2-R model, the sea-ice retreat peaks during late summer/autumn. This retreat is substantially higher than our inferences from the Eastern Margin. Furthermore, the retreat is concordant with a late summer/autumn amplification of the mean-annual precipitation cycle (Refer: Appendix, Figure A.4), which could explain the enhanced freshening.

Inference:
The subsurface warming at Jakobshavn is a consequence of the warming of the Irminger Mode Waters. These currents are carried towards the west by the East Greenland Current. The magnitude of this warming, therefore, relates well with the subsurface warming seen across the Eastern Margin; particularly the Helheim Glacier (shelf).

Below is a table that shows the subsurface temperature sensitivity of the shelf corresponding to each location for the Historical and RCP 8.5 scenario with respect to the Pre-Industrial scenario.

Location	Historical	RCP 8.5
Helheim	0.94°C	2.38°C
Kangerlussuaq	0.77°C	3.76°C
Jakobshavn	0.85°C	1.92°C

Table 4.1: Increase in mean subsurface temperatures of the shelf for the Historical and RCP 8.5 scenario with respect to the Pre-Industrial scenario.
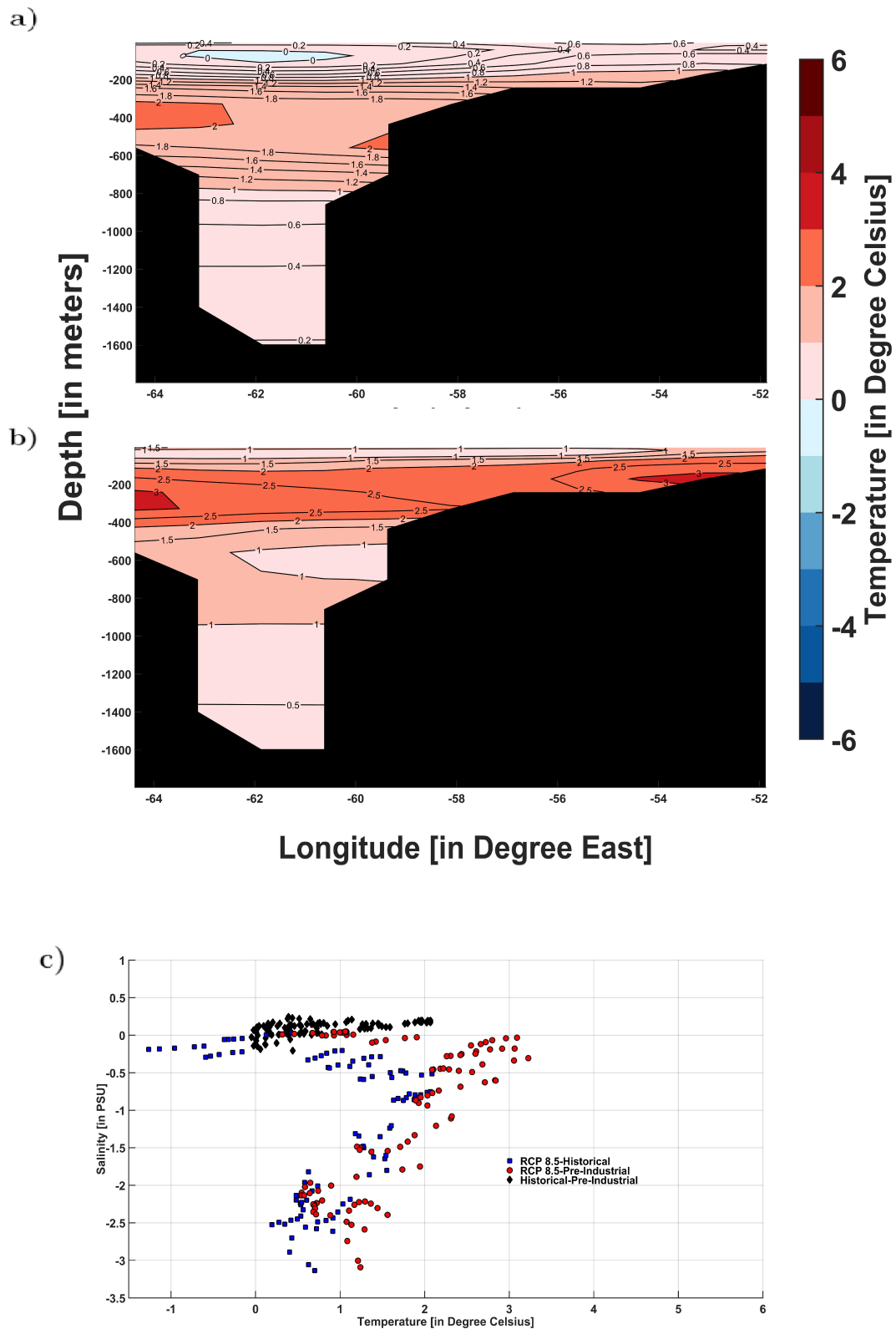
Figure 4.9: GISS-E2-R derived modelled temperature anomaly across the Jakobshavn Glacier section for **a)** Historical - Pre Industrial and **b)** RCP 8.5-Pre-Industrial. Figure 4.9 **c)** shows the anomaly in the modelled T-S characteristics for the different simulations.

4.3 Changes in temporal variability in the ocean heat forcing

Lastly, we quantify the spatio-temporal (decadal/multi-decadal) variability in the modelled Ocean Heat Content (OHC) around our study locations (Research Question **3**: Subsection 1.4). As we are particularly interested in the modelled subsurface (Atlantic Water) forcing to the Greenland shelf, we do not include the offshore region in our computation. Table 4.2 indicates the grid details corresponding to each study region used in our OHC analysis.

Location	Grid Details	Depth (in meters)
Helheim	38-35°W, 65°N	50-400
Kangerlussuaq	31-26°W, 68°N	50-250
Jakobshavn	52-58°W, 69°N	50-400

Table 4.2: Section details corresponding to our study regions for OHC analysis

We decompose the Ocean Heat Content time-series based on their intrinsic oscillatory modes using the CEEMDAN approach (Refer Methodology: subsection 3.5). This is driven by our hypothesis that the response of the ocean (to anthropogenic GHG forcing) can be categorised based on their frequency. The short-term (or high-frequency) response manifests itself over monthly timescales. The long-term (or low-frequency) response occurs over larger (multi-year/decadal) timescales. As the Pre-Industrial simulation does not include any external forcing, such responses could be seen as the natural variability of the climate system. Marginal Hilbert Spectrum of the modes (Refer Methodology: subsection 3.5) is used to express the distribution of energy over frequency.

Helheim Glacier:

Pre-Industrial simulation:

The OHC derived from the Pre-Industrial simulation is composed of considerable high-frequency variability (Figure A.9 and Table 4.4). In Table 4.4, modes c1-c4 (Figure A.9) correspond to sub-annual frequencies and contain 2.08% of the total energy content of the Pre-Industrial OHC signal. This is comparatively higher than the Historical (1.03%) and RCP 8.5 simulation (0.001%). The signal reconstructed from the high-frequency modes (c1-c4, Figure A.9) shows that most of the energy is contained around a 2 month period (Figure 4.11 **(b)**).

The Marginal Hilbert Spectrum obtained from the low-frequency IMFs (c5-c9, Figure A.9) of the Pre-Industrial simulation shows a small quasi-decadal (3 year and 6 year) periodicity. The energy contained at these periods are, however, an order of magnitude smaller than our inferences for the Historical and RCP 8.5 simulation. This can be seen from Figure 4.11 **(a)**.

Historical simulation:

On multi-year/quasi-decadal timescales, the Marginal Hilbert Spectrum obtained from the low-frequency modes of the Historical simulation (c5-c9, Figure A.10), shows considerable low frequency variability compared to the Pre-Industrial and RCP 8.5 OHC signal. This can be seen in Figure 4.11 **(a)**. To that extent, we see that most of the energy contained at 3-5 year periods. A 6 year cycle, similar to the Pre-Industrial signal is present, however, the energy contained at this period is substantially higher for the Historical signal than both the Pre-Industrial and RCP 8.5 signal.

The signal reconstructed from the high-frequency modes (c1-c4, Figure A.10) shows that most of the energy is contained around a 2 month period (Figure 4.11 **(b)**). Furthermore, this energy is considerably higher than both the Pre-Industrial and RCP 8.5 signal.

There are periods of strong peaks in the modelled Historical OHC, some of which are comparable to the RCP 8.5 simulation. This is clearly visible for the period from 1925-1930 (Figure 4.10).

A dominant increasing trend (Figure 4.10, Table 4.3) is observed in the last 20 years, towards the turn of the 21st century **(A.D. 1985-2005)**. This is comparable in magnitude to the RCP 8.5 modelled trend (Table 4.3) towards the end of the 21st century (A.D. 2055-2095).

RCP 8.5 simulation:

On multi-year/quasi-decadal timescales, the Marginal Hilbert Spectrum obtained from the low-frequency modes of the RCP 8.5 simulation (c5-c9, Figure A.11) shows a 6 year cycle, similar to the Pre-Industrial and Historical signal. The energy contained at this period is greater than the Pre-Industrial period. This can be seen in Figure 4.11 **(a)**. Most of the energy in the RCP 8.5 signal is contained at a decadal period. The Historical and Pre-Industrial signal do not show such a cycle.

The signal reconstructed from the high-frequency modes (c1-c4, Figure A.11) shows that most of the energy is contained around a 2 month period (Figure 4.11 **(b)**), consistent with our inference from the Pre-Industrial and Historical signal. The energy contained at this period is comparable to the Pre-Industrial signal.

Most of the RCP 8.5 signal is composed of a dominant low-frequency long-term trend (Table 4.4, Figure A.11).To that extent, two different trends over 50 year duration are identified (Figure 4.10). The first 50 year period (A.D. 2006-2054) shows a decreasing trend, which is followed by a strong increasing trend in the period A.D. 2055-2095 (Table 4.3).

Simulation	Time-Period	Trend [in J/m²/month)
Historical	1916-2005	2.46×10^6
Historical	1985-2005	1.13×10^8
RCP 8.5	2006-2095	2.36×10^7
RCP 8.5	2006-2054	-1.73×10^7
RCP 8.5	2055-2095	1.00×10^8

Table 4.3: The modelled upper-ocean heat content trend for the Historical and the RCP 8.5 simulations for the Helheim Glacier. The Historical and the RCP 8.5 simulation derived OHC density are presented as anomalies with respect to the mean of the Pre-Industrial climate.
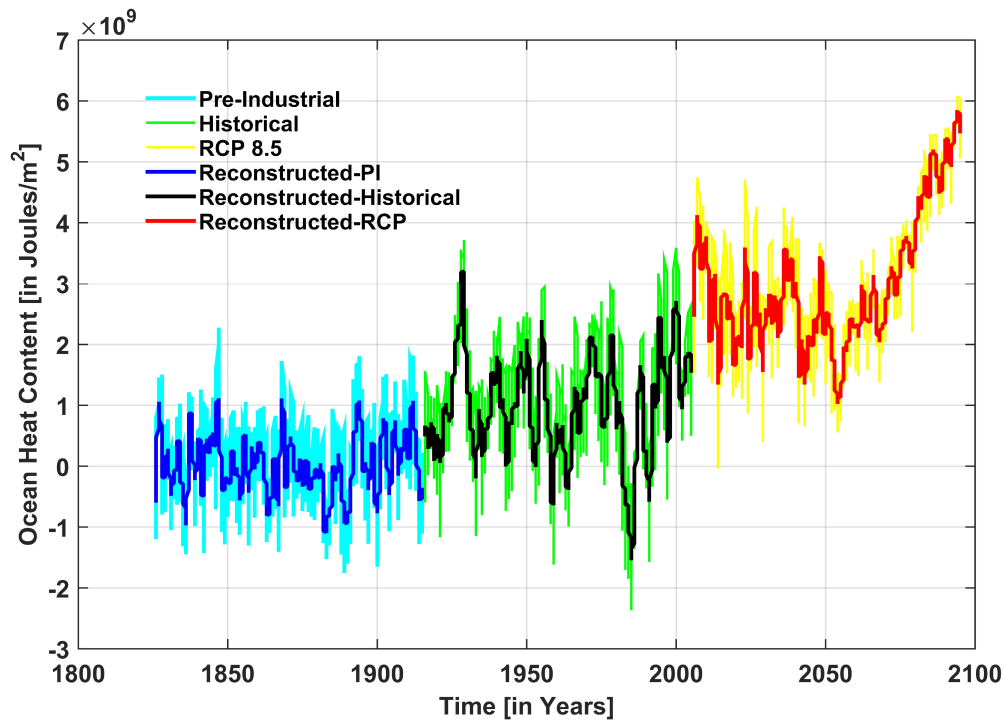
Figure 4.10: Modelled monthly ocean heat content density derived from the HADGEM2-ES model for the Helheim Glacier section. The Historical and RCP 8.5 simulation derived OHC are expressed as anomalies with respect to the mean of the Pre-Industrial Values. The Deep Blue, Black and Red colours correspond to the Reconstructed Pre-Industrial, Historical and RCP 8.5 simulations respectively. The Reconstructed Pre-Industrial is obtained from the last 7 IMFs, labelled from c5-c11 in Figure A.9. The Reconstructed Historical and RCP 8.5 signals are obtained from the last 6 Intrinsic Mode Functions (IMFs), labelled from c5-c10 in Figure A.10 and A.11 respectively.
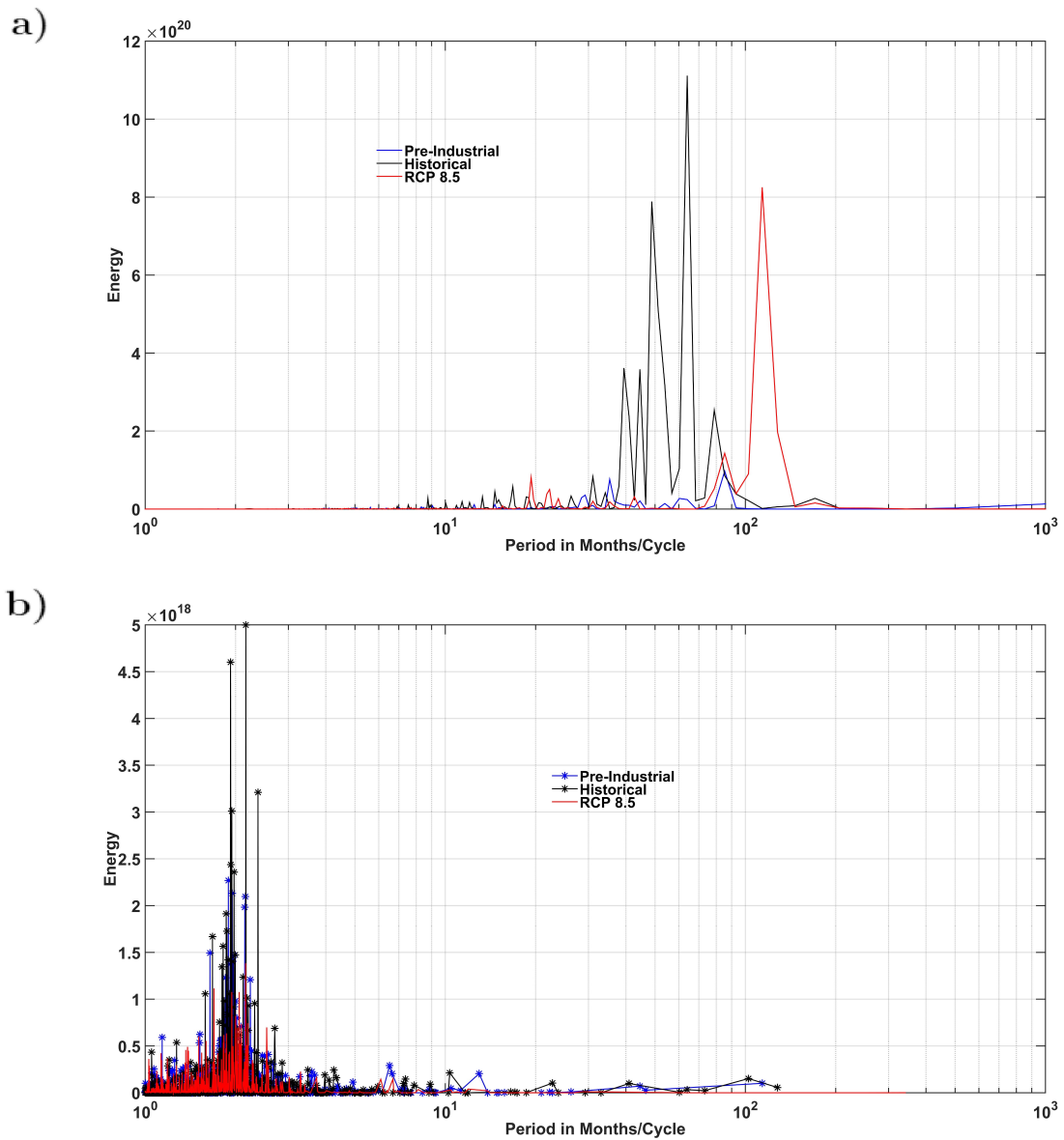
Figure 4.11: Helheim Glacier section: Marginal Hilbert Spectrum of Energy (in Joules^2/m^4) versus Period (in Months/Cycle) for the Pre-Industrial (Blue), Historical (Black) and RCP 8.5 (Red) OHC signal derived from the HADGEM2-ES model, using **a)** the low-frequency (c5-c9) modes and **b)** the high-frequency (c1-c4) modes corresponding to each simulation. The low frequency modes (c5-c9) contain the multi-year cycles, whereas, the high-frequency modes (c1-c4) contain the intra-annual cycles.

Below, in Table 4.4, we provide the energy contained in each mode (Refer A.2.2: Helheim Glacier) corresponding to each of the three simulations. Furthermore, we express the contribution of each of these modes to the total energy as percentages.

	Helheim Glacier					
	Pre-Industrial		Historical		RCP 8.5	
Mode	Energy	% of Total	Energy	% of Total	Energy	% of Total
c1	1.51×10^{19}	0.36	2.05×10^{19}	0.03	1.30×10^{19}	0.033×10^{-2}
c2	8.17×10^{17}	0.02	3.52×10^{19}	0.04	5.35×10^{17}	0.001×10^{-2}
c3	4.52×10^{19}	1.06	4.43×10^{19}	0.05	2.69×10^{19}	0.067×10^{-2}
c4	2.73×10^{19}	0.64	7.44×10^{20}	0.91	6.12×10^{19}	0.002
c5	7.24×10^{19}	1.70	4.44×10^{19}	0.05	4.75×10^{19}	0.001
c6	1.09×10^{20}	2.59	4.11×10^{20}	0.50	6.95×10^{19}	0.002
c7	3.92×10^{19}	0.92	6.68×10^{20}	0.81	3.65×10^{20}	0.009
c8	2.92×10^{20}	6.88	2.74×10^{21}	3.34	1.90×10^{20}	0.005
c9	1.15×10^{20}	2.71	6.80×10^{19}	0.08	1.18×10^{21}	0.029
c10	2.25×10^{21}	53.01	7.74×10^{22}	94.18	3.99×10^{24}	99.951
c11	1.28×10^{21}	30.10	N/A	N/A	N/A	N/A

Table 4.4: For each of the three simulation corresponding to Helheim Glacier, the table contains the energy (in Joules^2/m^4) contained in every decomposed Intrinsic Mode Function (IMF). The contribution of each IMF towards the total energy is expressed as percentages.For the Historical and RCP 8.5 simulation, there are only 10 IMFs, and therefore, N/A denotes Not Applicable.

Kangerlussuaq Glacier:

Pre-Industrial simulation:

The signal reconstructed using the high-frequency modes (c1-c4, Figure A.12) shows that most of the energy is contained around a 2 month period (Figure 4.13 **b**), similar to our inferences from Helheim Glacier. Furthermore, in Table 4.6, modes c1-c4 (Figure A.12) correspond to sub-annual frequencies and contain 2.71% of the total energy content of the Pre-Industrial OHC signal. This is comparatively higher than the Historical (0.90%) and RCP 8.5 simulation (0.005%).

The Marginal Hilbert Spectrum obtained from the low-frequency modes (c5-c8, Figure A.12) shows a small multi-year (3 year) periodicity. The energy contained at this period is relatively higher than the Historical simulation. This can be seen in Figure 4.13 **a**.

Historical simulation:

On multi-year timescales, the Marginal Hilbert Spectrum obtained from the low-frequency modes of the Historical simulation (c5-c8, Figure A.14) shows considerable low-frequency variability compared to the Pre-Industrial and RCP 8.5 OHC signal (Figure 4.13 **a**). To that extent, we see some of the energy contained at multi-year (2 and 3 year) cyles. However, most of the energy is contained at a 5 year period. This is substantially higher than the energy contained in the Pre-Industrial and RCP 8.5

signal at any particular period.

The energy contained in the high-frequency modes (c1-c4, Figure A.13) is centred around a 2 month period, and, is considerably higher than both the Pre-Industrial and RCP 8.5 signal (Figure 4.13 **b**), consistent with our inferences from Helheim Glacier.

The last 20 years of the Historical signal is marked by a dominant increasing trend (Figure 4.12), similar to that of Helheim Glacier (Figure 4.10). However, the modelled trend is an order of magnitude lower than the Helheim Glacier (Table 4.3 and 4.5).

RCP 8.5 simulation:

The RCP 8.5 derived OHC signal shows a consistent increasing trend throughout the simulation (Figure 4.12), unlike our inferences from Helheim (Figure 4.10) where the first half of the 21st century showed a decreasing trend. Furthermore, compared to Helheim Glacier, the trend over the entire period (A.D. 2005-2095) is considerably higher (Table 4.5).

A multi-year (2 year) cycle is seen. The energy contained at this period is, however, an order of magnitude smaller than the energy contained at Historical and Pre-Industrial signal at other periods (Figure 4.13 **b**).

The signal reconstructed from the high-frequency modes (c1-c4, Figure A.14) shows that most of the energy is contained around a 2 month period (Figure 4.13 **(b)**), similar to our findings for the Helheim Glacier. The energy contained at this period is comparable to the Pre-Industrial signal.

Simulation	Time-Period	Trend [in $J/m^2/month$)
Historical	A.D. 1916-2005	1.35×10^7
Historical	A.D. 1985-2005	9.16×10^7
RCP 8.5	A.D. 2006-2095	1.01×10^8
RCP 8.5	A.D. 2006-2054	5.38×10^7
RCP 8.5	A.D. 2055-2095	2.02×10^8

Table 4.5: The modelled upper-ocean heat content trend for the Historical and the RCP 8.5 simulations expressed in Joules/m²/month for the Kangerlussuaq Glacier. The Historical and the RCP 8.5 simulation derived OHC density are presented as anomalies with respect to the mean of the Pre-Industrial climate.
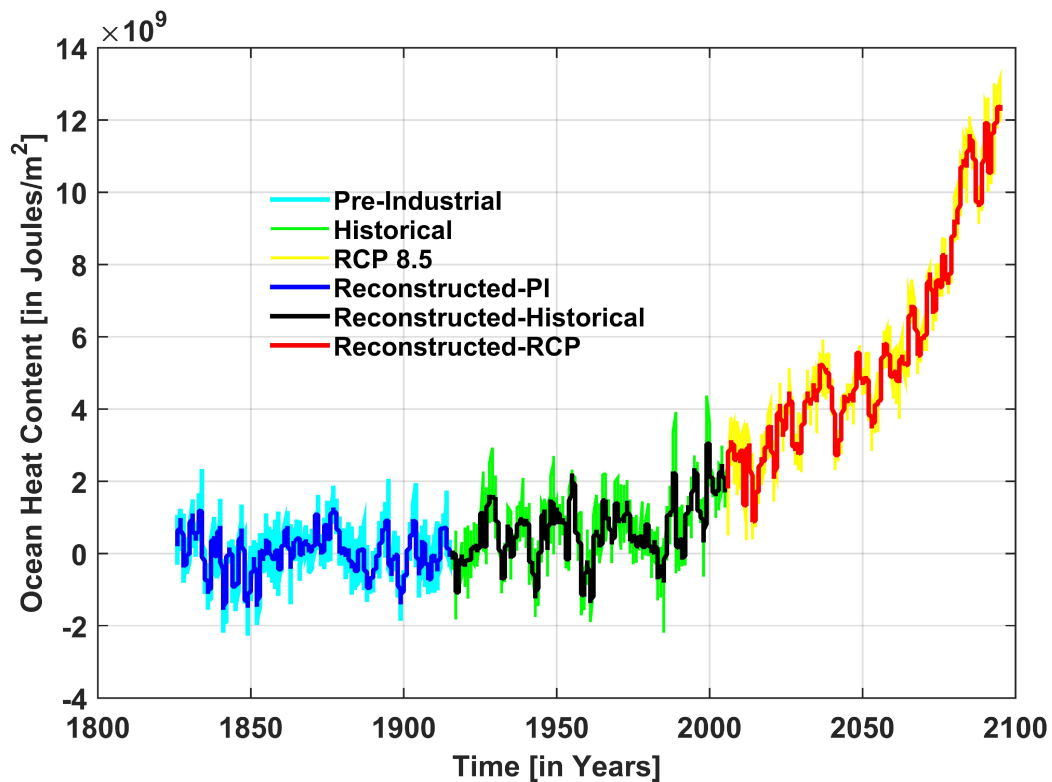
Figure 4.12: Modelled monthly ocean heat content density derived from the HADGEM2-ES model for the Kangerlussuaq Glacier section. The Historical and RCP 8.5 simulation derived OHC are expressed as anomalies with respect to the mean of the Pre-Industrial Values. The Deep Blue, Black and Red colours correspond to the Reconstructed Pre-Industrial, Historical and RCP 8.5 simulations respectively. The Reconstructed Pre-Industrial, Historical and RCP 8.5 signals are obtained from the last 6 Intrinsic Mode Functions (IMFs), labelled from c5-c10 in Figure A.12, A.13 and A.14 respectively.

a)

b)
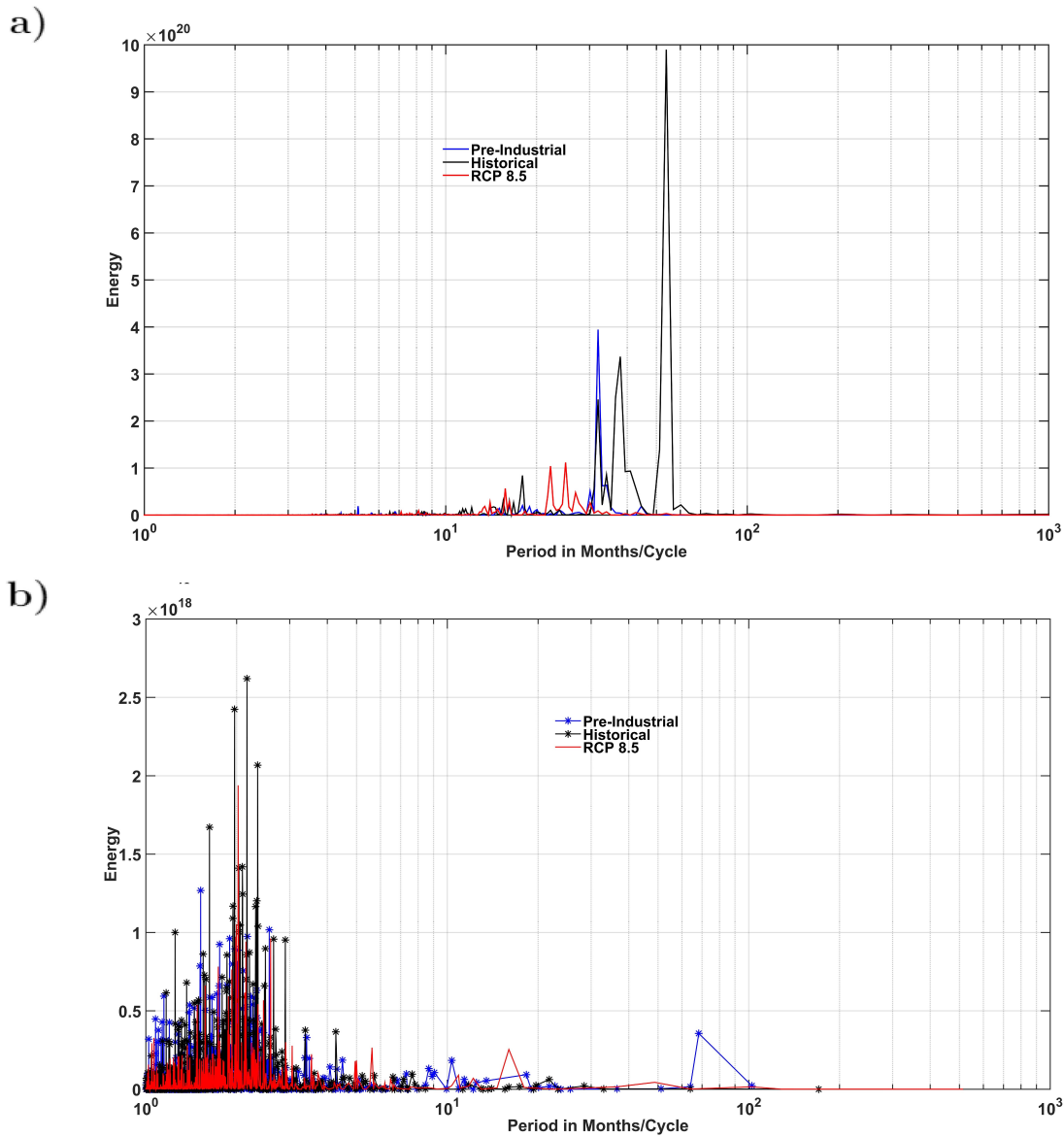
Figure 4.13: Kangerlussuaq Glacier section: Marginal Hilbert Spectrum of Energy (in Joules^2/m^4) versus Period (in Months/Cycle) for the Pre-Industrial (Blue), Historical (Black) and RCP 8.5 (Red) OHC signal derived from the HADGEM2-ES model, using **a)** the low-frequency (c5-c8) modes and **b)** the high-frequency (c1-c4) modes corresponding to each simulation. The low frequency modes (c5-c8) contain the multi-year cycles, whereas, the high-frequency modes (c1-c4) contain the intra-annual cycles.

Below, in Table 4.6, we provide the energy contained in each mode (Refer A.2.2: Kangerlussuaq Glacier) corresponding to each of the three simulations. Furthermore, we express the contribution of each of these modes to the total energy as percentages.

	Kangerlussuaq Glacier					
	Pre-Industrial		Historical		RCP 8.5	
Mode	Energy	% of Total	Energy	% of Total	Energy	% of Total
c1	1.63×10^{19}	0.39	8.20×10^{20}	0.82	1.60×10^{19}	0.017×10^{-2}
c2	2.24×10^{19}	0.54	7.72×10^{17}	0.08×10^{-2}	1.07×10^{18}	0.001×10^{-2}
c3	4.17×10^{19}	1.00	3.51×10^{19}	0.03	1.47×10^{19}	0.015×10^{-2}
c4	3.25×10^{19}	0.78	5.25×10^{19}	0.05	5.08×10^{20}	0.005
c5	8.54×10^{19}	2.04	8.32×10^{19}	0.08	4.60×10^{19}	0.048×10^{-2}
c6	6.72×10^{19}	1.60	2.00×10^{20}	0.20	7.93×10^{19}	0.084×10^{-2}
c7	4.49×10^{20}	10.73	3.47×10^{20}	0.35	6.00×10^{20}	0.006
c8	5.80×10^{20}	13.85	7.72×10^{20}	0.77	4.71×10^{20}	0.005
c9	2.30×10^{21}	54.89	1.00×10^{19}	0.01	6.82×10^{21}	0.072
c10	5.94×10^{20}	14.18	9.81×10^{22}	97.69	9.45×10^{24}	99.910

Table 4.6: For each of the three simulation corresponding to Kangerlussuaq Glacier, the table contains the energy (in Joules^2/m^4) contained in every decomposed Intrinsic Mode Function (IMF). The contribution of each IMF towards the total energy is expressed as percentages.

Interpretation of the results:

At the modelled Helheim Glacier section, the Irminger Current (IC) temperatures show a considerable variability over time [Figure not shown]. As the Ocean Heat Forcing near Helheim is predominantly dependent on the IC component, a greater variability is seen in the OHC signal over time at the Helheim section, as compared to the Kangerlussuaq section (Figure 4.10 and 4.12). Furthermore, at Kangerlussuaq, the subsurface warming is dependent on the return waters of the Arctic Atlantic which are colder compared to the IC component. Thus, the modelled amplitude of the Historical signal is similar to the Pre-Industrial signal. It is only when these Return Atlantic Waters (RAWs) gain in heat and salt (towards the end of the 20th century), that the OHC shows an increasing trend, consistent with our inferences from section 4.2 (Figures 4.8(a) and (b)).

We also infer from Table 4.4 and 4.6, that in a Pre-Industrial scenario, the contribution of the high-frequency modes (c1-c4) to the total energy contained in the signal is relatively higher than the Historical and RCP 8.5 signal. The ocean's response to GHG forcings is manifested as a very dominant, low-frequency, long-term trend. For the Historical and RCP 8.5 simulation, this is captured in mode c10 (Table 4.4 and 4.6), and constitutes (almost) all of the energy contained in the signal. Such a dominant response is seen to overcompensate the energy contribution from the other modes, in particular, the high-frequency (c1-c4) modes. This becomes more evident from the considerable fall in the energy contribution from the high-frequency (c1-c4) modes in the RCP 8.5 simulation.

At Helheim, compared to the Pre-Industrial and Historical scenario, the energy contained in mode c10 for the RCP 8.5 scenario is found to be 2 and 3 orders of magni-

tude greater, respectively (Refer Table 4.4). At Kangerlussuaq, a similar response is seen, however, the RCP 8.5 scenario (mode c10) is found to be 4 orders of magnitude greater than the Pre-Industrial scenario (Refer Table 4.6). Furthermore, the trend over the entire period for the RCP 8.5 scenario is substantially higher at Kangerlussuaq than Helheim (Refer Table 4.3 and 4.5). It can be stated that Kangerlussuaq Glacier is more sensitive to anthropogenic induced ocean heat forcing than Helheim.

Jakobshavn Glacier:

Pre-Industrial simulation:

The Marginal Hilbert Spectrum of the signal reconstructed using the high-frequency modes (c1-c4, Figure A.15) shows that the energy is contained around a 2 month period, similar to our inferences from the East. This energy is considerably higher than the energy contained in the RCP 8.5 signal at these periods (Figure 4.15 (b)). In Table 4.8, modes c1-c4 (Figure A.15) correspond to sub-annual frequencies and contain 2.51% of the total energy content of the Pre-Industrial OHC signal. This is comparatively higher than the Historical (0.001%) and RCP 8.5 simulation (0.00005%).

The Marginal Hilbert Spectrum obtained from the low-frequency modes of the Pre-Industrial simulation (c5-c8, Figure A.15) shows that most of the energy is contained around a multi-year (2 and 3 year) period (Figure 4.15 **a**). This energy is considerably higher than the energy contained in the Historical simulation at any given period.

Historical simulation:

The Marginal Hilbert Spectrum of the low-frequency modes (c5-c8, Figure A.16) shows that the energy is contained around a multi-year (3 year) period. The energy at these periods, however, is not comparable to the Pre-Industrial and RCP 8.5 signal (Figure 4.15 **a**). Some energy is also contained in a 6 year cycle, which is not seen for the Pre-Industrial and RCP 8.5 signal.

A dominant increasing trend is seen in the last two decades of the 20th century (A.D. 1985-2005) (Figure 4.14, Table 4.7). This is comparatively lower than our inferences at Kangerlussuaq; and furthermore, an order of magnitude lower than Helheim.

The energy corresponding to the high-frequency modes (c1-c4, Figure A.16) is contained around a 2 month period, and, is considerably higher than the Pre-Industrial and RCP 8.5 signal (Figure 4.15 **b**), similar to our inferences from the East.

RCP 8.5 simulation:

The Marginal Hilbert Spectrum of the low-frequency modes (c5-c8, Figure A.17) shows the presence of multi-year (2 and 3 year) cycles (Figure 4.15 **a**), whose energies are comparable to the Pre-Industrial signal, and considerably greater than the Historical signal.

The signal reconstructed from the high-frequency modes (c1-c4, Figure A.17) shows that most of the energy is contained around a 2 month period (Figure 4.15 **(b)**), consistent with our inference from the Eastern Margin. The energy contained at these periods are relatively lower than the Pre-Industrial period.

A strong increasing trend can be discerned in the modelled OHC amplitude during the beginning of the simulation (A.D. 2006), which continues for ~ 45 years until A.D. 2050 (Figure 4.14, Table 4.7).

Unlike our inferences from the Eastern Margin, where a consistent, low-frequency, long-term increasing trend was seen towards the end of the century (A.D. 2055-2095) (Figure 4.10 and 4.12), the modelled OHC shows a small decreasing trend (A.D. 2051-2065), after which it remains fairly stagnant. This is supposedly driven by a declining sea-ice concentration at Nares Strait, which allows for a relatively greater mixing of cold Arctic waters of the Lincoln Sea and the Baffin Bay (Refer Appendix: Figure A.18).

Simulation	Time-Period	Trend [in $\mathbf{J/m^2/month}$)
Historical	1916-2005	1.38×10^7
Historical	1985-2005	4.51×10^7
RCP 8.5	2006-2095	1.27×10^7
RCP 8.5	2006-2050	6.26×10^7
RCP 8.5	2051-2065	-8.75×10^7

Table 4.7: The modelled upper-ocean heat content trend for the Historical and the RCP 8.5 simulations expressed in Joules/m^2/month for the Jakobshavn Glacier. The Historical and the RCP 8.5 simulation derived OHC density are presented as anomalies with respect to the mean of the Pre-Industrial climate.

Interpretation of the results:
Following our inference from the Eastern Margin, we find a similar dominant, low-frequency, long-term trend as a response to GHG forcings at Jakobshavn (Mode c10, Table 4.8). More importantly, the response seen for the Historical simulation (Mode c10, Table 4.8) is comparable to the RCP 8.5 simulation, unlike our inferences from the East. It can be argued that for Jakobshavn, the entire energy of the OHC signal is stored in this mode. Following this response, we see that the energy contribution from the high-frequency modes (c1-c4) is overcompensated by the energy contained in mode c10. Furthermore, this compensation is substantially greater than our inferences from the Eastern Margin.

Furthermore, for the RCP 8.5 scenario, it can be inferred from Figure 4.14, that the OHC does not have a consistent long-term increasing trend for the late half of the 21st century (A.D. 2055-2095). During the Pre-Industrial and Historical scenario, a time-series of the average sea-ice concentration across the strait shows that the strait was covered with considerable sea-ice throughout the year, for the entire period (Figure A.18 **(a)**, **(b)**). It can be argued that this could inhibit the inflow of cold Arctic waters of the Lincoln Sea in to the Baffin Bay. Thus, an additional warming induced by the GHGs in Historical scenario is seen to cause a rise in the subsurface temperatures, particularly towards the end of the 20th century (Figure A.18 **(b)**). While a similar rise in (subsurface) temperatures would be expected under a future warming scenario, this does not hold true. For the RCP 8.5 scenario, we notice that towards the later part of the simulation (A.D. 2050 onwards), there are several months during the year that remain completely free of sea-ice (Figure A.18 **(c)**), allowing for a relatively enhanced mixing of the Arctic origin waters with the waters lying south of the strait. This is concordant with a sudden stagnation seen in a rising subsurface temperature in the RCP 8.5 scenario (A.D. 2050 onwards) (Figure A.18**(c)**).
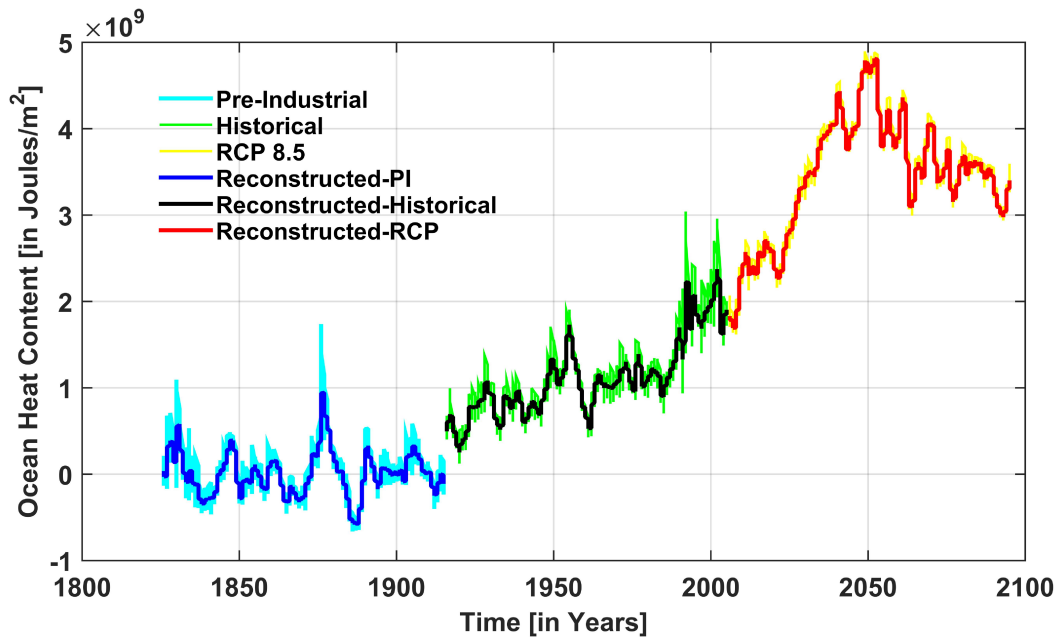
Figure 4.14: Modelled monthly ocean heat content density derived from the GISS-E2-R model for the Jakobshavn Glacier section. The Historical and RCP 8.5 simulation derived OHC are expressed as anomalies with respect to the mean of the Pre-Industrial Values. The Deep Blue, Black and Red colours correspond to the Reconstructed Pre-Industrial, Historical and RCP 8.5 simulations respectively. The Reconstructed Pre-Industrial is obtained from the last 7 IMFs, labelled from c5-c11 in Figure A.15. The Reconstructed Historical and RCP 8.5 signals are obtained from the last 6 Intrinsic Mode Functions (IMFs), labelled from c5-c10 in Figure A.16 and A.17 respectively.
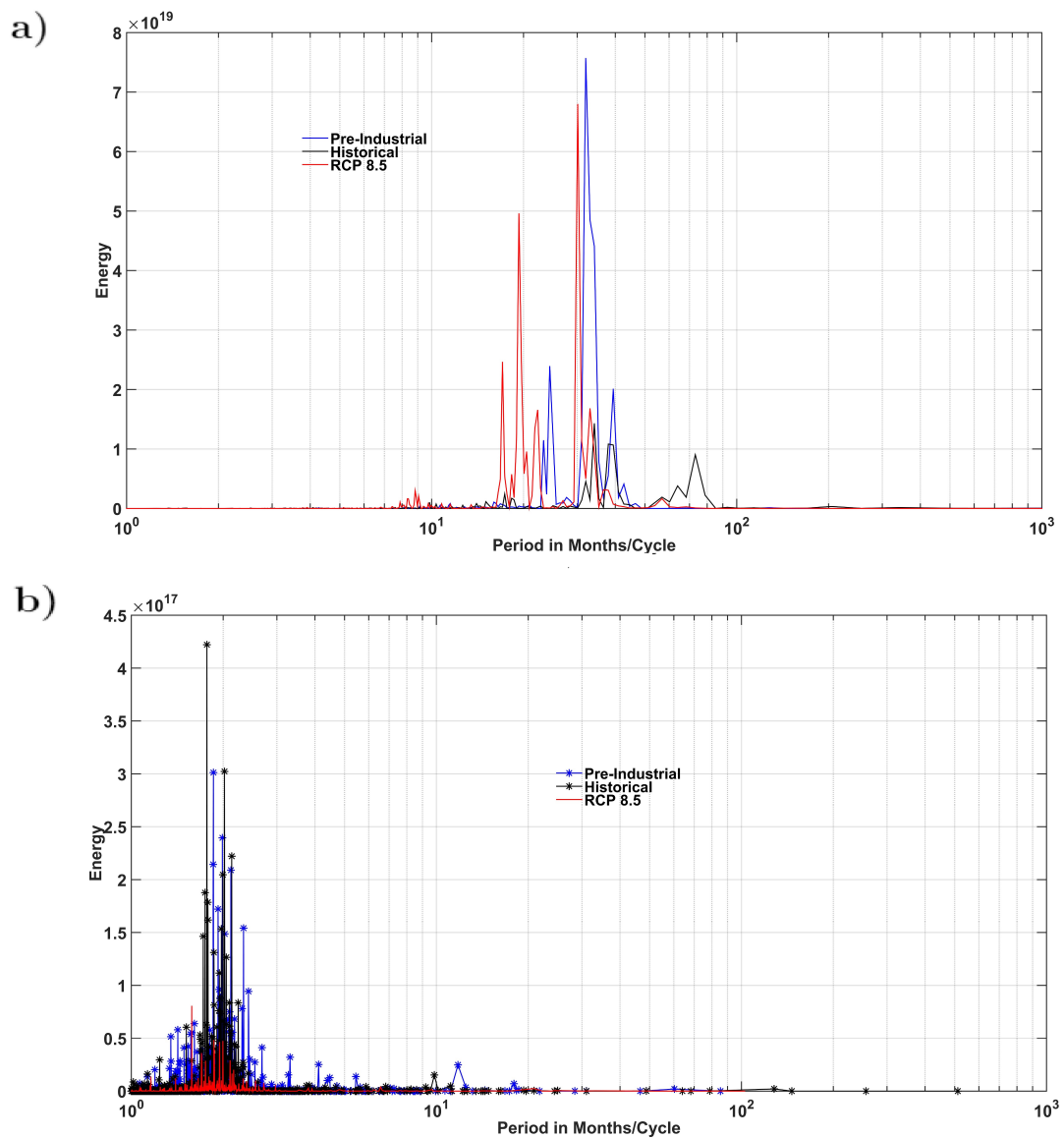
Figure 4.15: Jakobshavn Glacier section: Marginal Hilbert Spectrum of Energy (in Joules^2/m^4) versus Period (in Months/Cycle) for the Pre-Industrial (Blue), Historical (Black) and RCP 8.5 (Red) OHC signal derived from the HADGEM2-ES model, using **a)** the low-frequency (c5-c8) modes and **b)** the high-frequency modes (c1-c4) corresponding to each simulation. The low frequency modes (c5-c8) contain the multi-year cycles, whereas, the high-frequency modes (c1-c4) contain the intra-annual cycles.

Below, in Table 4.8, we provide the energy contained in each mode (Refer A.2.2: Jakobshavn Glacier) correspond to each of the three simulations. Furthermore, we express the contribution of each of these modes to the total energy as percentages.

	Jakobshavn Glacier					
	Pre-Industrial		Historical		RCP 8.5	
Mode	Energy	% of Total	Energy	% of Total	Energy	% of Total
c1	5.25×10^{17}	0.13	2.11×10^{17}	0.317×10^{-4}	1.24×10^{17}	0.024×10^{-4}
c2	7.98×10^{16}	0.02	2.10×10^{16}	0.032×10^{-4}	3.20×10^{16}	0.006×10^{-4}
c3	4.92×10^{18}	1.21	2.20×10^{18}	3.310×10^{-4}	4.10×10^{17}	0.078×10^{-4}
c4	4.67×10^{18}	1.15	7.06×10^{18}	0.001	2.38×10^{18}	0.452×10^{-4}
c5	4.42×10^{18}	1.09	3.19×10^{18}	4.783×10^{-4}	6.21×10^{18}	1.182×10^{-4}
c6	8.88×10^{18}	2.19	8.60×10^{18}	0.001	2.63×10^{19}	5.006×10^{-4}
c7	1.41×10^{20}	34.85	1.78×10^{19}	0.003	2.12×10^{20}	0.004
c8	1.58×10^{20}	38.92	1.55×10^{20}	0.023	1.28×10^{20}	0.002
c9	5.50×10^{19}	13.53	1.32×10^{20}	0.020	3.36×10^{22}	0.639
c10	1.53×10^{19}	3.78	6.65×10^{23}	99.951	5.22×10^{24}	99.354
c11	1.27×10^{19}	3.14	N/A	N/A	N/A	N/A

Table 4.8: For each of the three simulation corresponding to Jakobshavn Glacier, the table contains the energy (in Joules^2/m^4) contained in every decomposed Intrinsic Mode Function (IMF). The contribution of each IMF towards the total energy is expressed as percentages. For the Historical and RCP 8.5 simulation, there are only 10 IMFs, and therefore, N/A denotes Not Applicable.

5

Conclusion

In this chapter, we answer the research objectives discussed in Chapter 1, and thereafter, provide recommendations for future research work.

5.1 Model Evaluation

The first research question stated: ***How reliable are the Global Circulation Models in simulating the Ocean Heat Forcing to the GrIS?***. We answered this question in Chapter 4 (Refer 4.1), using Methods discussed in Chapter 3 (Refer 3.3).

5.1.1 Conclusion

In this project, the modelled tracer fields of Temperature and Salinity were evaluated against regridded high resolution CTD observations of the same parameters. We inferred from our analysis that not all the GCMs are suitable for analysing the ocean heat forcing around Greenland. More importantly, we noticed that there is a relevant inter-model spatial discrepancy. To that extent, the GISS E2-R model fails to capture the water mass signatures towards the Eastern Greenland Margin, but at the same time, it's representation of the spatial distribution of the Irminger Mode Waters (IMWs) is more reliable than the HADGEM2-ES model, towards the West.

For the modelled tracer fields to reciprocate the observations towards the Eastern Greenland Margin, it needs to accurately resolve the vertical mixing of tracers. The Helheim section lies south of the Denmark Strait. The sensitivity of the modelled tracer fields along the section, is therefore, dependent on the modelled volume transport of the overflowing waters from the Arctic across the Strait, and how it facilitates the mixing of these water masses with the Irminger Current, and the subsequent Deep Water formation. Similarly, the Kangerlussuaq section lies north of the Denmark Strait, where a subsurface Irminger Current, flowing from the south, mixes with the colder and more saline Return Atlantic Waters (RAWs), on the Greenland shelf. Thus, with deep convection sites and regions of enhanced vertical mixing, the potential temperature along the Eastern Greenland Margin shows greater variability (Refer Chapter 4, section 4.3), than the West. Therefore, it can be argued that the HADGEM2-ES model is able to characterise these processes better than the GISS-E2-R model.

At the Jakobshavn section, the GISS-E2-R model accurately represents the spatial distribution and (T-S) characterisation of the IMWs, whereas, in the HADGEM2-ES model, the IMWs are found to remain offshore and are not seen to climb on to the Greenland shelf. Furthermore, our results show that the HADGEM2-ES modelled surface current component of the West Greenland Current (WGC) is comparatively colder and fresher than the observations. The GISS-E2-R model, on the other hand, accurately represents the surface current (T-S) properties. It can be argued that a cold and fresh surface current component favours sea-ice formation and growth in the HADGEM2-ES model, which in turn, helps the surface waters to retain their relatively cold and thick profile. In comparison, a warmer and relatively more saline surface layer in the GISS-E2-R model is seen to limit sea-ice formation. This, in conjunction with a greater intrusion of the AWs within the surface layer weakens the stratification, further inhibiting sea-ice growth. Over seasonally competing processes, a lower sea-ice concentration (SIC) would allow the surface waters to take up more heat (SW↓) during summer, compensated in part, by the heat loss from the upwelling longwave radiation (LW↑).

It is, therefore, highly recommended, to draw comparisons with the observed tracer properties, before performing a similar study using modelled results from a GCM.

5.2 Changes in variability of the Ocean Heat Forcing

The second research objective stated: ***What is the spatial distribution of the different water masses along our study regions and how does the subsurface (AW) warming evolve under anthropogenic GHG forcings?***
In this section, we will also answer the third research objective, which stated: ***At multi-year/decadal timescales, what is the natural variability of the Ocean Heat Content around our study locations and how does it evolve under anthropogenic forcing?*** Both these questions have been answered in Chapter 4 (Refer 4.2), using methods discussed in Chapter 3 (Refer 3.4).

5.2.1 Conclusion

The modelled climatological anomaly (with respect to the Pre-Industrial climate) for the Historical and RCP 8.5 subsurface temperature fields along the Greenland shelf, shows warming across all three of our study locations. However, based on our results, we argue that the Kangerlussuaq region is more sensitive than Helheim and Jakobshavn glacier to GHG forcings. Furthermore, the subsurface warming manifests itself differently, at each of our study location. We demonstrate that the subsurface warming at the Helheim Glacier (shelf) is predominantly dependent on the heat advection from the Irminger Current (IC). In comparison to the IC occupying the Helheim Glacier (shelf), the subsurface component of the East Greenland

Current (EGC), that arrives after it overflows the shallow sill, is only a small fraction. Being more dense than the waters found South of the Denmark Strait, they sink below the subsurface IC and usually correspond to the DWs. At Kangerlussuaq, only a small fraction of the Irminger Current component is able to climb on to the shallow shelf as it moves Northward. The much higher modelled subsurface temperature anomaly, is therefore explained by the enhanced warming of the Return Atlantic Waters (RAWs) in response to anthropogenic GHG forcing. Towards the West, the Jakobshavn glacier is fed by the Irminger and Northern Atlantic Mode Waters (IMWs and NAMWs). These are the subsurface current extensions of the East Greenland Current. A warming of the Irminger Current could possibly translate to a warmer IMW or NAMW.

Our hypothesis is further validated during our investigation of the temporal variability in the modelled Ocean Heat Content. For Kangerlussuaq, the Historical OHC amplitude resembles the Pre-Industrial signal. However, a warming of the RAWs in response to the GHG forcing is consistent with a long-term increasing trend in the modelled OHC, beginning from the end of the Historical simulation in 20th century (A.D. 1985) till the end of our RCP 8.5 simulation (A.D. 2095). This (RCP 8.5) trend is an order of magnitude higher than our results from other locations.

For each of the three locations, we see that there is a considerable contribution from the high-frequency intrinsic modes (c1-c4) to the total energy contained in the OHC signal in a Pre-Industrial scenario. The response of the ocean to GHG forcings is manifested as a very dominant, low-frequency, long-term trend, which constitutes for (almost) all of the energy contained in the signal. This dominant response is further seen to overcompensate the contribution from the high-frequency modes in these scenarios. Furthermore, for the RCP 8.5 scenario, we infer that at Kangerlussuaq, such a response (mode c10) is considerably greater than other locations. Our results also indicate that sea-ice free months at the Nares Strait (A.D. 2055 onwards) allows for a relatively greater mixing of the cold Arctic Waters of the Lincoln Sea and the Baffin Bay. This is found to be consistent with the stagnation seen in the rising upper ocean heat content at Jakobshavn.

5.3 Research Project Status:

We conclude our research report by discussing whether the study was able to achieve the primary objective or not. This is followed by recommendations for possible research in the future.

5.3.1 Evaluation: Primary Objective

After summarizing the research objectives in detail, we evaluate the research project status by analysing the primary objective, as discussed in Chapter 1 (Refer section 1.4). The objective stated: ***Can GCMs be used to bridge the data gaps and put the hydrographic observations into perspective? Can they be used***

for making reliable projections of subsurface ocean heat forcing?

In our study, the selection of GCMs for each location was formulated based on a comprehensive evaluation scheme. Owing to a considerable discrepancy seen between the modelled and observed tracer characterisation along both the margins, we believe that in order to perform a similar study, evaluation of the GCMs is necessary before using the output. Concerning our analysis of the spatio-temporal variability of ocean heat forcing around our glacier locations, we argue that as the subsurface (AW) properties agree well with the observational records, the simulated spatio-temporal distribution of the AWs, and the variability in the ($\sim$50-500 meter) Ocean Heat Content are well grounded. However, reliable projections need to be bound by uncertainties. An underlining caveat in our study is that we only have one model to address the response of the ocean at each location.

5.3.2 Recommendations for further research

We propose the following setup for further research in line with our study:

1. Set up the research by evaluating a series of GCMs around the study region. The models should be able to satisfy the observed subsurface T-S characteristics. The GCMs which qualify the evaluation can be used to set up an ensemble. The nature of this ensemble would be based on the objective of the research. If the main objective of the research involves drawing (spatial) comparisons between locations along both the margins, it is necessary that the ensemble should have the same set of GCMs. If the investigation is spatially local, separate ensembles can be generated for each study location.

2. We recommend the addition of two more parameters for the model evaluation phase, namely precipitation and sea-ice concentration. These can be used to improve our understanding of the modelled surface water characteristics.

3. It is known that both radiative and latent heat fluxes show significant seasonal variation in the arctic. Therefore, studies along the air-ocean-ice interaction domain is needed to understand the seasonal and temporal variations in the energy balance, water-mass characteristics, and how they regulate the forcing needed to establish sea-ice cover.

4. Utilise the generated ensemble of GCMs for investigating the research questions (Refer Methodology: Subsection 3.4), and use the ensemble average instead of relying on output from a single model. The results would now be more coherent, and the projections could now be bound by uncertainties.

5. During our research, numerous hydrographic sections had to be modelled, in order to understand the network of current pathways. The use of current velocity (vector) fields, along with the T-S sections, is a better indicator of flow. This would, therefore, help in tracing the currents and subsequently improve

our understanding of the motion of subsurface water masses.

6. The volume of water overflowing the Denmark Strait is an important variable field, as these waters transform the tracer properties found south of the strait. Therefore, it could be useful during both the model evaluation and analysis phase of the assessment.

7. An aspect not covered during our study is the effect of seasonality in the ocean heat forcing and the parameters that influence it. The presence of a (strong) seasonal cycle could greatly modify the response of submarine melting towards ocean heat forcing. For instance, regions with pronounced (subsurface) warming for most/greater parts of the year would be more sensitive to submarine melt than other regions.

8. The relatively greater (high-frequency) variability seen in the modelled Ocean Heat Content along the Helheim Glacier section, might in part, be a result of the deepened MLD towards the East in the Irminger Sea basin (when compared to the West). It would be useful to investigate the seasonal/inter-annual variability in the modelled mixed layer and the thermocline along both the eastern and western margins, for a more robust understanding of the AW variability and its subsequent effect on Ocean Heat Forcing.

Bibliography

[1] Location of Greenland *https://en.wikipedia.org/wiki/Greenland*

[2] Morlighem,M., Ice Sheet Modelling Group, Mass Conservation Dataset *http://sites.uci.edu/morlighem/dataproducts/bedmachine-greenland/*

[3] Potter,S., Cabbage, M., McCarthy, L. 2016 *NASA, NOAA Data Show 2016 Warmest Year on Record Globally.*

[4] Luthcke, Scott B.; Sabaka, T.J.; Loomis, B.D.; Arendt, A.A.; McCarthy, J.J.; Camp, J. Journal of Glaciology, Volume 59, Number 216, August 2013, pp. 613-631(19). *Antarctica, Greenland and Gulf of Alaska land-ice evolution from an iterated GRACE global mascon solution*

[5] Hua, Aixue, Meehla, Gerald A., Hanb, Weiqing, & Yinc, Jianjun. 2011. Deep Sea Research Part II: Topical Studies in Oceanography, 58(September), 1914–1926. *Effect of the potential melting of the Greenland Ice Sheet on the Meridional Overturning Circulation and global climate in the future*

[6] Straneo, F.; Heimbach, P. 2013. Nature 504, 36–43, doi:10.1038/nature12854. *North Atlantic warming and the retreat of Greenland's outlet glaciers*

[7] Nick, Faezeh M.; Vieli, A.; Andersen M.L.; Joughin, I; Payne, A; Edwards, T.L.; Pattyn, F; van de Wal, Roderik S.W. 2013. Nature 497, 235–238, doi:10.1038/nature12068. *Future sea-level rise from Greenland's main outlet glaciers in a warming climate*

[8] Holland, D. M.; Thomas, R.H.; De Young, B.; Ribergaard, M.H.; Lyberth, B. 2008, Nature Geoscience, 1(10), 659-664, doi:10.1038/Ngeo316 *Acceleration of Jakobshavn Isbrae triggered by warm subsurface ocean waters*

[9] Joughin, I.; Alley, R.B.; Holland, D.M. 2012,Science, 338 (6111), 1172-1176, doi: 10.1126/Science.1226481. *Ice-Sheet Response to Oceanic Forcing*

[10] Andresen, Camilla S.; Straneo, F.; Ribergaard, M.H.; Bjørk,A.A.; Andersen,Thorbjørn J; Kuijpers,A.; Nørgaard-Pedersen,N.; Kjær,Kurt H.; Schjøth,F.; Weckström,K.; Ahlstrøm, Andreas P. 2012, Nature Geoscience 5, 37–41, doi:10.1038/ngeo1349. *Rapid response of Helheim Glacier in Greenland*

to climate variability over the past century

[11] Rignot, E.; Koppes,M.; Velicogna, I. 2010, Nature Geoscience 3, 187–191, doi:10.1038/ngeo765 *Rapid Submarine melting of the calving faces of West Greenland Glaciers*

[12] Straneo, F.; Hamilton, G.; Sutherland, D.A.; Stearns, L.A. 2009, Woods Hole Oceanographic Institution. *Did changes in the Subpolar North Atlantic trigger the recent mass loss from the Greenland Ice Sheet?*

[13] Klinck, J. M.; O'Brien, J.J.; Svendsen, H. 1981, J. Phys. Ocean. 11, 1612-1626. *A simple model of Fjord and coastal circulation interaction*

[14] Stigebrandt, A. 1990, Tellus 42A 605-614. *On the response of the horizontal mean vertical density distribution in a fjord to low-frequency density fluctuations in the coastal water*

[15] Sutherland,D.A.; Pickart,R.S. 2008, Prog. Oceanogr. 78, 58-77. *The East Greenland Coastal Current: Structure, variability, and forcing*

[16] Hanna, E. et al. 2009, Hydrol. Process. 23, 7-30. *Hydrologic Response of the Greenland ice sheet: the role of oceanographic warming*

[17] Hátún, H., Sandø, A.B., Drange, H., Hansen, B. and Valdimarsson, H. 2005. Science 309, 1841–1844. *Influence of the Atlantic subpolar gyre on the thermohaline circulation.*

[18] Myers,P.G.; Kulan, N.; Ribergaard, M.H. 2007, Geophysical Research Letters 34, L17601 doi:10.1029/2007GL030419. *Irminger Water variability in the West Greenland Current*

[19] Yashayaev, I. 2007, Prog. Oceanogr., 73, 242-276. *Hydrographic changes in the Labrador Sea, 1960-2005*

[20] Häkkinen, S.; Rhines, P.B. 2004, Science 304, 555-559. *Decline of Subpolar North Atlantic Circulation during the 1990s*

[21] Häkkinen, S.; Rhines, P. B.; Worthen, D. L. 2011, Science 334, 655–659. *Atmospheric blocking and Atlantic multidecadal ocean variability*

[22] Williams, R.G., Roussenov, V., Smith, D. and Lozier, S. 2013. J. Clim. http://dx.doi.org/10.1175/JCLI-D-12-00234.1. *Decadal evolution of ocean thermal anomalies 1 in the North Atlantic: the effect of Ekman, overturning and horizontal transport.*

[23] Lozier, M.S.; Leadbetter, S.; Williams, R.G.; Roussenov, V.; Reed, M.S.C.;Moore, N.J. 2008, Science, 309, 800-803. *The spatial pattern and*

mechanisms of heat-content change in the North Atlantic

[24] Visbeck, M.; E. Chassignet; R.Curry; T.Delworth; R.Dickson; and G.Krahmann. 2003. (J. Hurrell; Y. Kushnir; G. Ottersen; M.Visbeck; eds.) AGU, Washington,D.C. pp 113-146. *The Ocean's Response to North Atlantic Oscillation Variability, in The North Atlantic Oscillation: Climatic Significance and Environmental Impact*

[25] Polyakov, I.V. et al. 2005, J. Clim. 18, 4562–4581. *Multidecadal variability of North Atlantic temperature and salinity during the twentieth century*

[26] Reverdin, G. 2010, J.Clim. 23, 4571–4584. *North Atlantic subpolar gyre surface variability (1895–2009)*

[27] Trenberth, K.E.; Shea, D.J. 2006, Geophysical Research Letters 33, L12704. *Atlantic hurricanes and natural variability in 2005*

[28] Levitus, S. et al. 2012, Geophysical Research Letters 39, L10603. *World ocean heat content and thermosteric sea level change (0–2000 m), 1955–2010*

[29] Johannessen, O.M., Korablev, A., Miles, V. et al. 2011, Surv. Geophys. 32:387. doi:10.1007/s10712-011-9130-6. *Interaction Between the Warm Subsurface Atlantic Water in the Sermilik Fjord and Helheim Glacier in Southeast Greenland*

[30] Danish Meteorological Institute Centre for Ocean and Ice, Copenhagen, Denmark, May 2013. *Oceanographic Investigations off West Greenland 2012*

[31] J.Alean, M.Hambrey, Glaciers Online. *http://www.swisseduc.ch/glaciers/arctic-islands/arctic-04-en.html*

[32] Shepherd, A. et al. 2012. Science 338, 1183–1189 (2012). *A reconciled estimate of ice-sheet mass balance.*

[33] Hanna, E. et al. 2013. Nature 498, 51–59 *Ice-sheet mass balance and climate change.*

[34] van den Broeke, M. et al. 2009. Science 326, 984–986 (2009). *Partitioning recent Greenland mass loss.*

[35] Krabill, W. 2004. Geophys. Res. Lett. 31, L24402. *Greenland Ice Sheet: increased coastal thinning.*

[36] Sole, A., Payne, T., Bamber, J. et al. 2008. The Cryosphere, 2 (2). 205-218. ISSN 1994-0416 *Testing hypotheses of the cause of peripheral thinning of the Greenland Ice Sheet: is land-terminating ice thinning at anomalously high rates?*

[37] Hanna, E. et al. 2011. J. Geophys. Res. 116, D24121. *Greenland ice sheet surface mass balance 1870 to 2010 based on Twentieth century reanalysis, and links with global climate forcing.*

[38] Moon, T., Joughin, I., Smith, B. and Howat, I. 2012. Science 336, 576–578. *21st-century evolution of Greenland outlet glacier velocities.*

[39] Hall, D. K. et al. 2013. Geophys. Res. Lett. 40, 2114–2120. *Variability in the surface temperature and melt extent of the Greenland ice sheet from MODIS.*

[40] Donald Slater October 28, 2016. Submarine Melt, EGU Blog. *http://blogs.egu.eu/divisions/cr/tag/submarine-melt/*

[41] I. Joughin et al. 2008. J. Geophys. Res. 113, F04006.

[42] J.M. Amundson et al. 2010. J. Geophys. Res. 115, F01005.

[43] R. J. Motyka et al. 2011. J. Geophys. Res. 116, F01007.

[44] Jenkins, A. 2011. J. Phys. Oceanogr. 41, 2279–2294. *Convection-driven melting near the grounding lines of ice shelves and tidewater glaciers.*

[45] Sciascia, R., Straneo, F., Cenedese, C. and Heimbach, P. J. Geophys. Res. 118, 2492–2506. *Seasonal variability of submarine melt rate and circulation in an East Greenland fjord.*

[46] Pritchard, H.D., Arthern, R.J., Vaughan, D.G. and Edwards, L.A. 2009. Nature 461, 971–975. *Extensive dynamic thinning on the margins of the Greenland and Antarctic ice sheets*

[47] Våge,K. et al. 2011. Deep Sea Res. Part I 58, 590–614. *The Irminger Gyre: Circulation, convection, and interannual variability.*

[48] Bersch, M., Yashayaev, I. and Koltermann, K.P. 2007. Ocean Dyn. 57, 223–235. *Recent changes of the thermohaline circulation in the subpolar North Atlantic.*

[49] Häkkinen, S., Rhines, P.B. and Worthen, D. L. 2013, Journal of Geophysical Research, Oceans 118, 3670-3678. *Northern North Atlantic sea surface height and ocean heat content variability*

[50] Hurrell, J.W. 1995, Science 269, 676-679. *Decadal trends in the North Atlantic oscillation: regional temperatures and precipitation*

[51] Enfield, D.B., Mestas-Nunez, A.M. and Trimble, P.J. 2001. Journal of Geophysical Research Letters 28, 2077-2080. *The Atlantic multidecadal oscillation*

and its relationship to rainfall and river flows in the continental U.S.

[52] Zweng, M.M. and Münchow, A. 2006. J.Geophys. Res. 111, C07016. *Warming and freshening of Baffin Bay, 1916–2003.*

[53] Christoffersen, P. et al. 2011. Cryosphere 5, 701–714. *Warming of waters in an East Greenland fjord prior to glacier retreat: mechanisms and connection to large-scale atmospheric conditions.*

[54] Straneo, F. et al. 2010. Nature Geosciences 3, 182-186. *Rapid circulation of warm subtropical waters in a major glacial fjord in East Greenland.*

[55] Johnson, H.L., Münchow, A., Falkner, K.K. and Melling, H. 2011. J. Geophys. Res. 116, C01003. *Ocean circulation and properties in Petermann Fjord, Greenland.*

[56] Straneo, F. et al. 2012. Ann. Glaciol. 53, 202–210. *Characteristics of ocean waters reaching Greenland's glaciers.*

[57] Sutherland, D.A. et al. 2013. J. Geophys. Res. Oceans 118, 847–855. *Atlantic water variability on the Southeast Greenland continental shelf and its relationship to SST and bathymetry.*

[58] Sutherland, D.A. and Straneo, F. 2012. Ann. Glaciol. 53, 50–58. *Estimating ocean heat transports and submarine melt rates in Sermilik Fjord, Greenland, using lowered acoustic Doppler current profiler (LADCP) velocity profiles.*

[59] Mortensen, J. et al. 2013. J. Geophys. Res. Oceans 118, 1382–1395. *On the seasonal freshwater stratification in the proximity of fast-flowing tidewater outlet glaciers in a sub-Arctic sill fjord.*

[60] Mortensen, J., Lennert, K., Bendtsen, J. and Rysgaard, S. 2011. J. Geophys. Res. 116, C01013. *Heat sources for glacial melt in a sub-Arctic fjord (Godthåbsfjord) in contact with the Greenland Ice Sheet.*

[61] Krauss, W., 1995. Journal of Geophysical Research, 100, 10851-10871. *Mixing in the Irminger Sea and in the Iceland Basin.*

[62] Hopkins, T.S., 1991. *The GIN Sea - A synthesis of its physical oceanography and literature review 1972-1985.*

[63] Aagaard, K. and L.K. Coachman. 1968a. Arctic, 21, 181-200. *The East Greenland Current north of Denmark Strait, Part I*

[64] Aagaard, K. and L.K. Coachman. 1968b. Arctic, 21, 267-290. *The East Greenland Current north of Denmark Strait, Part II*

[65] Aagard,K., J.H.Swift and E.C.Carmack. 1985. Journal of Geophysical Research, 90, 4833-4846. *Thermohaline circulation in the arctic Mediterranean seas*

[66] Hansen, B., Osterhus, S., 2000. Prog. Oceanogr. 45, 109–208. *North Atlantic-Nordic seas exchanges.*

[67] Hansen, B., Osterhus, S., 2007. Prog. Oceanogr. 75 (4), 817–856. *Faroe Bank channel overflow 1995–2005.*

[68] Ross, C.K., 1984. Rapp. P.V. Reun. Cons. Int. Explor. Mer. 185, 111–119. *Temperature-salinity characteristics of the "overflow" water in Denmark Strait during "Overflow '73".*

[69] Girton, J.B., Sanford, T.B., Kase, R.H., 2001. Geophys. Res. Lett. 28, 1619–1622. *Synoptic sections of the Denmark Strait Overflow.*

[70] Macrander, A., Send, U., Valdimarsson, H., Jonsson, S., Kase, R.H., 2005. Geophys. Res. Lett. 32, http://dx.doi.org/10.1029/2004GL021463, L06606. *Interannual changes in the overflow from the Nordic Seas into the Atlantic Ocean through Denmark Strait.*

[71] Jochumsen, K., Quadfasel, D., Valsimarsson, H., Jonsson, S., 2012. J. Geophys. Res. 117. http://dx.doi.org/10.1029/2012JC008244. *Variability of the Denmark Strait Overflow: moored time series from 1996– 2011.*

[72] Dickson, R.R., Brown, J., 1994. J. Geophys. Res. C 99, 12319–12341. *The production of North Atlantic deep water: sources, rates and pathways.*

[73] Mauritzen, C., Price, J., Sanford, T., Torres, D., 2005. Deep Sea Res. Part I 52, 883–913. *Circulation and mixing in the Faroese Channels.*

[74] Saunders, P.M., 1994. J. Geophys. Res. 99, 12343–12355. *The flux of overflow water through the Charlie-Gibbs fracture zone.*

[75] Bower, A.S., Le Cann, B., Rossby, T., Zenk, W., Gould, J., Speer, K., Richardson, P.L., Prater, M.D., Zhang, H.M., 2002. Nature 419 (6907), 603–607. *Directly measured mid-depth circulation in the northeastern North Atlantic Ocean.*

[76] Schott, F., Stramma, L., Fischer, J., 1999. Geophys. Res. Lett. 26, 369–372. *Interaction of the North Atlantic Current with the deep Charlie Gibbs Fracture*

Zone throughflow.

[77] Fleischmann, U., Hildebrandt, H., Putzka, A., Bayer, R., 2001. Deep Sea Res. Part I 48, 1793–1819. *Transport of newly ventilated deep water from the Iceland Basin to the West-European Basin.*

[78] Rudels, B., Anderson, L., Eriksson, P., Fahrbach, E., Jakobsson, M., Jones, E.P., Melling, H., Prinsenberg, S., Schauer, U., Yao, T., 2012a. Arctic Clim. Change 43, 117–198. *Observations in the ocean.*

[79] *http://www.hafro.is/indexeng.php*

[80] Irminger Sea: Where the Arctic Meets the Atlantic. *http://www.whoi.edu/page.dopid=27957*

[81] Jan Mayen Microcontinent. *https://en.wikipedia.org/wiki/JanMayenMicrocontinent*

[82] Rhein, M., D. Kieke, S. Hüttl-Kabus, D. Kieke, S. Hüttl-Kabus, A. Roessler, C. Mertens, R. Meissner, B. Klein, C. W. Böning, and I. Yashayaev (2011). Deep-Sea Res. II, 58(17-18), 1819-1832. *Deep-water formation, the subpolar gyre, and the meridional overturning circulation in the subpolar North Atlantic.*

[83] Copyright: E. Paul Oberlander. Woods Hole Oceanographic Institution. *Refining the model, for a more reliable forecast of climate change, 10 March, 2011.*

[84] Pickart R.S., D.J. Torres, R.A. Clarke, 2001. Journal of Physical Oceanography. In press. *Hydrography of the Labrador Sea during active convection*

[85] Prater, M.D., 2000. Jour. of Phys. Oceanography. *Eddies in the Labrador Sea as observed by profiling RAFOS floats and remote sensing.*

[86] Fratantoni, D.M., P.L. Richardson and C. Wooding, 1999. EOS, Transactions AGU, 80, pg. 43. *Circulation of the North Atlantic Ocean during the 1990's as determined by Lagrangian drifters.*

[87] Lavander, K.L., 2000. Ph.D. Thesis, Scripps Institution of Oceanography, La Jolla, Ca. *Float-based Observations of Convection and General Circulation in the Labrador Sea.*

[88] Cuny, J., R.B. Rhines, P.P. Niiler, and S. Bacon, 2001. Journal of Physical Oceanography. *Labrador Sea boundary currents and the fate of the Irminger Sea Water.*

[89] Buch, E., (1990/2000). Greenland Fisheries Research Institute Report, (reissued in 2000 as Danish Meteorological Institute, Scientific report, 00-12), 405

pp. *A monograph on the Physical Oceanography of the Greenland Waters.*

[90] Overview of Helheim Glacier, glacierresearch.org. *http://www.glacierresearch.com/locations/helheim/overview.html*

[91] Kangerlussuaq Glacier, United Nations Environmental Program, Retrieved 2009-08-16. *https://na.unep.net/atlas/webatlas.php?id=383*

[92] Rignot, E., and P. Kanagaratnam, 2006. Science, 311, 986–990, doi:10.1126/science.1121381. *Changes in the velocity structure of the Greenland Ice Sheet*

[93] Bevan, S.L., A.J. Luckman, and T. Murray , 2012. Cryosphere, 6, 923–937, doi:10.5194/tc-6-923-2012. *Glacier dynamics over the last quarter of a century at Helheim, Kangerdlugssuaq and 14 other major Greenland outlet glaciers*

[94] Seale, A., P. Christoffersen, G. Mugford, and M. O'Leary, 2011. J. Geophys. Res., 116, F03013, doi:10.1029/2010JF001847. *Ocean forcing of the Greenland Ice Sheet: Calving fronts and patterns of retreat identified by automatic satellite monitoring of eastern outlet glaciers*

[95] Inall, M.E., T. Murray, F.R. Cottier, K.Scharrer, T.J. Boyd, K.J. Heywood, and S.L. Bevan (2014). J. Geophys. Res. Oceans, 119, 631–645, doi:10.1002/2013JC009295. *Oceanic heat delivery via Kangerdlugssuaq Fjord to the south-east Greenland ice sheet*

[96] Joughin, I., Smith, B.E., Shean, D.E., and Floricioiu, D, 2014. The Cryosphere, 8, 209-214, https://doi.org/10.5194/tc-8-209-2014. *Brief Communication: Further summer speedup of Jakobshavn Isbræ*

[97] Kendall Haven, 2007. Greenland's Ice Island Alarm. *https://earthobservatory.nasa.gov/Features/Greenland/printall.php*

[98] Joughin, I., Abdalati, W., Fahnestock, M. 2004. Nature. 432 (7017): 608–610. Bibcode:2004Natur.432..608J. PMID 15577906. doi:10.1038/nature03130. *Large fluctuations in speed on Greenland's Jakobshavn Isbrae glacier*

[99] Krishna Ramanujan, NASA, Retrieved 2009-02-02. *Fastest Glacier doubles in Speed. https://www.nasa.gov/vision/earth/lookingatearth/jakobshavn.html*

[100] Pelto, M., Hughes, T., Fastook, J., Brecher, H. 1989. Annals of Glaciology. 12: 781–783. *Equilibrium state of Jakobshavns Isbræ, West Greenland*

[101] *http://cmip-pcmdi.llnl.gov/cmip5/getting_started_CMIP5_experiment.html#T3*

[102] Collins, W.J., Bellouin, N., Doutriaux-Boucher, M., Gedney, N., Halloran, P., Hinton, T., Hughes, J., Jones, C.D., Joshi, M., Liddicoat, S., Martin, G., O'Connor, F., Rae, J., Senior, C., Sitch, S., Totterdell, I., Wiltshire, A., and Woodward, S. 2011. Geosci. Model Dev. Discuss., 4, 997–1062, doi:10.5194/gmdd-4-997-2011, 2011. *Development and evaluation of an Earth-system model HadGEM2*

[103] NOAA global mean CO2 data *ftp://ftp.cmdl.noaa.gov/ccg/co2/trends/co2 annmean gl.txt*

[104] Keeling, R.F., Piper, S.C., Bollenbacher, A.F., and Walker, J.S. 2009. Carbon Dioxide Information Analysis Center, Oak Ridge National Laboratory, US Department of Energy, Oak Ridge, Tenn., USA, doi:10.3334/CDIAC/atg.035, 2009. *Atmospheric CO2 records from sites in the SIO air sampling network. In Trends: A Compendium of Data on Global Change*

[105] N.E. Huang, Z.Shen, S.R. Long, M.C. Wu, H.H. Shih, Q.Zheng, N.C. Yen, C.C. Tung, and H.H. Liu, Proceeding of the Royal Society of London. Series A. 454 (1998),903–995. *The empirical mode decomposition and the Hilbert spectrum for nonlinear and nonstationary time series analysis*

[106] P. Flandrin, G. Rilling, and P. Goncalves, IEEE, Signal Processing Letters 11 (2004), no. 2, 112–114. *Empirical mode decomposition as a filter bank*

[107] Z. Wu and N.E. Huang, Proceedings of the Royal Society of London. Series A 460 (2004), no. 2046, 1597–1611. *A study of the characteristics of white noise using the empirical mode decomposition method*

[108] C.Y. Chang, N.E. Huang, and Z. Shen, Chinese Journal of Physics 35 (1997), no. 6–11, 818–831. *A statistically significance periodicity in the homestake solar neutrino data*

A

Appendix 1

A.1 Model Evaluation

This section of the appendix addresses the questions that follow from the Model Evaluation section of the results chapter (Refer Chapter 4, Section 4.1).

A.1.1 Modelled surface water anomaly

We first address the discrepancy in modelling the surface waters, as inferred from our results for the HADGEM2-ES model, at the Jakobshavn section (Figure 4.5 (c) and Figure 4.6 (b)). To that extent, we evaluate the Sea-Ice Concentration (SIC) field, from 1950-2005, using the Pre-Industrial and Historical simulation for both the models. This is used in conjunction with our inference from the T-S characteristics of the models and observations (Refer section 4.1.2), to understand the presence of a thick, cold and fresh surface water layer in the HADGEM2-ES model.

We infer from our results that the modelled surface component of the East Greenland Current (EGC) is substantially colder (and fresher) than the observations in the HADGEM2-ES model (Figure 4.1 (b) and 4.2). This is seen to be well reciprocated towards the Western Margin as well; owing to the fact that the West Greenland Current (WGC), is in principle, a westward extension of the EGC.

The presence of a relatively cold and fresh surface current component favours the formation and growth of sea-ice in the HADGEM2-ES model (Add figures). We argue, based on comparisons between the annual SIC (Figure A.1 (a)) and T-S climatologies (Figure 4.5(c)), that the thick sea-ice cover, in turn, helps the surface waters to retain their relatively colder profile.

In other words, we base our arguments on the trade-off between the seasonally competing air-ocean interaction processes. To that extent, a higher SIC in summer prevents the surface layer from heating up (SW ↓), which compensates for the heat trapped (LW ↑) during the winter. The energy trapped is spent in melting the sea-ice from below. This becomes apparent while comparing the anomaly in SIC with respect to Pre-Industrial values (Figure A.1 (a)); where both SW↓ and LW↑ would be higher than their Pre-Industrial values in response to anthropogenic forcing, causing a decline in the modelled SIC. This phenomenon, might, in part, play a role towards the modelled freshening of the surface layer in the HADGEM2-ES

model.
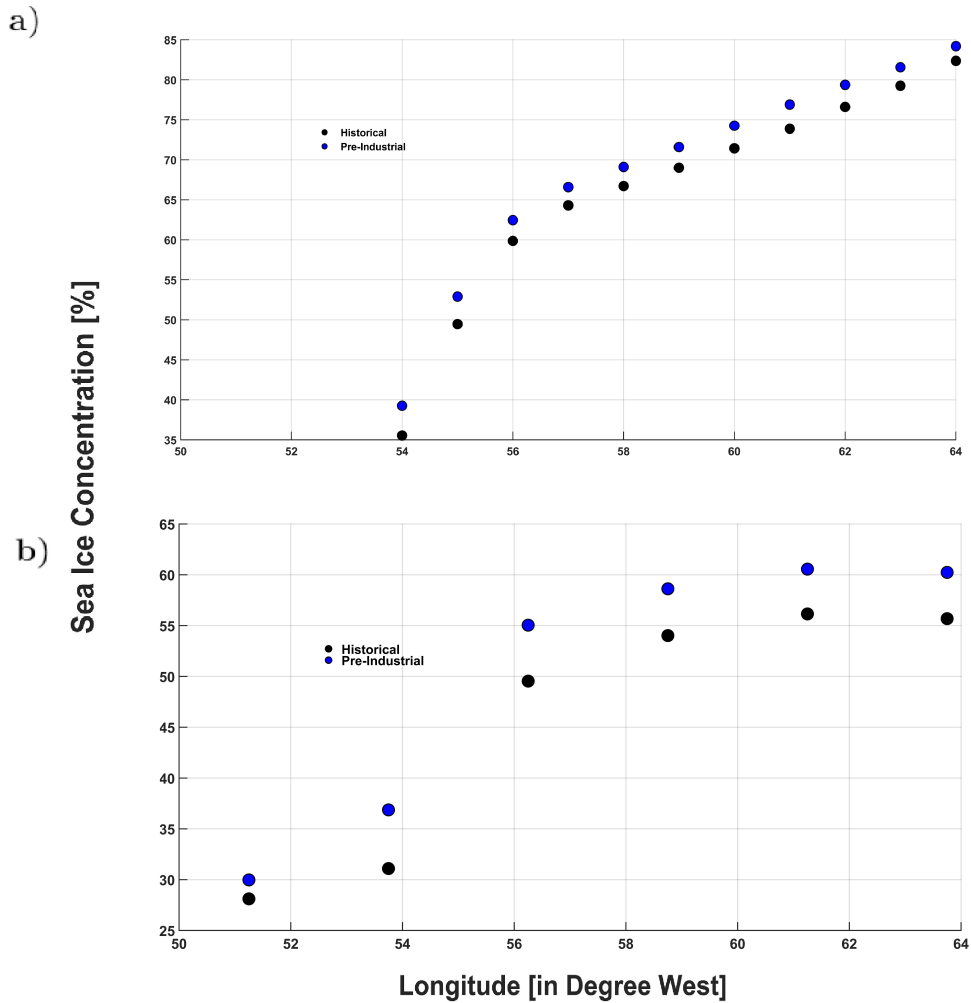
Figure A.1: Jakobshavn Glacier Section: **a)** HADGEM2-ES derived Sea Ice Concentration for the Pre-Industrial and Historical simulation (1950-2005). **b)** GISS-E2-R derived Sea Ice Concentration for the Pre-Industrial and Historical simulation (1950-2005).

Comparing this to the GISS-E2-R model, a warmer and relatively more saline surface layer is seen to limit sea-ice formation (Figure and Figure 4.5 (b)). Furthermore, our results suggest that there is a greater intrusion of the Atlantic Waters (AWs) within the surface water layer (Figure 4.5 (b)), and mixing of these water masses could weaken the stratification, further inhibiting sea-ice growth. The annual SIC climatology is, therefore, relatively lower than the HADGEM2-ES model (Figure A.1 (b)). A lower SIC would further allow the surface layer to take up more heat (SW↓) during summer, compensated in part, by the heat loss from the upwelling longwave radiation(LW↑).

While it is also necessary to address the surface (T-S) anomaly towards the Eastern Margin seen in the HADGEM2-ES model (Figure 4.1 (b) and 4.2), the inter-model discrepancy towards the East is substantially higher. Furthermore, our results suggested that the GISS-E2-R model deviates significantly from the observations. Therefore, drawing such inferences becomes a challenging task.

It is important to point out that our arguments need further validation. Our results suggest that the HADGEM2-ES model overestimates the SIC towards the western margin, and that the GISS-E2-R SIC field is more reliable. This is based on our inferences from the T-S characterisation; where the GISS-E2-R modelled T-S fields are comparable to the observed values. However, validation against observed SIC field is needed to evaluate our hypothesis. We believe that the thick layer of cold and fresh surface waters in conjunction with the relatively higher SIC in the HADGEM2-ES model is responsible for the modelled surface water anomaly [See also: Recommendation 8 and 9 (Chapter: Conclusion, subsection 5.3.2)]

A.1.2 Modelled subsurface (AW) anomaly

For the Kangerlussuaq section, we inferred from our results (Figure 4.3 (a) and 4.3 (b)) that the HADGEM2-ES model slightly overestimates the subsurface temperatures of the AWs. We based our argument on the fact that the temperatures of the Return Atlantic Waters (RAWs) in the HADGEM2-ES model is slightly greater than the observed values.

Furthermore, the subsurface AWs in the GISS-E2-R are comparitively colder than both the observation and the HADGEM2-ES model. This stems from the overcompensating effect of the cold RAWs of the GISS-E2-R model. These water masses are colder than both the observed values and the HADGEM2-ES model.

We validate our hypothesis by comparing the modelled temperature profiles of the Return Atlantic Waters (RAWs) against the observed values. It becomes apparent that the RAWs of the HADGEM2-ES model are warmer than the observed values and the GISS-E2-R model (Figure A.2). The GISS-E2-R modelled RAWs, on the other hand, are the coldest (Figure A.2).

However, drawing such comparisons in the High Arctic is more challenging due to the lack of hydrographic observations. As a result, the observational section only spans from 69-71°N.
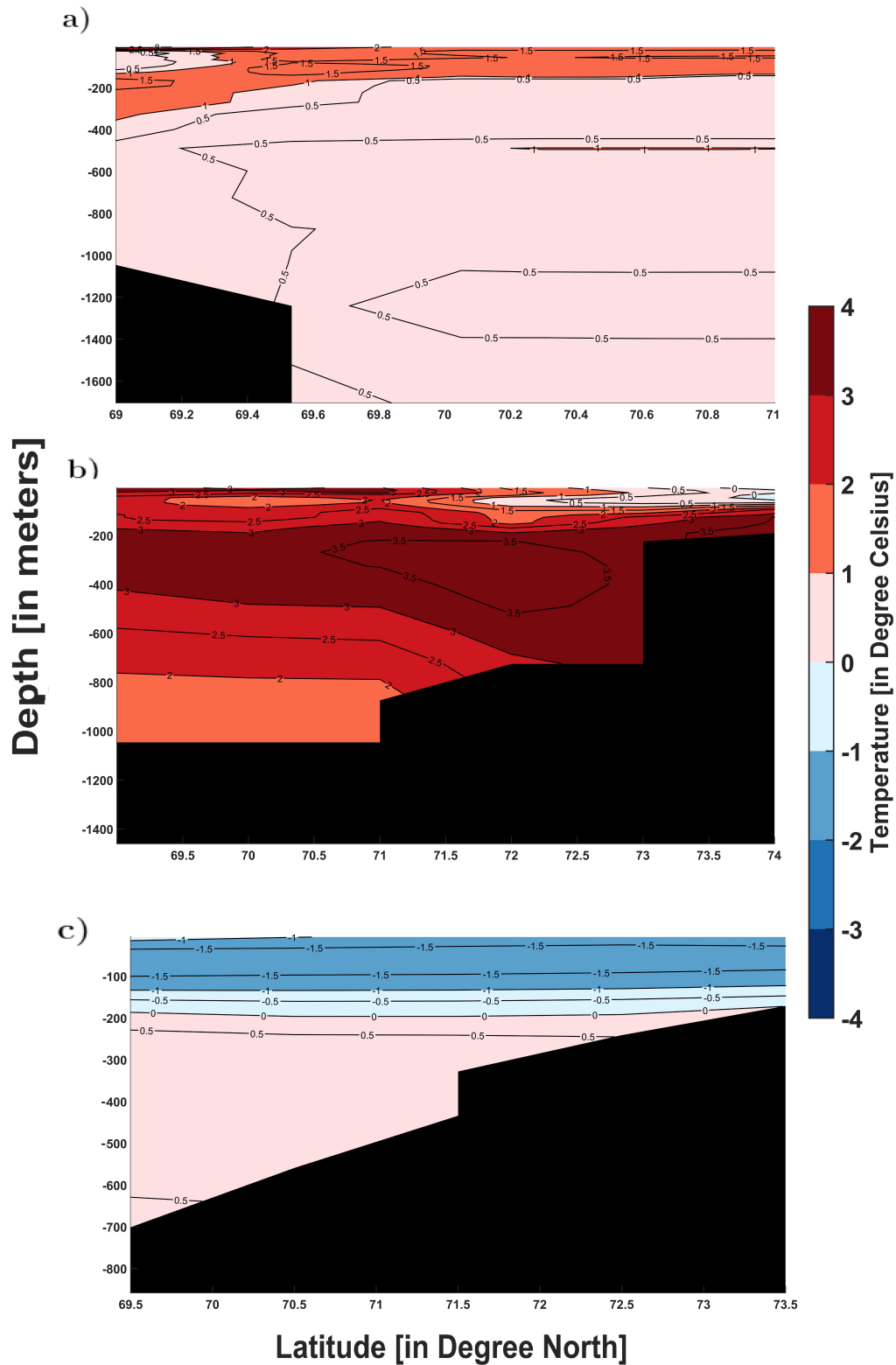
Figure A.2: Potential Temperature profile across the latitudinal section (at a fixed longitude of 19°W), north of Kangerlussuaq Glacier as derived from a) CTD observations, b) HADGEM2-ES model, c) GISS-E2-R model.Owing to a lack of observations in the High Arctic, the CTD section spans only from 69-71°N.

A.2 Changes in variability in the ocean heat forcing

A.2.1 Spatial Variability

This section of the appendix pertains to the questions that follow from the second section of the results chapter, where we analyse the spatial variability in the Ocean Heat Forcing around our study locations. (Refer Chapter 4, Section 4.2).

A.2.1.1 Sea Ice Concentration

A future warming scenario shows considerable freshening of the surface and subsurface waters across our study locations. We argue that the freshening results from a decline in (winter) sea-ice concentration (SIC), which is seen to amplify the (winter) precipitation.

From A.D. 2075-2095, the HADGEM2-ES derived time-series of precipitation at Helheim and Kangerlussuaq section is considerably higher than the global average (Figure A.3 **(a)**). Furthermore, the precipitation is seen to have a strong seasonal cycle. The mean annual precipitation cycle shows that precipitation peaks in autumn/winter (Figure A.3 **(b)**). We argue that this cycle is driven, in part, by the autumn/winter sea-ice retreat (Figure A.3 **(c)**), which could lead to an intensified surface evaporation.

At the Helheim section, this leads to a freshening up to depths of around 150 meters (Figure A.5 **(a)**). Below this depth, the intrusion of AWs from the Irminger Current drives the modelled net subsurface salinity gain (Figure A.3 (b)). At Kangerlussuaq, we see a freshening of the upper 50 meters (Figure A.5 **(b)**), below which, the salinity gain is driven by the highly saline subsurface Return Waters of the Arctic Atlantic.

At the Jakobshavn section, the GISS-E2-R derived time-series of precipitation (A.D. 2075-2095) shows that the precipitation is considerably lower than the global average (Figure A.4 **(a)**). Furthermore, the sea-ice retreat begins towards the end of summer, instead of early autumn, as seen for our locations on the Eastern Margin (Figure A.4 **(c)**). However, the late summer retreat is substantially higher than the autumn/winter retreat seen for Helheim and Kangerlussuaq. We also infer that this retreat relates well with the gain in precipitation seen in the modelled mean-annual precipitation cycle(Figure A.4 **(b)**). Therefore, a considerable (late-summer) sea-ice retreat and a resulting amplified precipitation drives the freshening at Jakobshavn.
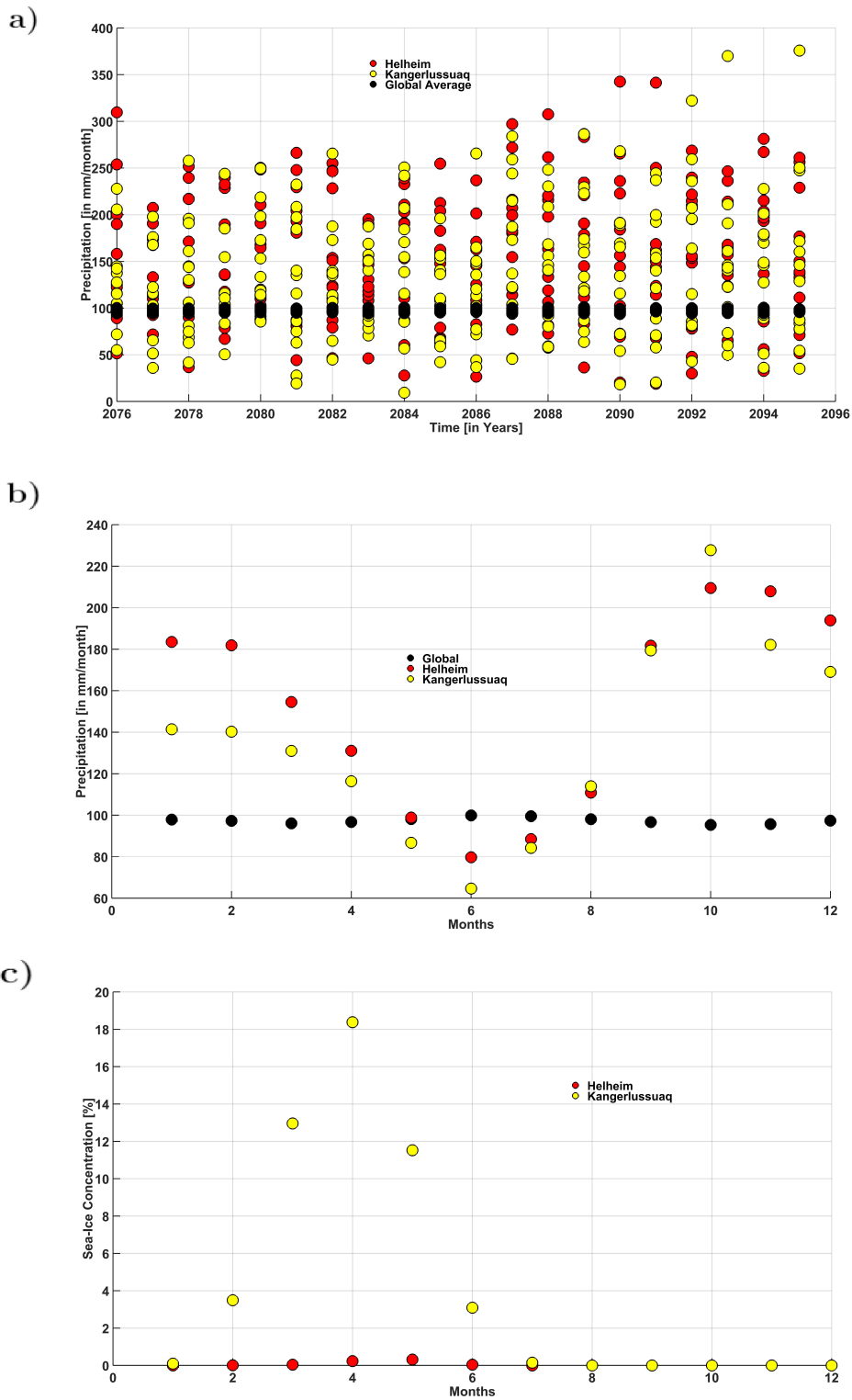
Figure A.3: a) Precipitation (in mm/month) shown for the Helheim (Red) and Kangerlussuaq (Yellow) region for the RCP 8.5 simulation. The global average precipitation is shown in Black. **b)** Mean Annual Precipitation Cycle of figure **(a)** (in mm/month) **c)** Mean Annual Sea-Ice Concentration Cycle for Helheim (Red) and Kangerlussuaq (Yellow) region for the RCP 8.5 simulation.

a)

b)

c)
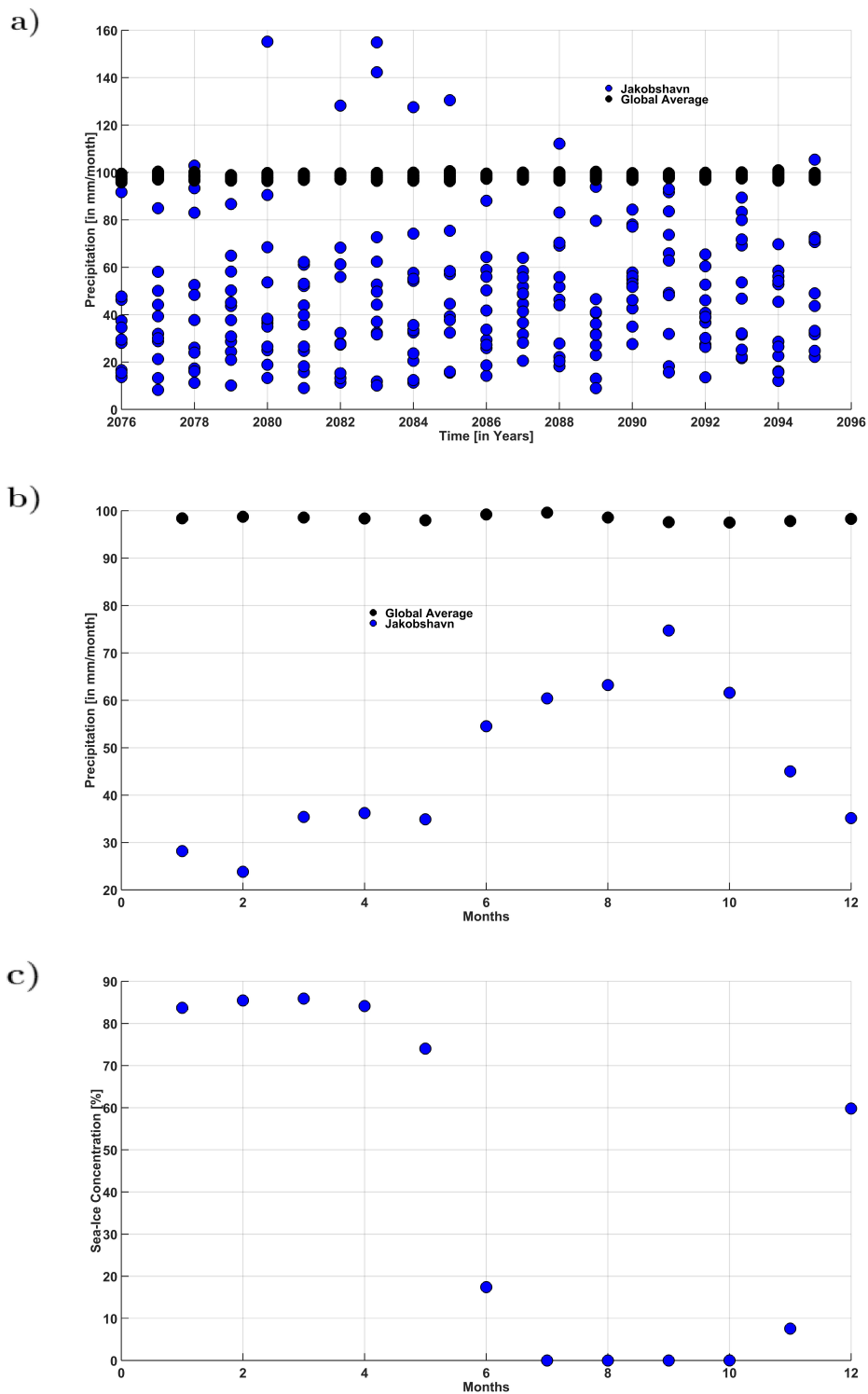
Figure A.4: a) Precipitation (in mm/month) shown for the Jakobshavn (Blue) region for the RCP 8.5 simulation. The global average precipitation is shown in Black. **b)** Mean Annual Precipitation Cycle of figure **(a)**(in mm/month) **c)** Mean Annual Sea-Ice Concentration Cycle for Jakobshavn region for the RCP 8.5 simulation.
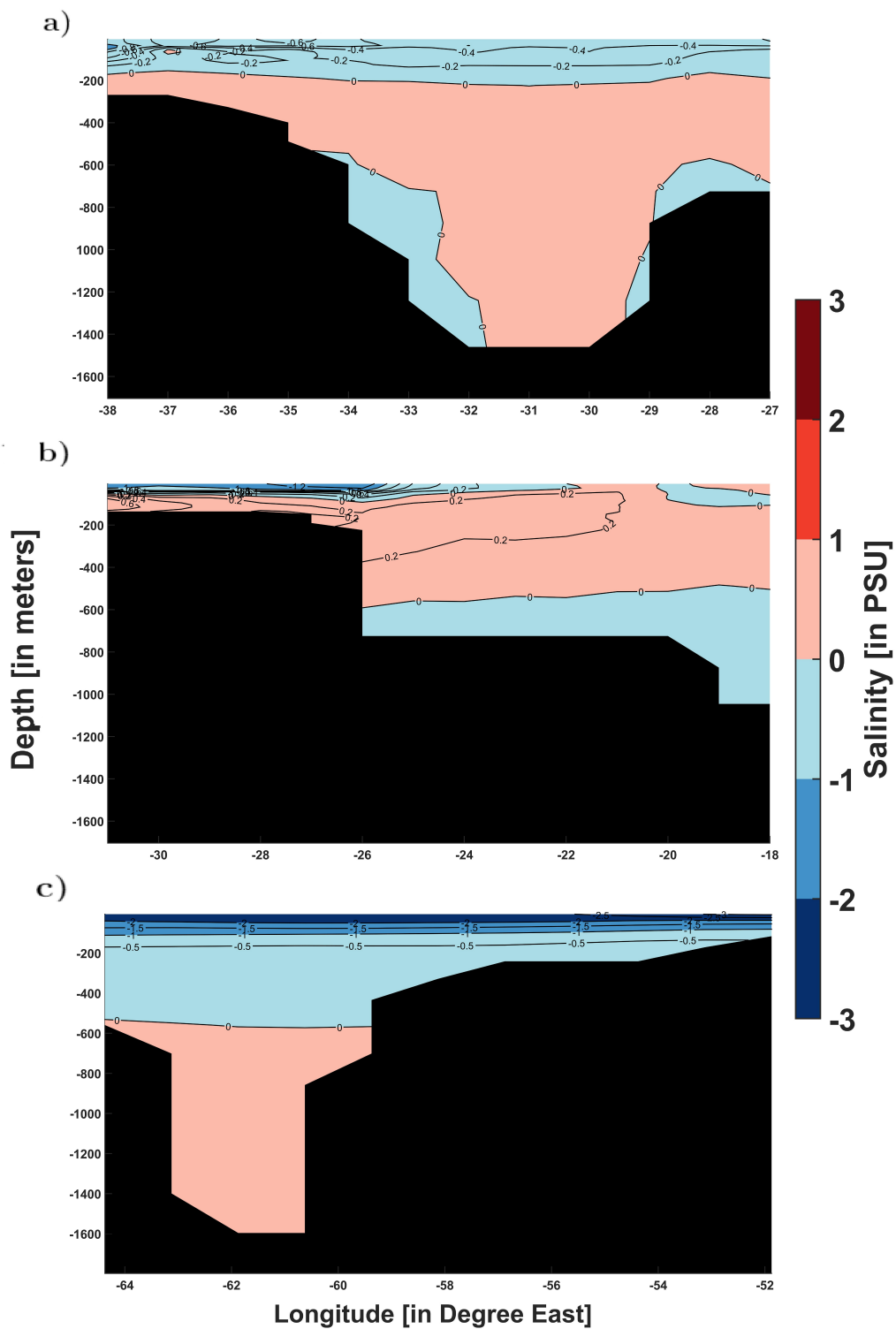
Figure A.5: Salinity anomaly (RCP 8.5 - Pre-Industrial) of **a)** the Helheim Glacier section **b)** the Kangerlussuaq section, and **c)** the Jakobshavn section.

A.2.1.2 Return Atlantic Waters

Our results suggest that the Return Atlantic Waters (RAWs) play a crucial role towards driving the subsurface warming along the Eastern Margin.

The Greenland continental shelf north of the Denmark Strait (DS) is shallower (Figure A.6; 68°N (31°W)) compared to the south (of DS) (Figure A.7, 38°W (65°N)). We argue that only a small fraction of the subsurface RAWs cross the shelf while continuing their southward journey. The major proportion of the southward transport occurs through the Denmark Strait.

These RAWs are much colder (Figure A.7 (b)) compared to water masses found south of DS (Figure A.7 (a)). Upon transcending the strait, they modify the tracer properties of the subsurface AWs of the Irminger Current, before sinking below, forming the Deep Water (DW) masses. In response to the anthropogenic GHG forcings, the RAWs are seen to be more sensitive than the IC (Figure A.8 and Figure 4.7(b)). These RAWs in conjunction with the IC drives the warming of the DWs at the Helheim Glacier (Figure 4.7 (b)).

The IC dominates the subsurface ocean heat forcing at Helheim; as only a small fraction of the RAWs are present on the shelf along the Helheim Glacier (section). However, the RAWs are seen to be more sensitive to GHG forcings.

North of the Denmark Strait, only a small fraction of the IC component is able to cross the shallow sill (Figure A.6: 67-68°N) and reach the Kangerlussuaq Glacier (shelf). The subsurface warming is, therefore, predominantly dependent on the RAWs as opposed to the IC.

In a Pre-Industrial climate, these RAWs are substantially colder (Figure A.7 (b)) than the IC (Figure A.7 (a)), and are seen to overcompensate for the heat advected from the northward component of the IC.

As the RAWs gain in heat in response to the GHG forcings (Figure A.8 (b)), the subsurface warming increases (Figure 4.8 (b)). This gain is effectively more pronounced than the modelled (subsurface) warming of the Helheim Glacier (shelf) (Figure 4.7 (b)).
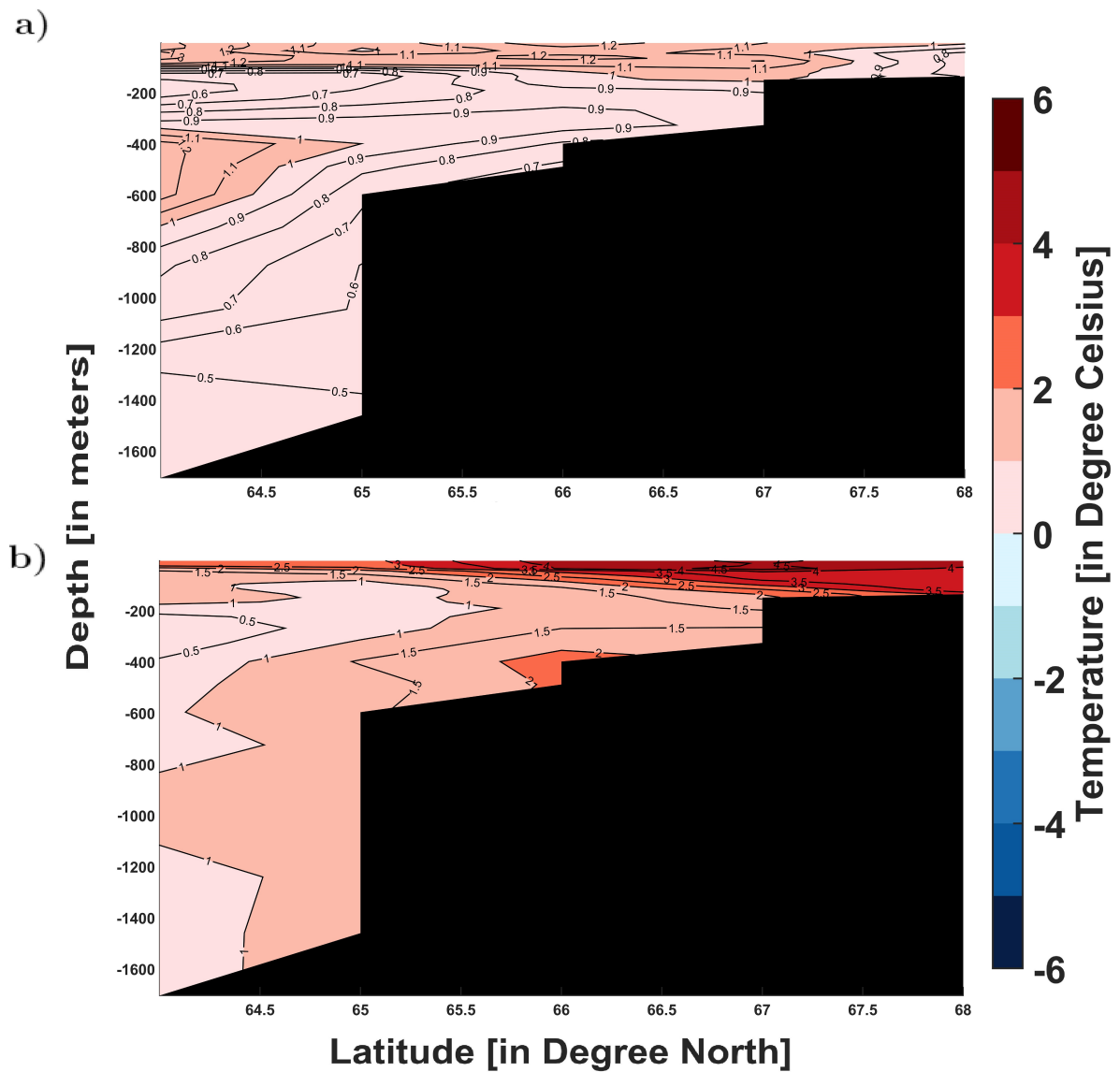
Figure A.6: HADGEM2-ES derived modelled temperature anomaly across the Denmark Strait (31°W) for **a)** Historical-Pre-Industrial and **b)**RCP 8.5-Pre-Industrial simulation.
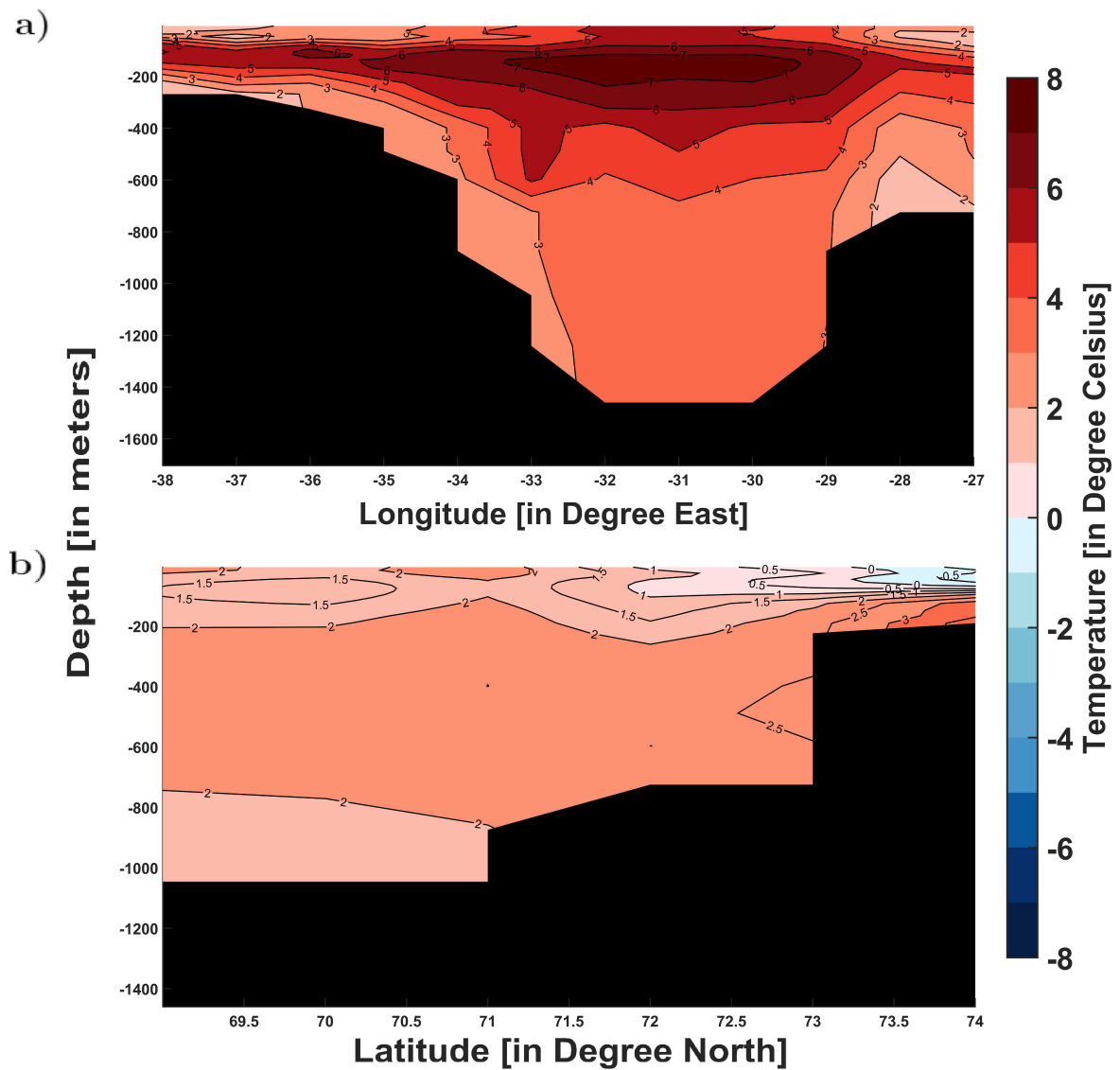
Figure A.7: HADGEM2-ES derived Pre-Industrial modelled temperature profile for **a)** Helheim Glacier section (at a fixed latitude of 65°N) and **b)**Return Atlantic Water (RAW) section (at a fixed longitude of 19°W).
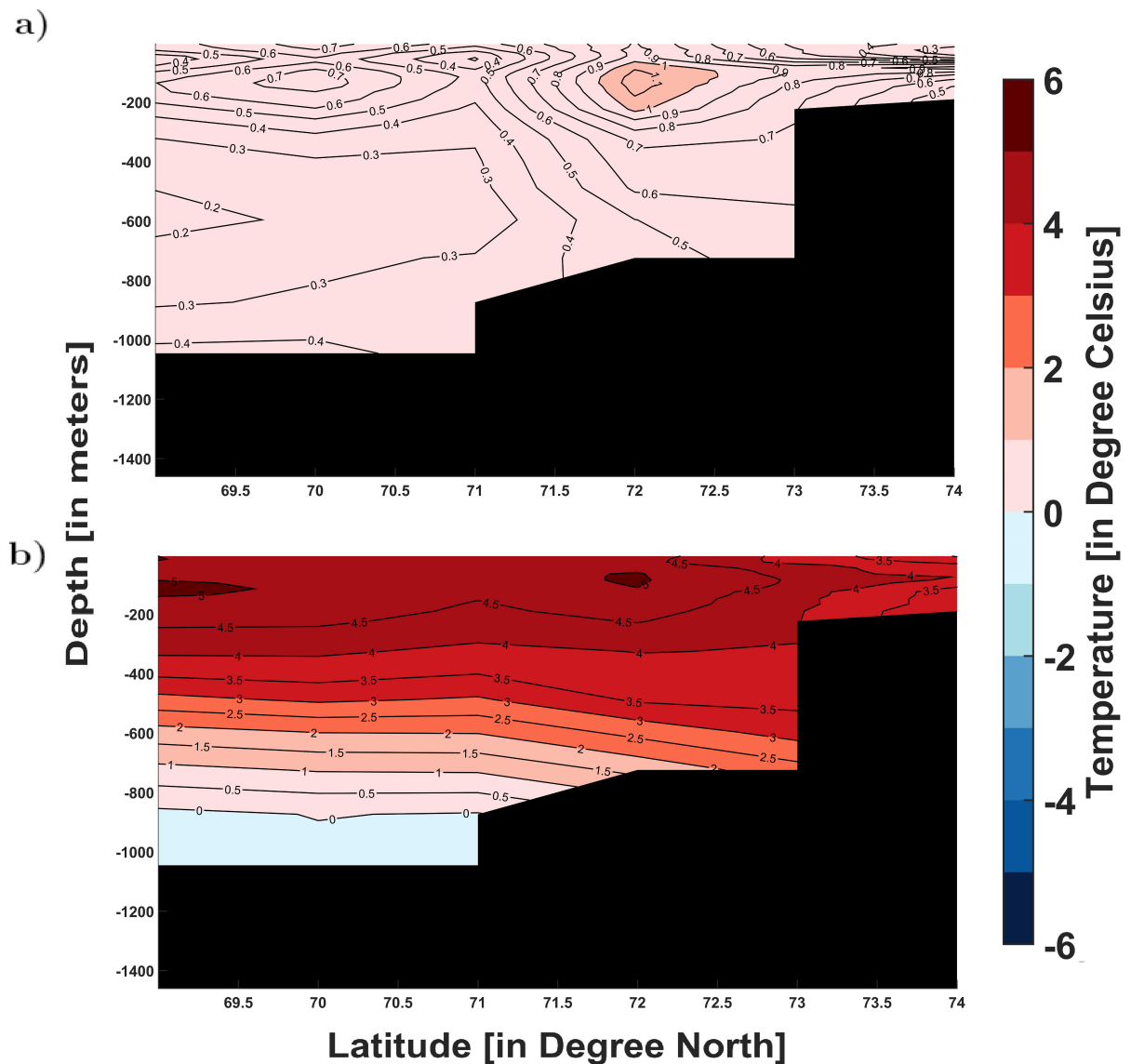
Figure A.8: HADGEM2-ES derived modelled temperature anomaly for the Return Atlantic Water (RAW) section (at a fixed longitude of 19°W) for **a)** Historical-Pre-Industrial and **b)**RCP 8.5-Pre-Industrial simulation.

A.2.2   Temporal Variability

This section of the Appendix contains results from the CEEMDAN analysis of the Historical and RCP 8.5 OHC signals. For each of our study locations, results from the CEEMDAN decomposition is provided. This is followed by a summary table which represents the energy contained in each of the modes and the contribution of each mode towards the total energy in the OHC time series.

Helheim Glacier:

At the Helheim Glacier, the CEEMDAN evaluation decomposes the Historical and RCP signal in 10 Intrinsic Mode Functions (IMFs), labelled as c1-c10 (Figure A.10 and A.11 respectively), in decreasing order of frequency (from high-low). The Pre-Industrial signal is decomposed in 11 IMFs, labelled similarly as c1-c11 (Figure A.9). For each simulation, modes c1-c4 correspond to the high-frequency variability. They contain information regarding the intra-annual cycles in the modelled OHC. Likewise, modes c5-c9 correspond to the low-frequency periodicity and are used to quantify the multi-year cycles. The remaining modes, corresponding to the Historical (c10 Figure A.10) and RCP 8.5 (c10 Figure A.11) simulation, contain information about the long-term, anthropogenic induced trend. We compare this to the remaining modes (c10,c11 Figure A.9) of the Pre-Industrial simulation, which contain the very low-frequency, long-term natural variability.
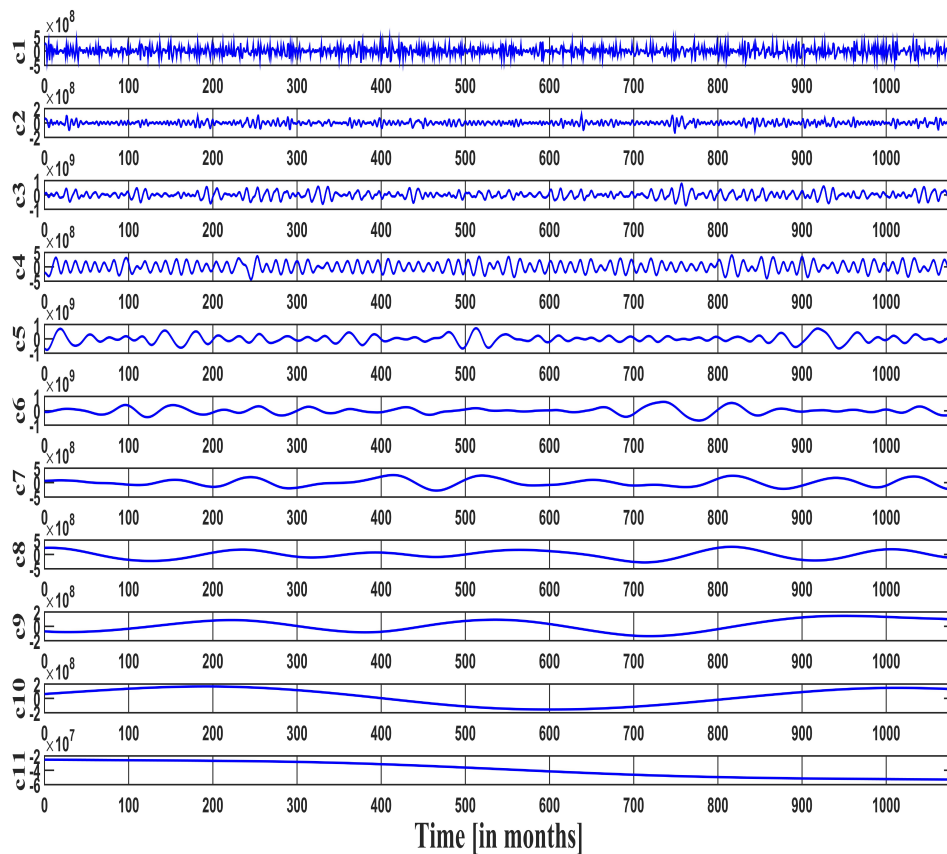
Figure A.9: Modelled Pre-Industrial Signal derived from the HADGEM2-ES model for the Helheim Glacier Section. The 11 different Intrinsic Mode Functions (IMFs) are labelled accordingly from c1-c11. The time period corresponds to the duration of the simulation (1080 months).
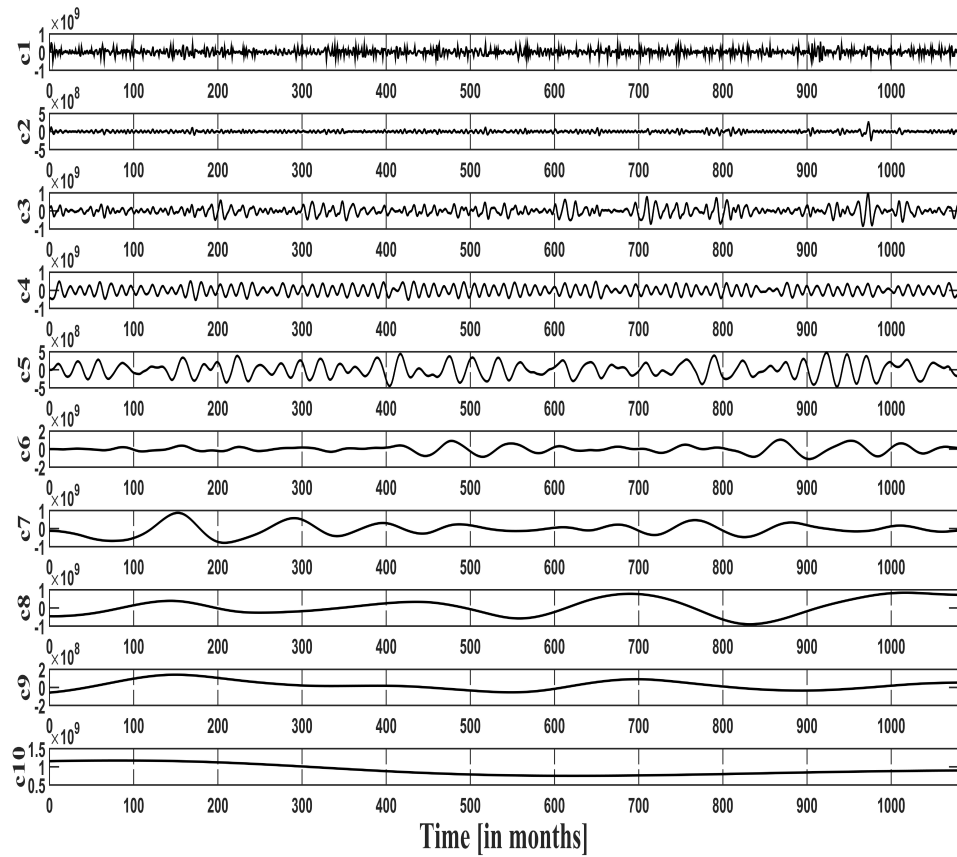
Figure A.10: Modelled Historical Signal from the HADGEM2-ES model for the Helheim Glacier Section. The 10 different Intrinsic Mode Functions (IMFs) are labelled accordingly from c1-c10. The time period corresponds to the duration of the simulation (1080 months).
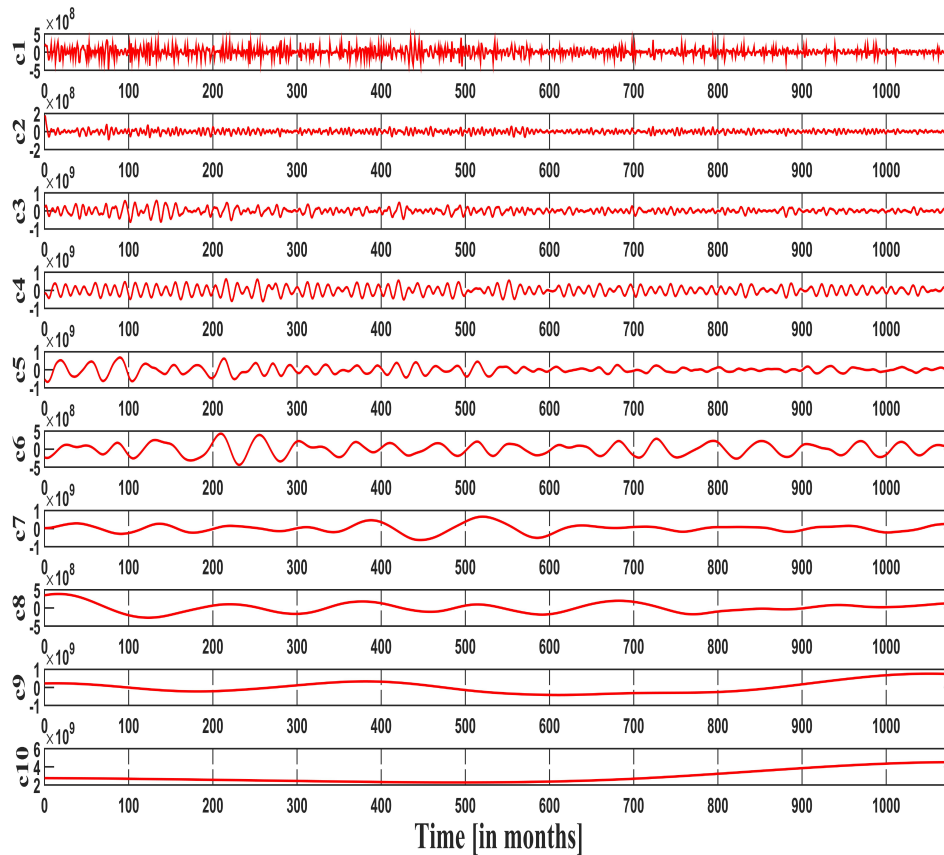
Figure A.11: Modelled RCP 8.5 Signal from the HADGEM2-ES model for the Helheim Glacier Section. The 10 different Intrinsic Mode Functions (IMFs) are labelled accordingly from c1-c10. The time period corresponds to the duration of the simulation (1080 months). The Reconstructed RCP 8.5 Signal was obtained from modes c5-c10.

Kangerlussuaq Glacier:

At the Kangerlussuaq Glacier, the CEEMDAN evaluation decomposes the Pre-Industrial, Historical and RCP 8.5 signal in 10 (labelled as c1-c10; Figure A.12, A.13 and Figure A.14 respectively) Intrinsic Mode Functions (IMFs), in decreasing order of frequency (from high-low). For each simulation, modes c1-c4 correspond to the high-frequency variability. They contain information regarding the intra-annual cycles in the modelled OHC. Likewise, modes c5-c8 correspond to the low-frequency periodicity and are used to quantify the multi-year cycles. The remaining modes, corresponding to the Historical (c9,c10 Figure A.13) and RCP 8.5 (c9,c10 Figure A.14) simulation, contain information about the long-term, anthropogenic induced trend. We compare this to the remaining modes (c9-c10) of the Pre-Industrial simulation (Figure A.12), which contain the very low-frequency, long-term natural variability.
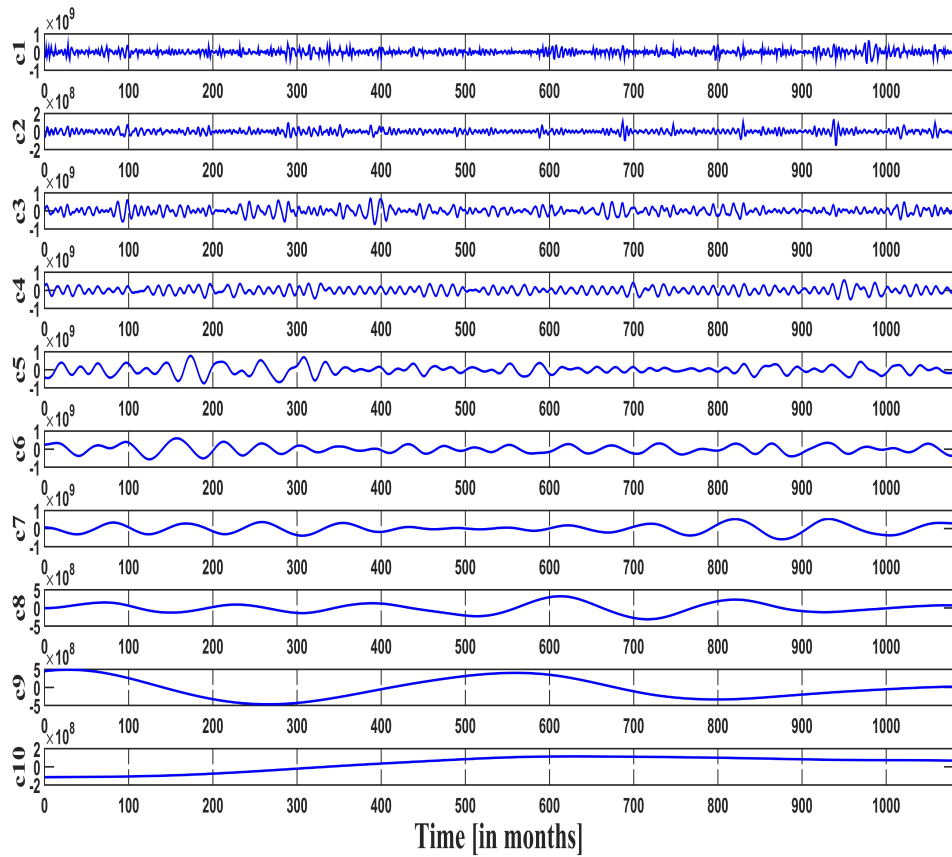
Figure A.12: Modelled Pre-Industrial Signal from the HADGEM2-ES model for the Kangerlussuaq Glacier section. The 10 different Intrinsic Mode Functions (IMFs) are labelled accordingly from c1-c10. The time period corresponds to the duration of the simulation (1080 months).
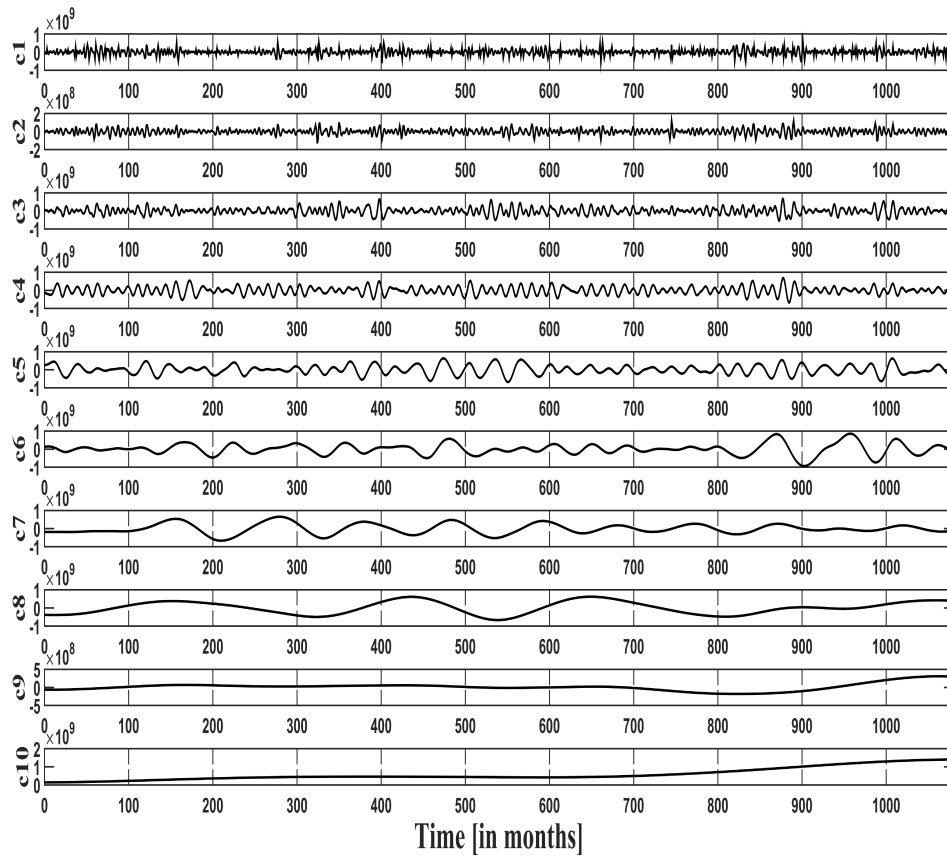
Figure A.13: Reconstructed modelled Historical Signal from the HADGEM2-ES model for the Kangerlussuaq Glacier section. The 10 different Intrinsic Mode Functions (IMFs) are labelled accordingly from c1-c10. The time period corresponds to the duration of the simulation (1080 months). The Reconstructed Historical Signal was obtained from modes c5-c10. The modes c1-c4 correspond to the (high-frequency) background variability in the modelled historical simulation.
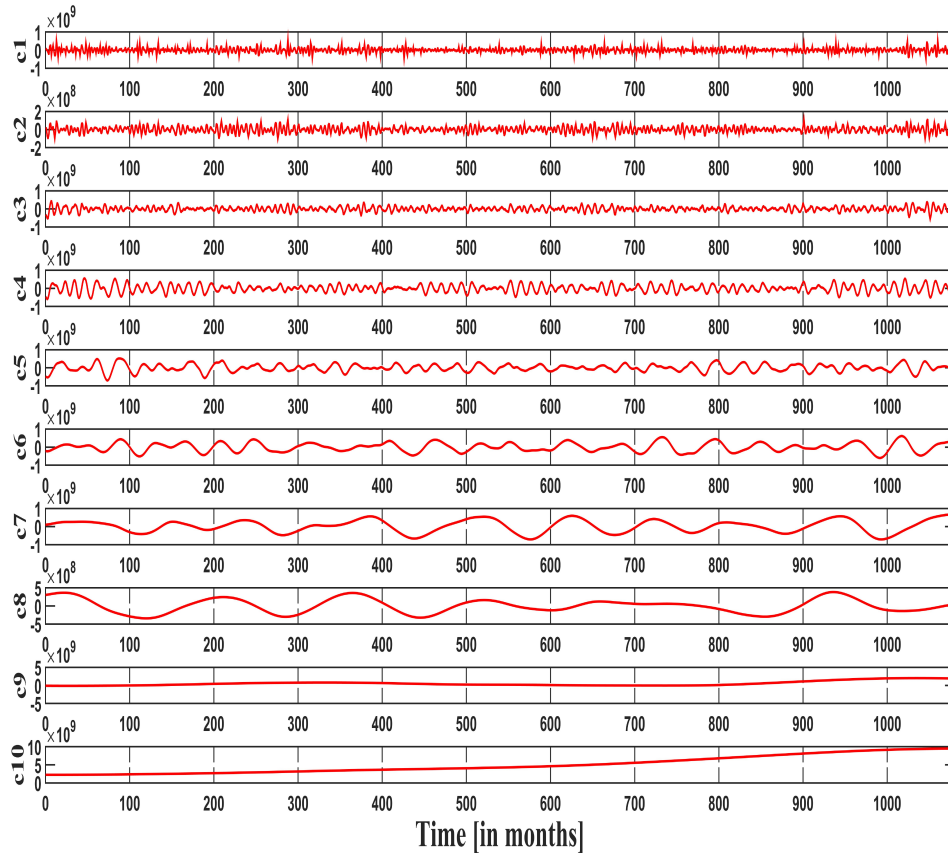
Figure A.14: Reconstructed modelled RCP 8.5 Signal from the HADGEM2-ES model for the Kangerlussuaq Glacier section. The 10 different Intrinsic Mode Functions (IMFs) are labelled accordingly from c1-c10. The time period corresponds to the duration of the simulation (1080 months). The Reconstructed RCP 8.5 Signal was obtained from modes c5-c10. The modes c1-c4 correspond to the (high-frequency) background variability in the modelled RCP 8.5 simulation.

Jakobshavn Glacier:

At Jakobshavn, the OHC signal for the Historical and RCP 8.5 simulation is decomposed in 10 Intrinsic Mode Functions (IMFs), labelled as c1-c10 (Figure A.16 and A.17 respectively), in decreasing order of frequency. The Pre-Industrial signal is decomposed in 11 IMFs, labelled similarly as c1-c11 (Figure A.15). For each simulation, modes c1-c4 correspond to the high-frequency variability. They contain information regarding the intra-annual cycles in the modelled OHC. Likewise, modes c5-c8 correspond to the low-frequency periodicity and are used to quantify the multi-year cycles. The remaining modes, corresponding to the Historical (c10 Figure A.16) and RCP 8.5 (c10 Figure A.17) simulation, contain information about the long-term, anthropogenic induced trend. We compare this to the remaining modes (c10,c11) of the Pre-Industrial simulation (Figure A.15), which contain the very low-frequency, long-term natural variability.
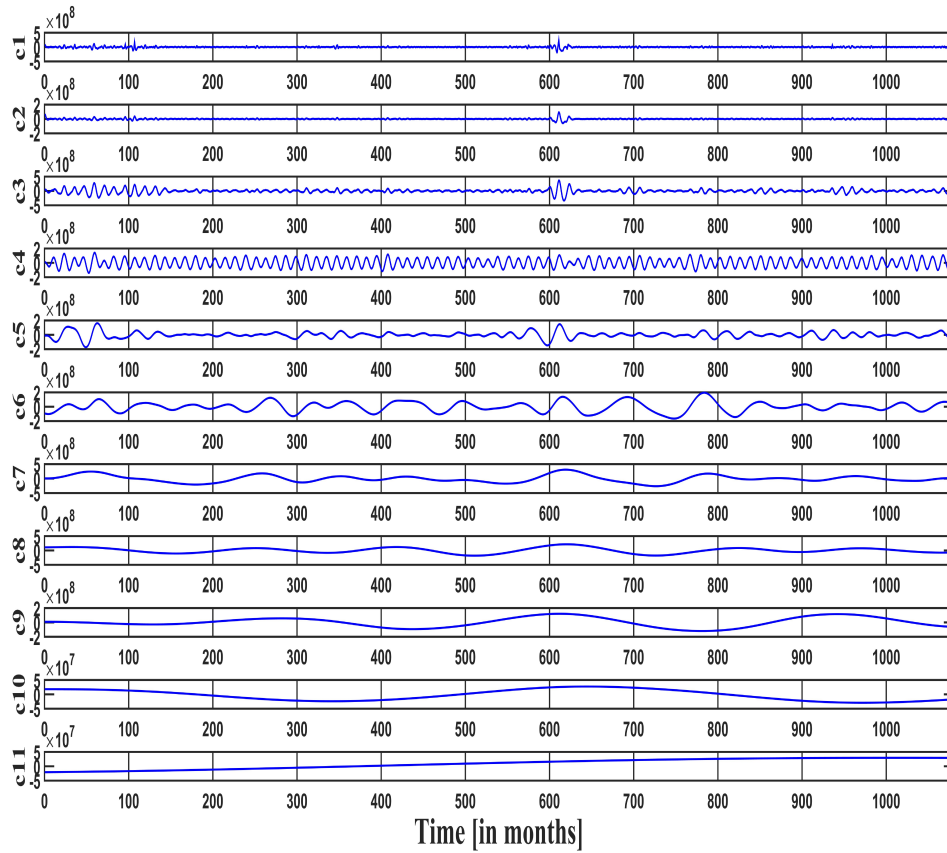
Figure A.15: Reconstructed modelled Pre-Industrial Signal from the GISS-E2-R model for the Jakobshavn Glacier Section. The 11 different Intrinsic Mode Functions (IMFs) are labelled accordingly from c1-c11. The time period corresponds to the duration of the simulation (1080 months). The Reconstructed Pre-Industrial Signal was obtained from modes c5-c11. The modes c1-c4 correspond to the (high-frequency) background variability in the modelled Pre-Industrial simulation.
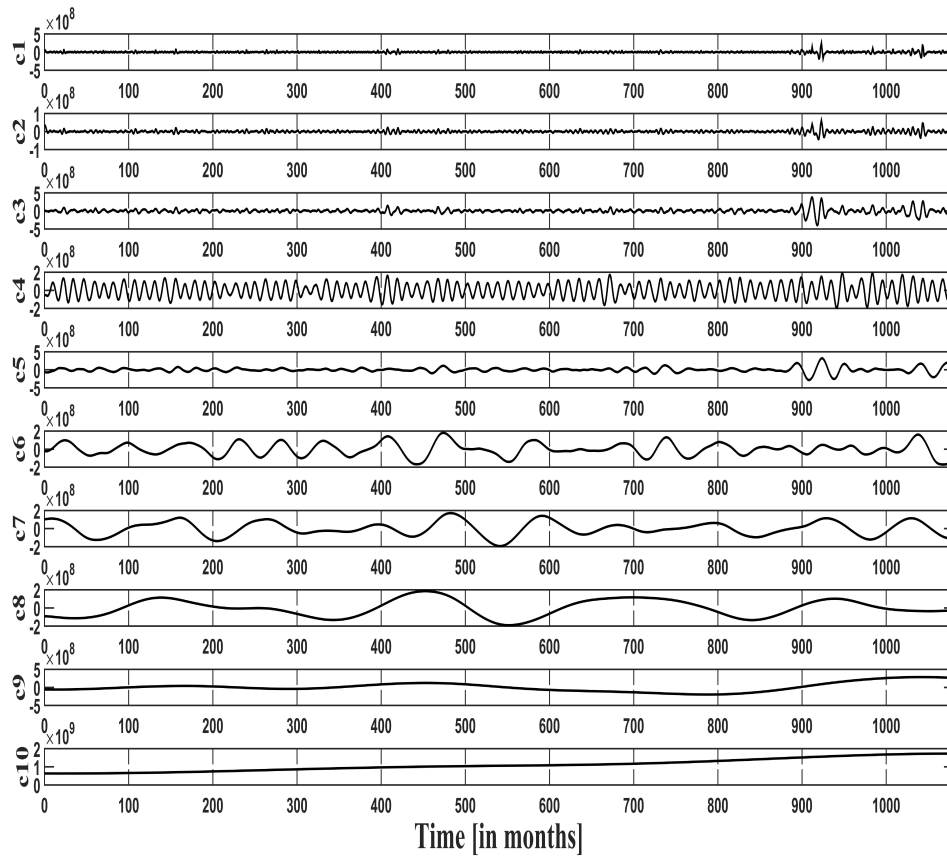
Figure A.16: Modelled Historical Signal from the GISS-E2-R model for the Jakobshavn Glacier Section. The 10 different Intrinsic Mode Functions (IMFs) are labelled accordingly from c1-c10. The time period corresponds to the duration of the simulation (1080 months). The Reconstructed Historical Signal was obtained from modes c5-c10. The modes c1-c4 correspond to the (high-frequency) background variability in the modelled Historical simulation.
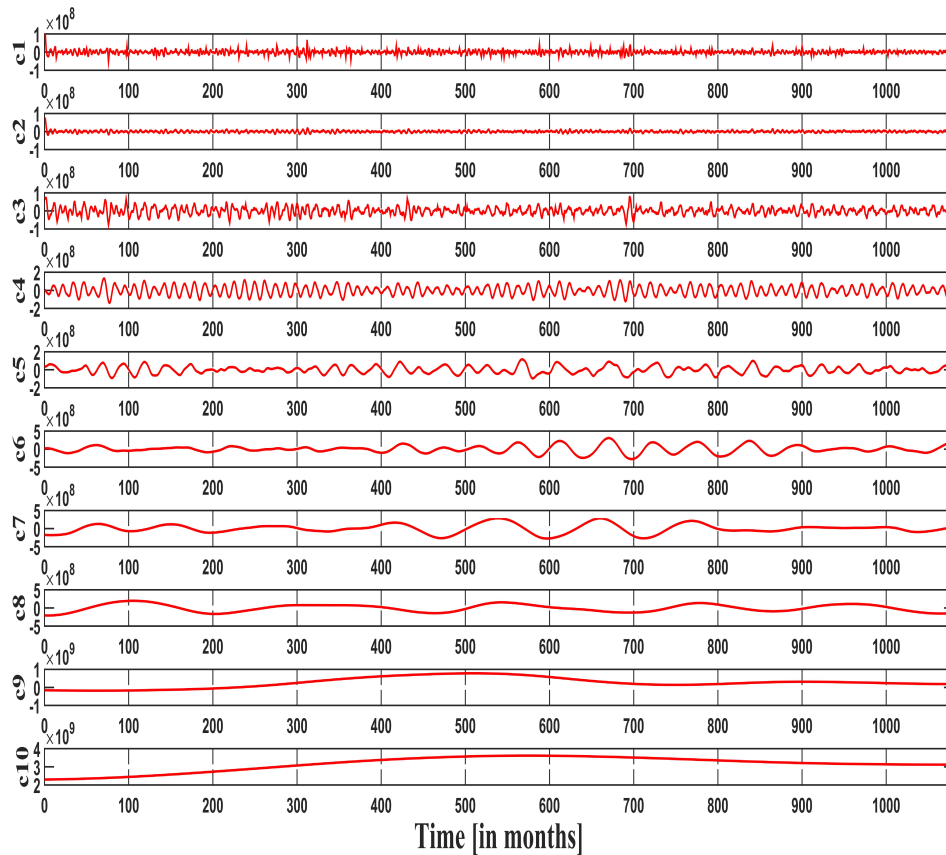
Figure A.17: Modelled RCP 8.5 Signal from the GISS-E2-R model for the Jakobshavn Glacier Section. The 10 different Intrinsic Mode Functions (IMFs) are labelled accordingly from c1-c10. The time period corresponds to the duration of the simulation (1080 months). The Reconstructed RCP 8.5 Signal was obtained from modes c5-c10. The modes c1-c4 correspond to the (high-frequency) background variability in the modelled RCP 8.5 simulation.

Nares Strait: Decreasing trend (and stagnation) in the RCP 8.5 derived OHC

The Nares Strait is a narrow waterway that lies between Northwest Greenland and the Ellesmere Islands. It connects the Northern Baffin Bay to the Lincoln Sea. Monthly modelled sea-ice concentration charts averaged over the strait show that several months in the late half of the 21st century (A.D. 2055-2095) are completely ice free (Figure A.18 (**c**)), allowing for a relatively greater mixing of the Arctic origin waters of the Lincoln Sea with the Baffin Bay waters. The consistent rise in the depth averaged (50-400 meter) temperatures along the Baffin Bay (A.D. 2005-2055) is seen to stagnate around the same time (Figure A.18 (**c**)).
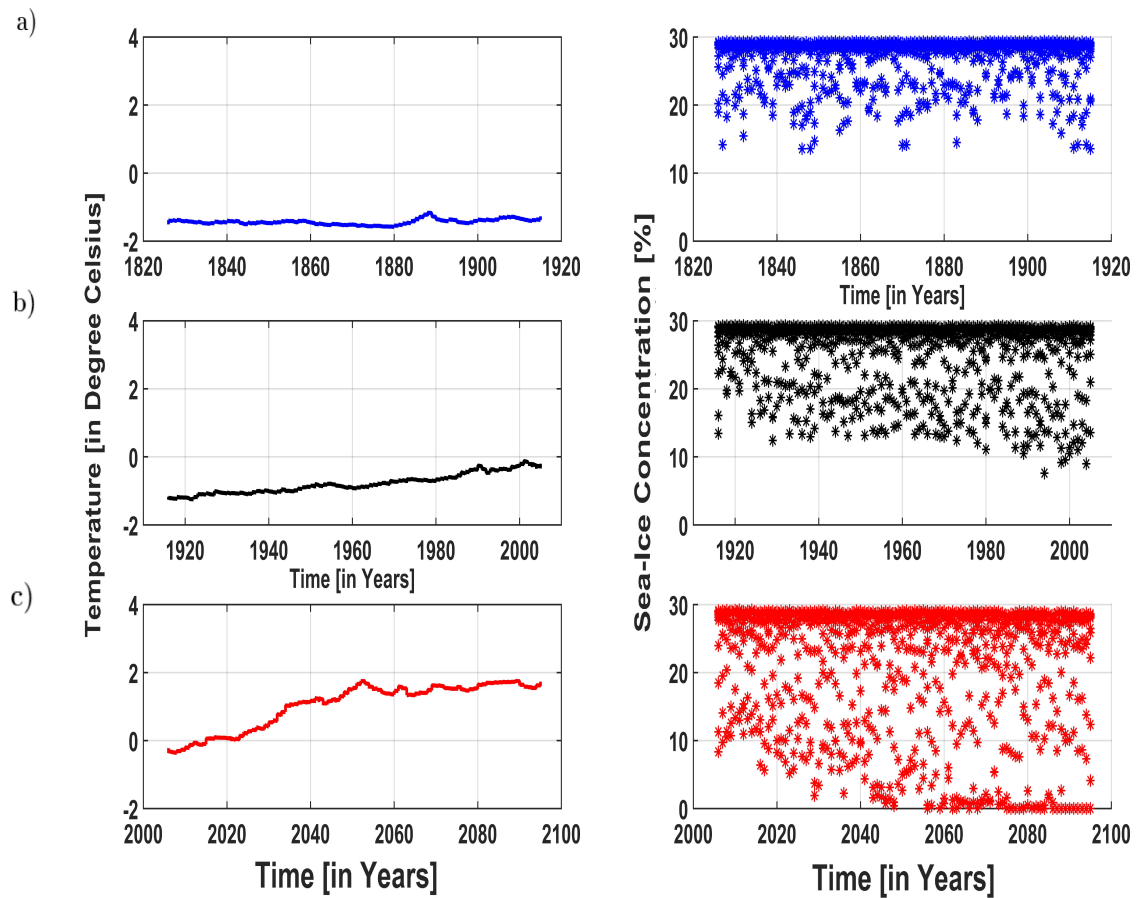
Figure A.18: Time series of Temperature and SIC, derived from the GISS-E2-R model, has been shown for three different scenarios, a) Pre-Industrial (Blue) , b) Historical (Black) and c) RCP 8.5 (Red). The time series of temperature is depth (50-400 meter) averaged over a latitudinal section (69-77°N,60°W), which originates from the southern tip of Nares Strait and stretches to the lower reaches of the Baffin Bay near Jakobshavn. The SIC time series is averaged over the Nares Strait (77-82°N,63-72°W).